



# ScuDo

Scuola di Dottorato ~ Doctoral School  
WHAT YOU ARE, TAKES YOU FAR



Doctoral Dissertation  
Doctoral Program in Mechanical Engineering (34<sup>th</sup> Cycle)

# **Design for Additive Manufacturing**

Innovative topology optimisation algorithms to thrive  
additive manufacturing application

**Riccardo Caivano**

\* \* \* \* \*

## **Supervisors**

Prof. Giorgio Chiandussi

## **Doctoral Examination Committee:**

Prof. Seyed Mohammad Javad Razavi, Norwegian University Of Science And Technology

Prof. Chiara Bertolin, Norwegian University Of Science And Technology

Politecnico di Torino  
November 22, 2021

This thesis is licensed under a Creative Commons License, Attribution - Noncommercial - NoDerivative Works 4.0 International: see . The text may be reproduced for non-commercial purposes, provided that credit is given to the original author.

I hereby declare that, the contents and organisation of this dissertation constitute my own original work and does not compromise in any way the rights of third parties, including those relating to the security of personal data.



.....

Riccardo Caivano  
Turin, November 22, 2021



# Summary

The dissertation concerns the investigation and development of design methodologies carried out to thrive the additive manufacturing application. The purpose of the research is to address several problems and opportunities related to the conceptual design phase of components to be produced by means of additive technologies. The focus has been on the development of the *Top Suite*, a collection of three innovative topology optimisation algorithms named *TopTM*, *TopComp* and *TopFat*.

The first topology optimisation algorithm *TopTM* finds the optimal final topology concurrently optimising the structural stiffness and the heat exchange in a coupled thermo-mechanical system. This algorithm is suitable for the optimisation and lightening of several real components such as heat exchangers, engines, and turbine blades. The problem is density-based formulated and solved using an optimality criterium in limited code lines in the commercially available software Ansys Mechanical.

The second algorithm, named *TopComp*, is suitable for the optimisation of fibre reinforced composites. The final output is the optimal combination of the matrix material distribution together with the optimal embedded fibre orientation. Fully optimised fibre reinforced composites are appropriate for substituting metal components in several applications, leading to outstanding weight reductions. The problem is density-based formulated and solved using an optimality criterion using Ansys Mechanical.

The third topology optimisation algorithm is named *TopFat*. This algorithm provides the final optimal topology considering the presence of defects due to the additive manufacturing process. Consequently, the final topology is guaranteed to be structurally safe considering the process-induced defect presence, both in the quasi-static and fatigue regime. The problem is density-based formulated and solved using a first-order method. The *TopFat* algorithm includes two different stress constraints that represent a critical challenge in the topology optimisation procedure. Therefore, the *TopFat* algorithm is firstly implemented in solved in the Matlab environment as a quite complex code. As a complement of this research, the *TopFat* procedure is extended to the commercially available software *HyperWorks*.

The whole *Top Suite* is thought to be integrated and implemented in commercially available software with a double purpose. Firstly, commercially

available software like *Ansys Mechanical* and *HyperWorks* already have an easy-to-use user interface, tools for the geometrical and finite elements manipulation, and output visualisation which increases enormously the *Top Suite* applications for real and complex components. Secondly, the absence of complex coding and dedicated platforms permits the additive manufacturing community to access the *Top Suite* straightforwardly and take advantage of these design methodologies.

Overall, this dissertation is thought to foster the additive manufacturing application in terms of applicability, effectiveness and reliability.

# Acknowledgment

At the end of my PhD path, I feel compelled to honestly and gratefully acknowledge all the people who supported me and helped me up to this personal life milestone. Without the amazing people and mentors I found along this journey, I am overwhelmed in all humbleness to admit it would not be possible to achieve the ambition of becoming a Doctorate.

My academic Tutor Prof. Giorgio Chiandussi firstly introduced me to the world of design for additive manufacturing. He granted me the possibility to follow in his footsteps and perpetuating the research on this unimaginably vast and thrilling topic.

Doctor Andrea Tridello taught me the manner to be a deserving researcher. He supervised all my work and guided me every single day in the last four years, inspiring me thanks to his extraordinary dedication.

Prof. Davide Paolino has been my most valuable reference. He has been the shoulder I could stand up to accomplish my research and my work. Without his constant support and unassailable solution-oriented mindset, I am sure I would have quit my PhD.

Prof. Filippo Berto believed in my potential at the first sight and assisted me so many times I lost count. He helped me without any reason except that being an exceptional and generous person. His collaboration cannot be defined as anything else than fundamental.

Prof. Chiara Daraio gave me the possibility to visit and collaborate with her research group at the California Institute of Technology, an extraordinary life and work experience.

Doctor Xingjun Gao and Professor Haitao Ma which cooperation gave birth to *TopFat* after more than one year of hard work.

Professor Marco Codegone dispensed his brilliant mathematical knowledge to provide solid analytical proof for my research.

Finally, thanks to my beloved parents and friends.

# Contents

1. Design for Additive Manufacturing.....	4
1.1 Additive Manufacturing: the new era of product design .....	4
1.1.1 Additive Manufacturing technologies.....	8
Selective Laser Sintering/Melting (SLS/SLM).....	9
Electron Beam Melting (EBM).....	10
Fused Deposition Modelling (FDM) .....	11
1.2 Topology Optimisation .....	12
1.2.1 Topology Optimisation evolution and main approaches .....	13
1.2.2 Density-Based / Gradient-based Topology Optimisation .....	18
1.2.3 Numerical Instabilities in Topology Optimisation.....	24
Checkerboards .....	25
Mesh dependency .....	27
Undefined grey zones .....	29
Local Minima.....	31
1.2.4 The <i>Top</i> Suite.....	32
2. <i>TopTM</i> : thermo-mechanical topology optimisation .....	36
2.1 Thermo-mechanical topology optimisation background .....	36
2.2 <i>TopTM</i> solution.....	38
2.2.1 Optimality criterium derivation .....	38
2.2.2 Iterative solution implementation .....	41
2.2.3 Benchmarking validation.....	43
2.3 <i>TopTM</i> results .....	45
2.3.1 Test cases .....	45
2.3.2 Industrial application .....	53
2.4 <i>TopTM</i> final remarks .....	60
3. <i>TopComp</i> : fibre and topology optimisation .....	62
3.1 Composite material topology optimisation.....	62
3.2 <i>TopComp</i> solution.....	64
3.2.1 Optimality criterium for material distribution.....	64

3.2.2	Optimality criterium for fibre orientation .....	66
3.2.3	Coupled topology optimisation.....	68
3.3	<i>TopComp</i> results .....	70
3.3.1	Benchmarking validation .....	70
3.3.2	Sequential and simultaneous approach .....	72
3.3.3	3D component optimisation .....	75
3.4	<i>TopComp</i> final remarks .....	77
4.	<i>TopFat</i> : defect driven topology optimisation .....	78
4.1	Defect population and topology optimisation.....	78
4.2	Fatigue response in presence of defects.....	80
4.3	<i>TopFat</i> solution.....	82
4.3.1	Optimisation analytical definition.....	82
4.3.2	Hybrid stress element model.....	84
4.3.3	Stress constraints implantation.....	86
4.3.4	Solution algorithm.....	90
4.4	<i>TopFat</i> results .....	91
4.4.1	L-shape structure design .....	92
4.4.2	Cantilever structure design.....	96
4.4.3	Corbel structure design .....	99
4.5	<i>TopFat</i> extension to commercial software.....	102
4.5.1	Benchmarking validation .....	103
4.5.2	Variable stress ratio .....	105
4.5.3	Industrial application.....	110
4.6	<i>TopFat</i> final remarks .....	114
5.	Conclusions.....	116
6.	Recommendations for future research .....	117
7.	References.....	118

# List of Tables

Table 1 - Top Suite characteristics .....	33
Table 2 - Properties of the steel for the benchmark validation .....	46
Table 3 - Ti6Al4V properties .....	54
Table 4 - Comparison between optimisation results .....	59
Table 5 - FRC material data .....	72
Table 6 - <i>TopComp</i> data result with different approaches .....	74
Table 7 - Values of <i>TopFat</i> optimisation parameters.....	91
Table 8 - Values of defect and fatigue parameters .....	92
Table 9 - Material, defect population and fatigue modelling parameters .....	106
Table 10 - Applied loads in worst and nominal conditions.....	111
Table 11 - Values of modelling parameters .....	112

# List of Figures

Figure 1 - Hierarchical map of AM processes [2] .....	4
Figure 2 – AM prototype for rocket nozzle featuring internal cooling channels [3] ...	5
Figure 3 - Different designs for the same jet engine bracket by GE challenge [8] .....	6
Figure 4 - Metamaterial optimised structure from Nature [9].....	6
Figure 5 - Size optimisation of truss structure .....	7
Figure 6 - Shape optimisation of holed simply supported beam.....	7
Figure 7 - Topology optimisation of simply supported beam.....	8
Figure 8 - Selective Laser Melting (SLM) process [14] .....	9
Figure 9 - Electron Beam Melting (EBM) process [20] .....	10
Figure 10 - Fused Deposition Modelling (FDM) for composite materials [6].....	11
Figure 11 - Schematic algorithm for a general Topology Optimisation procedure ...	13
Figure 12 - Michell cantilever structure optimisation.....	14
Figure 13 - Topology Optimisation main methods timeline.....	15
Figure 14 - Continuous microstructure and single rectangularly holed unit cell .....	15
Figure 15 - Example of interpolation scheme between density $\rho$ and stiffness $E$ .....	16
Figure - Level Set design domain interpretation by higher order function.....	17
Figure 17 - Design Domain and related quantities .....	19
Figure 18 - Example of simple discrete topology by <i>density-based</i> methods.....	20
Figure 19 - Example of simple continuous topology by <i>density-based</i> methods .....	21
Figure 20 - SIMP and RAMP interpolation scheme for density and stiffness.....	22
Figure 21 - Final topology without penalisation.....	23
Figure 22 - Checkerboard effect on final topology.....	25
Figure 23 – Filtering techniques and element neighbourhood.....	26
Figure 24 - Checkerboard solution by filtering approach .....	27
Figure 25 - Mesh dependency and feature refinement.....	28
Figure 26 - Mesh independency by filtering technique .....	29
Figure 27 - Effect of density projection on classical heat transfer case.....	30
Figure 28 - Topology optimisation with continuation method .....	31
Figure 29 – Thermostructural system .....	39
Figure 30 - Flow chart of thermo-mechanical topology optimisation. ....	41
Figure 31 - Thermal boundary conditions and geometry settings.....	43
Figure 32 - Heat conduction topology optimisation benchmark.....	44
Figure 33 - Structural boundary conditions and geometry settings .....	44
Figure 34 – Structural topology optimisation benchmark.....	44
Figure 35 - Validation of the <i>TopTM</i> on a 2D domain .....	46
Figure 36 - Final optimised topologies obtained with <i>TopTM</i> .....	48

Figure 37 - Thermostructural energy density distribution .....	48
Figure 38 - Meaningful quantities in the final topologies LC1 .....	49
Figure 39 - Meaningful quantities in the final topologies LC2.....	50
Figure 40 - Meaningful quantities after structural topology optimisation of LC1 .....	51
Figure 41 - Meaningful quantities after thermal topology optimisation of LC1 .....	51
Figure 42 - Meaningful quantities in the final topologies LC2.....	52
Figure 43 - Meaningful quantities after thermal topology optimisation of LC2.....	52
Figure 44 - Radiator model and design domain with dimensions.....	53
Figure 45 - Cross section A of the radiator with dimensions.....	54
Figure 46 – Loads and constraints applied to redesigned panel.....	55
Figure 47 - <i>TopTM</i> application on real component.....	56
Figure 48 - Displacement vector sum distribution [mm] .....	57
Figure 49 - Von Mises ideal stress distribution [MPa] .....	57
Figure 50 - Temperature field [°C] .....	57
Figure 51 - Thermal gradient vector sum distribution [°C /mm] .....	58
Figure 52 - Thermostructural energy density distribution [MPa] .....	58
Figure 53 - redesign by <i>TopTM</i> of real LHP radiator .....	60
Figure 54 - Design Domain for a generic material .....	64
Figure 55 - FRC problem coordinate system .....	67
Figure 56 - <i>TopComp</i> flowchart.....	68
Figure 57 - <i>TopComp</i> sequential approach .....	70
Figure 58 - First <i>TopComp</i> 2D benchmark .....	71
Figure 59 - Second <i>TopComp</i> 2D benchmark.....	72
Figure 60 - <i>TopComp</i> simultaneous vs sequential approach.....	73
Figure 61 - Elastic strain energy density [MPa] .....	74
Figure 62 - Three-dimensional design domain with constraints .....	75
Figure 63 - <i>TopComp</i> on a three-dimensional component.....	76
Figure 64 - <i>TopComp</i> layered result with fibre direction.....	76
Figure 65 - Component flow from the initial design domain to the realisation .....	81
Figure 66 - Flowchart of the <i>TopFat</i> solution algorithm .....	91
Figure 67 - L-shape design domain and geometrical dimensions.....	93
Figure 68 - Optimisation results for the L-shape structure .....	94
Figure 69 - Stress distribution of the optimized L-shape.....	95
Figure 70 - Iteration histories for optimisation of the L-shape .....	96
Figure 71 - Cantilever design domain and geometrical dimensions .....	97
Figure 72 - Optimisation results for the cantilever beam.....	97
Figure 73 - Stress distribution of the optimized cantilever beam .....	98
Figure 74 - Iteration histories for optimisation of the cantilever beam.....	99
Figure 75 - Corbel design domain and geometrical dimensions.....	100
Figure 76 - Optimisation results for the corbel structure .....	100
Figure 77 - Stress distribution of the optimized corbel.....	101
Figure 78 - Iteration histories for optimisation of the corbel structure .....	102
Figure 79 - <i>TopFat</i> L-shape benchmark .....	104
Figure 80 - <i>TopFat</i> Cantilever benchmark.....	104
Figure 81 - <i>TopFat</i> Corbel benchmark .....	105
Figure 82 - Corbel design domain for variable stress ratio .....	107
Figure 83 - Defects and related fatigue limits.....	107
Figure 84 – Final topologies under different stress ratios.....	109
Figure 85 - Frist principal stress distribution in the final topology.....	110

Figure 86 - Original component geometry and boundary conditions .....	111
Figure 87 - Design domain and No design domain definition .....	113
Figure 88 - Topologically optimised component.....	114
Figure 89 - Optimised component result data.....	114

# Chapter 1

## Design for Additive Manufacturing

### 1.1 Additive Manufacturing: the new era of product design

Additive Manufacturing, or simply AM, is a set of technologies that appeared for the first time during the 80'. Nowadays, it is very complex to precisely define all the technologies that AM comprehends. Indeed, whatever manufacturing method starts from a digital model and creates a component adding by some means material can be considered belonging to the AM methodology set. Nowadays, the possibilities are so vast that cover almost every type of material, process, and size. AM applies on nanoscale up to macro-scale, on soft materials up to metals and ceramics, on polymers and composites [1].

In Figure 1, a high-level map of most of the current AM techniques is reported. As it can be noticed, the number of processes is quite elevated and still many subcategories are not reported.

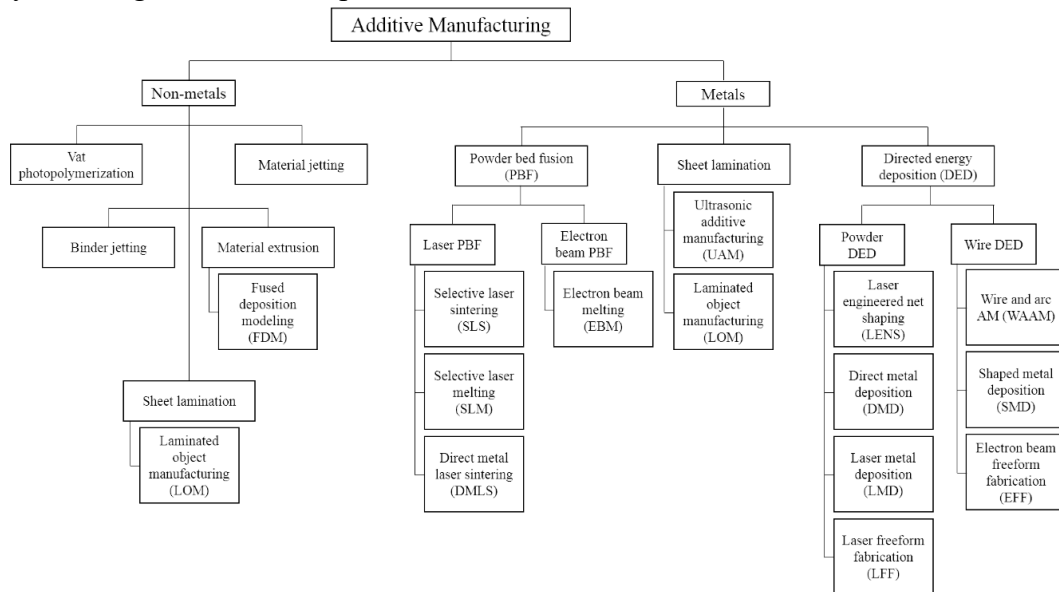


Figure 1- Hierarchical map of AM processes [2]

The very beginning of AM was related to rapid prototyping, mainly on polymeric structures. The processes were limited, expensive, and slow. The huge developments carried out in the last decades by the industrial and scientific community let AM to explode, becoming a state-of-art technology for many sectors, such as aerospace, healthcare, racing, and automotive [3–5].

Indeed, the most innovative aspect of AM is that for the first time in the industrial era, components can be produced by adding and not subtracting material from a raw block. Since no tool has the need of sculpting the part, the shape the component can assume is hypothetically unlimitedly complex. Intricated and convoluted features such as cells or lattice structures and metamaterials are nowadays producible thanks to AM. Components are no more limited to be fully dense solid and geometrically simple parts. These aspects make AM extremely suitable to lighten structures, reduce mass employment, save energy and fuel, increase static and dynamic stiffness, produce multi-component and multi-material parts, and improve many other crucial component responses [6].

Up to the arrival of AM technologies, the producible geometrical features were quite limited due to manufacturing limitations. The related design variables were often evaluated thanks to specific analytical models such as tank wall thickness, beam section width, shaft diameter, or screw length. More complex parts, such as gears, required specific design procedures often dictated by experimental data and experience [7].

AM technologies completely modify this design flow. Indeed, AM unlocks the geometrical and shape freedom that components may assume, opening many questions and possibilities. Figure 2 provides a visual example of the extraordinary possibilities provided by AM technologies. This entire nozzle is built as a unique component with extremely complex metamaterials features in the internal core. Such geometries would be unproducible with any type of subtracting manufacturing methodologies.



**Figure 2** – AM prototype for rocket nozzle featuring internal cooling channels [3]

Overall, one of the greatest opportunities offered by AM processes is the possibility to consider the material distribution, i.e., the component shape as a design variable. Since there are few manufacturing limitations, the designer can tune and modify the component shape to improve its performance. In other words, the material distribution can be exploited as a design variable to make the final

component behave in the desired way. However, this freedom comes together with the main drawback of a remarkable increase in complexity. The definition of the material distribution as a design variable leads to the extremely difficult problem of finding which of the infinite possible combination of material distributions provides the prescribed result. For example, Figure 3 shows various possible geometry solutions for the same jet engine bracket.

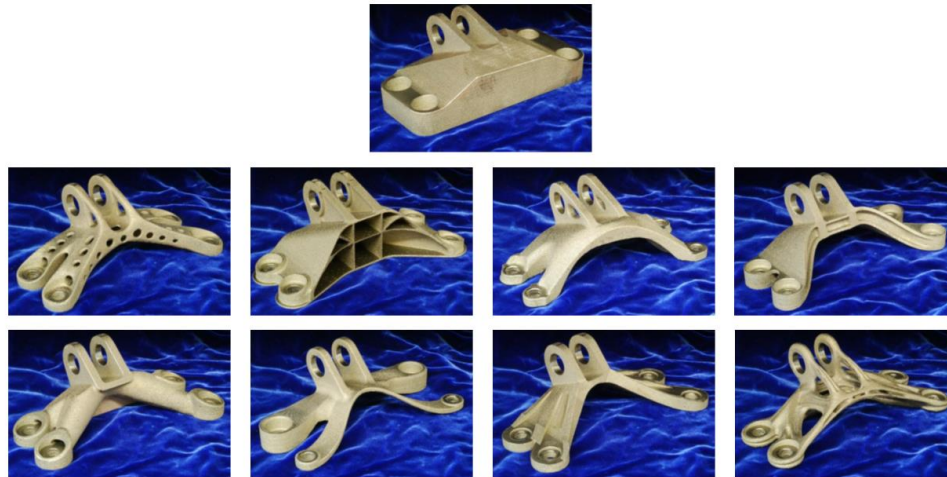


**Figure 3** - Different designs for the same jet engine bracket by GE challenge [8]

As it can be noticed, the proposed solutions are very different from each other, whereas they are all optimised to gain stiffness and reduce mass employment. Even in this simple case, where structural stiffness is the only performance index considered, the material distribution problem is extensively vast and wide.

The closest example of wide design freedom is Nature. Indeed, Nature employs millions of years to optimise structures operating with casual genetic changes until convergence at the equilibrium organism-environment. Figure 4 offers a very intuitive visual example of Nature structural optimisation. With the aim of obtaining extra light and stiff butterfly wings, Nature sculpts these wings with a gyroid core meta structure [9].

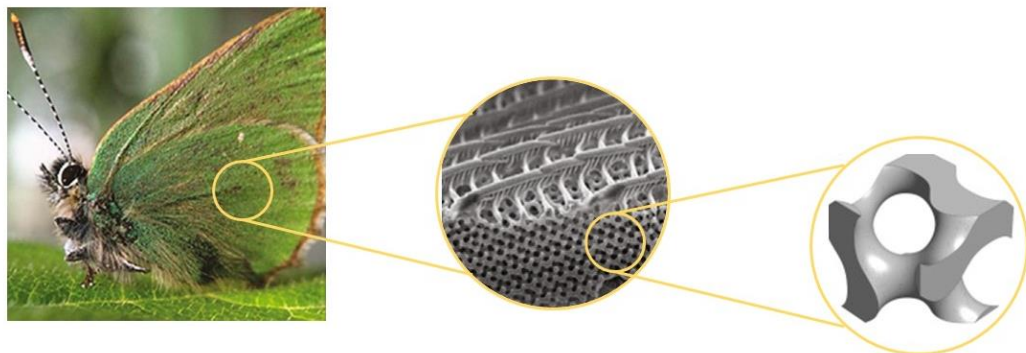


**Figure 4** - Metamaterial optimised structure from Nature [9]

If designers wanted to mimic this procedure, it would be inefficient, to say the least, to use a try-and-error method for every single component. For more, human intuition can be misleading, unprecise, and unreliable. Therefore, the key question AM introduced unlocking the geometry manufacturability is how to exploit this freedom.

The solutions to this question are not trivial and the scientific community is still and hardly working on this topic. Nevertheless, one design methodology is particularly fitting. This design methodology belongs to the set of structural optimisation techniques and it is called Topology Optimisation [10].

In general, structural optimisation is composed by three main procedures. In ascending order of complexity, they are known as size, shape and topology optimisation [11]. Size optimisation focuses on multiple parameters describing a fixed system and finding their optimal combination. For example, the optimal radiuses of a truss structure or the wall thicknesses of a pipe system. Figure 5 shows the classical example of the radius (size) optimisation of the reported bidimensional truss structure.

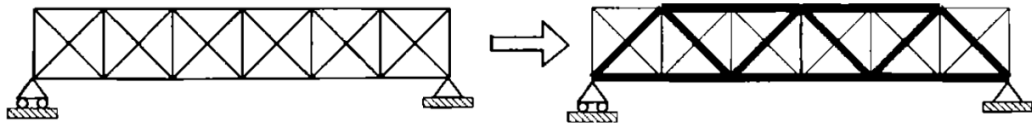


**Figure 5** - Size optimisation of truss structure

Shape optimisation consists of the modification of an existing geometry by moving its surface. In other words, shape optimisation moves punctually the surface of the part, but it does not change the number of holes or the overall structure. Figure 6 shows a holed simply supported beam in the initial configuration on the left, while on the right the optimised domain. As it can be seen, the shape of the hole is changed, optimising a certain final performance. However, the number of holes remains unchanged.

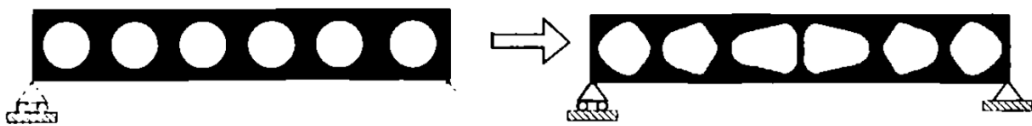


**Figure 6** - Shape optimisation of holed simply supported beam

Lastly, Topology Optimisation is not related to any fixed initial geometry. Basically, starting from a design domain, Topology Optimisation finds the most performant material distribution according to some constraints. Figure 7 shows an example of the result of a topology optimisation process over a simply supported beam where the black zones indicate the material distribution.

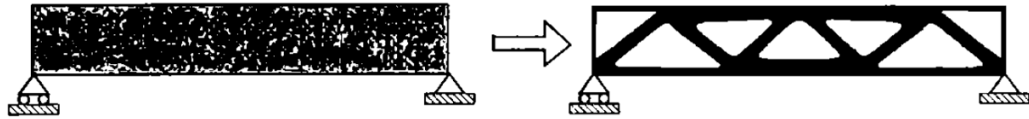


**Figure 7** - Topology optimisation of simply supported beam

Overall, AM opened the doors for a new era of product design where specific and dedicated tools must be developed. Among these tools, Topology Optimisation can fill the gap between design and production capabilities, exploiting the freedom unlocked by AM. However, Topology Optimisation requires accurate development to be applicable and reliable.

The purpose of this dissertation is to introduce, explain and describe three different Topology Optimisation algorithms developed to thrive the AM application.

The first algorithm *TopTM* can optimise the material distribution of a system under thermo-mechanical loads to achieve maximum structural stiffness and heat exchange under a volume/mass constraint.

The second algorithm *TopComp* can optimise concurrently the fibre and the material distribution of composites.

The third and last algorithm *HyperWorks* can include the AM process induce defect influence on the fatigue response of the part within the Topology Optimisation procedure to obtain reliable designs.

These algorithms are closely related to specific AM techniques which make producible the final obtained topologies. Specifically, *TopTM* and *HyperWorks* are related to Powder Bed Laser Fusion (PBLF) technologies on metals, whereas *TopComp* is related to Fused Deposition Modelling (FDM) technology on composites.

With the aim of clarifying the applicability of the developed algorithms through AM, firstly a description of PBLF and FDM is carried out.

Then, a detailed and deepened description of Topology Optimisation is carried out, starting from the origin of this methodology up to the reasons why the developed algorithms present an innovative step in the current state-of-art.

### **1.1.1 Additive Manufacturing technologies**

The presented algorithms, core topic of this dissertation, have been developed to obtain final topologies producible by AM techniques. Therefore, to improve the understating of the added value by the *Top Suite*, the addressed AM techniques are briefly and intuitively introduced. The below descriptions have the only aim of presenting globally the AM technologies. Specific and technical data about AM process is not reported in this dissertation except where necessary.

Below, the main interested AM processes are reported and detailed. Two of them belongs to the set of Powder Bed Laser Fusion (PBLF) technologies to manufacture metals [12]. They are Selective Laser Sintering/Melting (SLS/SLM) and Electron Beam Melting (EBM) respectively. As for composite materials the

key AM process is the Fused Deposition Modelling (FDM) with double extrusion [13].

## Selective Laser Sintering/Melting (SLS/SLM)

Selective Laser Sintering/Melting (SLS/SLM) is an AM process where the component is obtained by fusing selectively its sections layer by layer with a laser starting from a bed of raw metal powder. The distinction between the two nomenclatures is not always clear, many times they are interchangeable since they describe the same process. However, from a more rigorous point of view, nomenclature Sintering is referred exclusively to ceramic and polymeric thermoset materials, whereas Melting is referred to metal and polymeric thermoplastic materials.

The schematic representation of this process is reported in Figure 8. A highly energetic laser is deflected and focused by a series of lenses and mirrors to impact a layer of raw powders. This powder layer is uniformly spread by a roll which is feed by a tank, usually set aside the building zone. The laser impacting the powder selective fuses the powder together and, following a predetermined path, creates the bulk section.

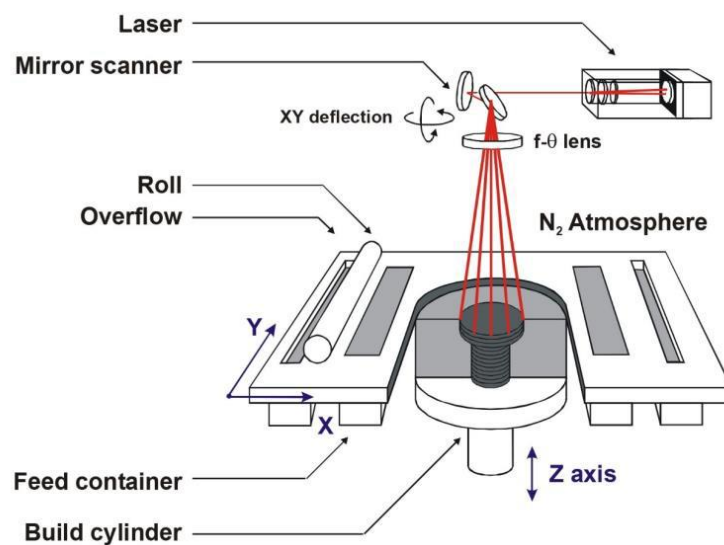


**Figure 8** - Selective Laser Melting (SLM) process [14]

After the section melting and consequent solidification, the building area is moved downward for a distance equal to the powder layer thickness. At this point, the roll spread another powder layer above the previous one, and the process is repeated. In the end, the final component is created layer by layer and surrounded by unmelt raw powder.

To avoid oxidation during the solidification phase, the internal chamber is put under a controlled inert atmosphere, usually N<sub>2</sub>. Often, the powder bed is heat up to 200°C to reduce the thermal gradient in the process.

Of course, this is just a very brief explanation of the process. In reality, the SLM is extremely complex, and hundreds of parameters come into account to

define the final component properties. For example, classical process parameters are the scan speed, the laser power, the hatching distance, the scanning strategy, the laser spot, the layer thickness, the mean powder size, and many others.

The freedom in obtainable geometrical shapes is great and incomparable with the traditional subtractive method. However, some drawbacks and limitations are present. Some major limitations of SLM are an overhanging failure, limited building dimensions, induced anisotropy, powder removal, lack of repeatability, the remarkable presence of process-induced defects [15–17].

## Electron Beam Melting (EBM)

Compared to SLM, Electron Beam Melting (EBM) is a very similar process, anyway, some notable differences are present. The schematic process is represented in Figure 9. First, the laser as a heat source to fuse the powder is substituted by a beam of electrons. This beam is deflected using electromagnetic lenses to correctly impact the powder bed. The other difference is the absence of atmosphere in the building chamber. Otherwise, electrons would impact the air molecules without reaching the powders. Lastly, the building chamber is heated up to 800°C, almost four times higher temperature than the SLM process. Indeed, EBM is often known as a hot process whereas SLM is a cold process due to this temperature difference. EBM has the same potentialities and drawbacks as the SLM process. The main differences are in the final roughness, higher in the EBM process due to higher spot of the electron beam compared to the laser, and thermal exposure due to different chamber temperatures [17–19].

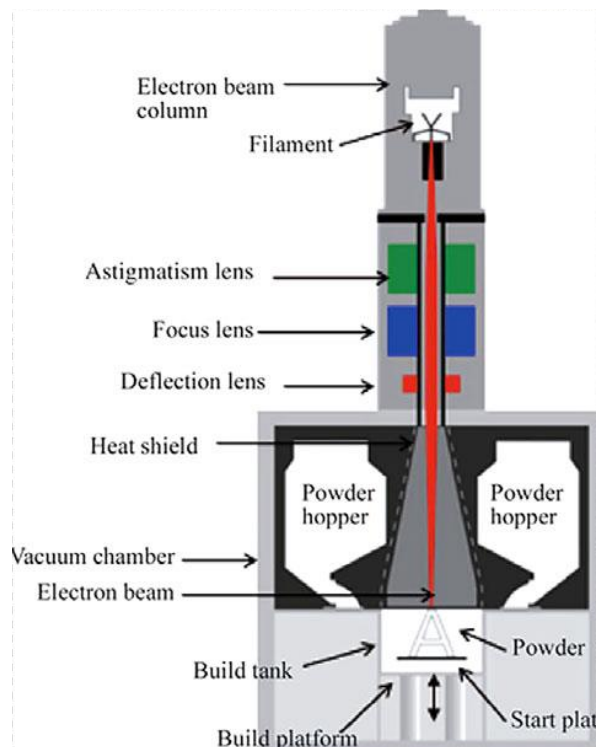


**Figure 9** - Electron Beam Melting (EBM) process [20]

## Fused Deposition Modelling (FDM)

This technology is suitable for thermoplastic polymeric material only and it is one of the most diffused. Classically, in the Fused Deposition Modelling (FDM) a roll forces the raw filament into a hot nozzle. When the filament passes through the nozzle, the material melts and can be deposited on the building platform following the path run by the extrusion head. Once out of the hot nozzle and in touch with the building platform, the raw fused material solidifies keeping the imposed shape. The subsequent layer is created moving the platform downward or the extrusion upward. During the extrusion, the thermoplastic polymer can be charged with a continuous fibre filament, usually stiffer but more brittle. The schematic process is reported in Figure 10.

Obviously, this process has much more constraints compared with SLM and EBM. Indeed, the producible geometries are much more limited. Furthermore, the fibre can be distributed only parallel to the building plate, generating strongly anisotropic properties.

However, this composite methodology production is the first step towards a novel generation of composite components. Nowadays, the production of composite materials is for a large part manual, complex and expensive [6,13,21].

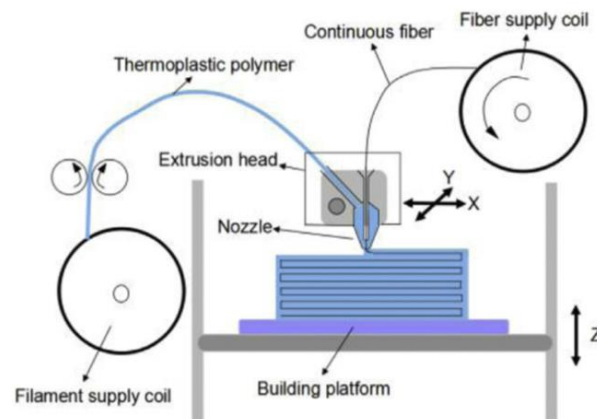


**Figure 10** - Fused Deposition Modelling (FDM) for composite materials [6]

## 1.2 Topology Optimisation

The introduction of AM allows the production of a vast range of shapes and geometries, previously inaccessible. This manufacturing freedom comes together with the issue of being able to exploit this freedom. Therefore, an entire part of classical design methodologies evolved to suit the possibilities introduced by AM. Among these design methodologies, one emerged as most promising to fully take advantage of AM, i.e., Topology Optimisation.

Topology Optimisation is essentially a minimisation problem where the objective is a certain performance of the analysed system and the variable is the material distribution of the system itself. The minimisation problem can be set with one or more constraints such as a final maximum volume. In other words, Topology Optimisation answers the crucial question of where placing the material to obtain maximum performance. This idea is often associated with many other names, such as *bionic design*, *morphogenesis*, *generative design*, or *nature inspired design*. However, these nomenclatures belong to the Topology Optimisation approach and solve the same problem [11].

Topology Optimisation can be applied to several physical problems, in other words, the performance of the system to be optimised can be electrical, thermal, mechanical magnetic, optical or a combination of them. In any case, Topology Optimisation is mainly composed of three phases, reported below [22–24].

- 1 **System definition:** in this phase, the initial design domain, the boundary conditions, and the material properties are defined. This phase is related to the specific problem and component addressed. The output, usually obtained with a simulation by means of Finite Element Analysis (FEA), is the system data and behaviour.
- 2 **Topology Optimisation setup:** in this phase, the Topology Optimisation is effectively defined, indeed the objective, the variables, additional functions, and so on are evaluated from the system data. Furthermore, the derivatives and the gradient of the objective and the functions are calculated with respect to the design variables, i.e., the material distribution, or other relevant quantities.
- 3 **Minimisation problem solution:** in this phase, the optimisation is solved. As mentioned before, Topology Optimisation consists of a minimisation problem, therefore, once the Topology Optimisation problem is set up the minimisation can be carried out by several means. The simplest way is using optimality criteria (OC), otherwise much more complex tools can be employed. Classically, the Method of Moving Asymptotes (MMA) [25] is used for this type of problem. Anyway, many other solvers can be used, based on gradients evaluation or even on machine learning, neural network methods [26].

Overall, Topology Optimisation can be applied and solved in many ways, depending on the system and the specific application. In Figure 11 a schematic algorithm for a general Topology Optimisation procedure is reported. In addition, the three main phases are reported and individuated.

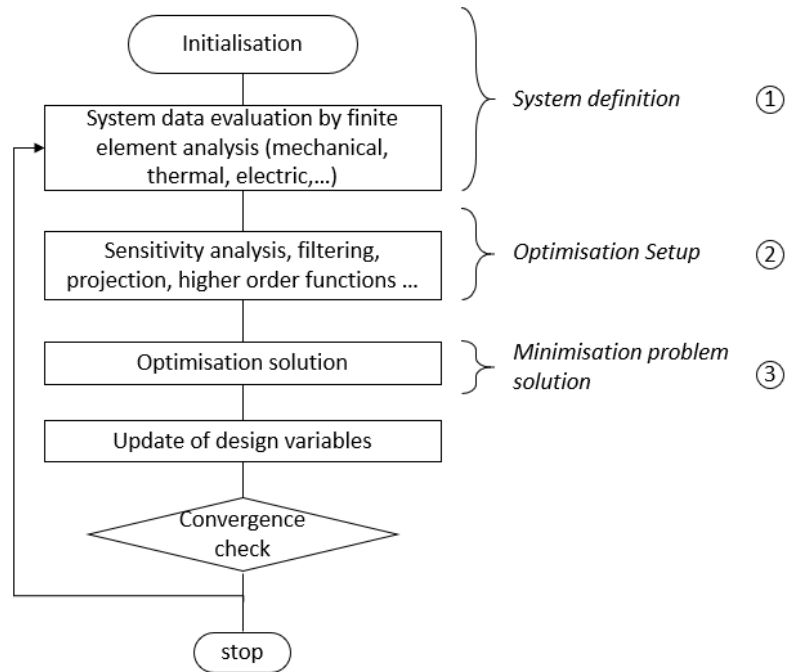


**Figure 11** - Schematic algorithm for a general Topology Optimisation procedure

In the following paragraph, a brief description of the evolution and some historic hints related to Topology Optimisation are described. This is useful to understand the role of the presented algorithms in the Topology Optimisation panorama. In addition, the main Topology Optimisation approaches and solvers are presented. All the presented *Top* algorithms belong to the *gradient-based / density-based* approach which characteristics will be deeply detailed in this dissertation. On the contrary, the main other approaches are here reported for completeness and briefly described to understand the key differences compared to the *Top Suite*.

### 1.2.1 Topology Optimisation evolution and main approaches

Topology Optimisation as a concept has been introduced for the very first time as an analytical procedure by Michell in 1904 in the mechanic field [27]. The research focused on finding the most performant, or stiffest and lightest structure to support a load in a bidimensional system. The most classical example reported in the original paper is shown in Figure 12. In Figure 12, B is the locking point, A is located horizontally with respect to B, the load F is applied perpendicularly to line AB. The dashed lines represent some first principal stress paths, whereas the bold lines represent the optimal structure to support load F, tracing the dashed ones. Figure 13

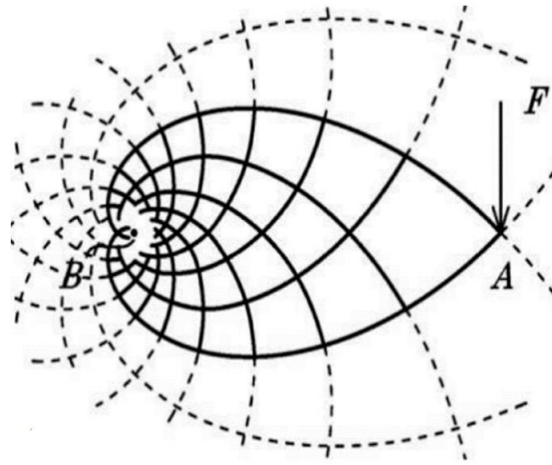


**Figure 12** - Michell cantilever structure optimisation

Michell introduced the concept of optimal structure in 1904 but almost 80 years elapsed before another methodology appeared. The main reason is related to the computational cost and calculation power availability. Indeed, Michell's equations were solvable manually only for very simple cases. However, structures are almost always characterised by a number of variables not manageable by hand calculation. Therefore, the Topology Optimisation methods as known nowadays appeared for the first time in the 80', when computational power was higher enough [28]. In Figure 13, an intuitive timeline about the main Topology Optimisation approaches is reported. Firstly, in the 80' appeared the *Homogenisation*, followed by the *density-based* and lastly by *higher-order function* methods. Along with these three main categories, others appeared during the years [22,23,29]. However, most of them can be included as a side branch of the three categories just highlighted or found minor applications. Only recently, the use of sophisticated *Artificial Intelligence (AI)* algorithms landed the Topology Optimisation field with promising but controversial results [30–32]. Not included in Figure 13, but as well important is the 'lateral' evolution of the Topology Optimisation application. Namely, the use of Topology Optimisation in different physic fields, such as thermal conduction, fluid heat and mass transfer, optics, magnetism, electrostatic and so on [33–35].

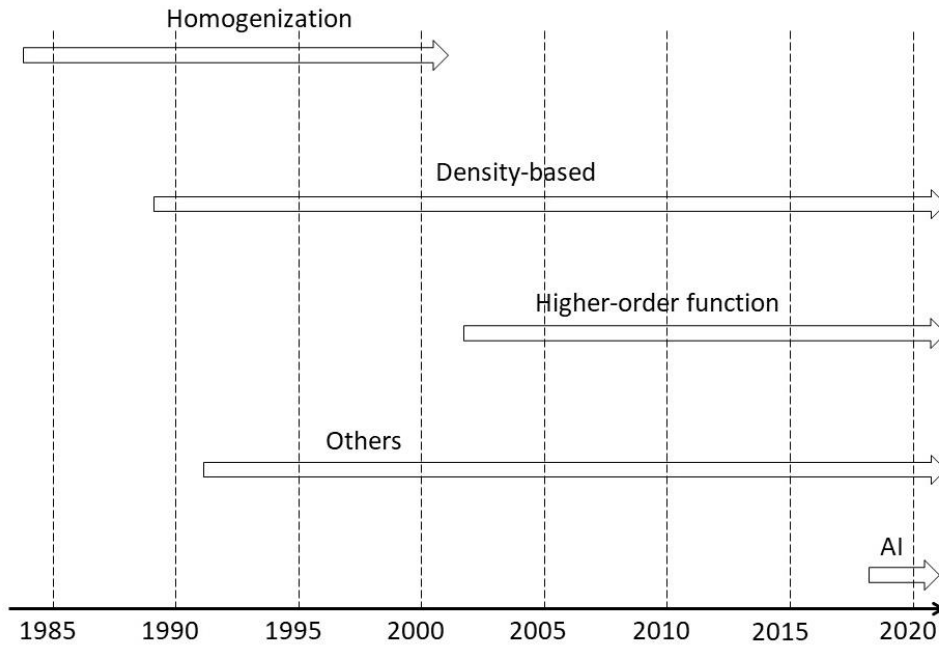


**Figure 13** - Topology Optimisation main methods timeline.

*Note: AI – Artificial Intelligence*

As already hinted, the *Homogenisation* method was the first algorithm to appear. In this method, the design domain is assumed as constituted by a periodic microstructure composed of holed unit cells. The dimensions and orientation of these holes define the domain microstructure and the overall domain behaviour. Consequently, depending on the hole size, the single unit cell has a prescribed stiffness and density. The Homogenisation method defines the relation between the hole size and the mechanical behaviour of the unit cell as a composite material [36]. In Figure 14 an example of the design domain interpretation is reported. On the left, a continuously changing microstructure defining the design domain, on the right the detail of the single holed unit cell.

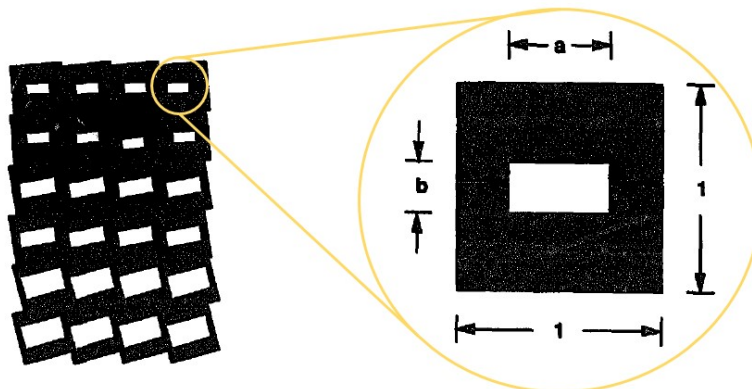


**Figure 14** - Continuous microstructure and single rectangularly holed unit cell

Following this procedure, the final output of the *Homogenisation* method consists of the size of the hole, namely  $a$  and  $b$  in Figure 14, and its orientation in the plane. The final material distribution can be defined by bulk unit cells ( $a$  and  $b$  equal to 0), void material ( $a$  and  $b$  equal to 1) or intermediate values ( $a$ ,  $b$ , and orientation variable). Nowadays, the *Homogenisation* method lost its primacy as an approach for the Topology Optimisation problems. However, it is coming back in the spotlight for specific Topology Optimisation problems. When the final component is supposed to be composed by metamaterial cells, the *Homogenisation* method is useful to describe the single cell behaviour and reduce the number of global variables [37–40].

Furthermore, the *Homogenisation* method has been the precursor of a new series of approaches, generally called *density-based* approaches [41], where the density of a point in the design domain is somehow interpolated to its stiffness. The first methodology appeared in this sense is the so-called Solid Isotropic Material with Penalization (SIMP) and it is still one of the most employed methodologies [42]. Other methods based on similar assumption were developed, such as Evolutionary Structural Optimisation (ESO), Bidirectional Evolutionary Structural Optimisation (ESO) [43], Rational Approximation of Material Properties (RAMP) [44,45]. In Figure 15 it is possible to visually understand the meaning of interpolation between stiffness  $E$  and density  $\rho$  in a design domain point, generally described by coordinates  $x$ . A detailed description of the *density-based* approaches is provided below since they are the core of the presented algorithms and the method employed in most of the available commercial software.

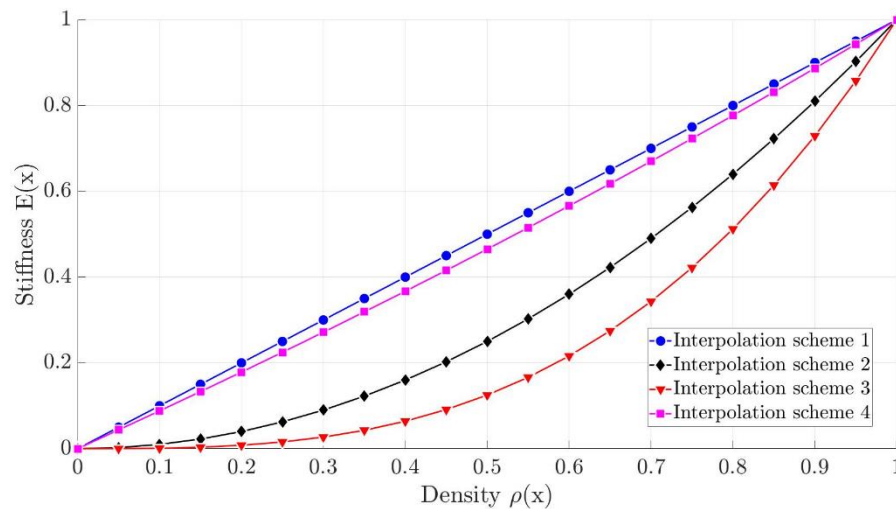


**Figure 15** - Example of interpolation scheme between density  $\rho$  and stiffness  $E$ .

After 10 years of research based on this type of material interpolation schemes, a novel methodology appeared, named *Level Set* and similar others [46]. The novelty of this method is the absence of the direct interpolation between density and stiffness. On the contrary, the entire topology, i.e., material distribution, is defined by a higher order function. Even if problematic to be described, the concept can be clearly understood thanks to Figure 16. In this

Figure, a 3D function named  $\Phi$  can assume three different values, depending on a constant parameter  $c$ . Most important, when  $\Phi = c$ , the function defines a boundary on a bidimensional plane, i.e., the domain. This condition is used to describe the topology in the domain and define the material distribution. Therefore, using this higher order function  $\Phi$ , it is possible to describe and change the topology on the 2D domain  $D$ . Similarly, using a 4D function it is possible to describe a 3D topology. Overall, the *Level Set* method is based on a more complex mathematical structure and its implementation is difficult as well. However, the *Level Set* method has found interesting applications mainly in problems where the physics depends directly on the boundary [47–49]. For example, most of the problems including a fluid with mechanical or thermal properties are strictly related to the boundary. In the *density-based* methods there is no analytical function describing the boundary. The boundary is the result of the transition between elements with null and full density. Whereas, for elements with intermediate densities it can be extremely difficult to be defined. On the contrary, in the *Level Set* method the boundary has an analytical definition by implementation. Therefore, it can be straightforwardly used to model the component behaviour.

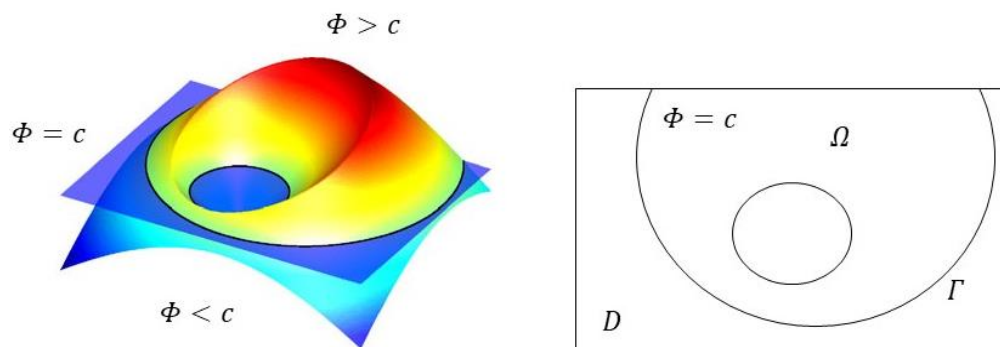


**Figure 16** - Level Set design domain interpretation by higher order function

The three main debrided methods are related to the approach the topology optimisation is carried out. It concerns the second phase explained in the previous paragraph. Indeed, these methods are used to setup the Topology Optimisation problems. However, the minimisation problem used to find the optimal material distribution has not been yet addressed, i.e., the third phase previously defined.

There are two main categories of inner minimisation problem solvers. The Gradient Based (GB) solvers and the Non-Gradient Based (NGB) solvers. The first evaluates the derivatives of the objective function and the constraints with respect to the design variables (material distribution), whereas the second bypasses this calculation. As stated in [32], the NGB presents many issues, especially the huge computational cost for larger system. Indeed, the most common method to bypass the gradient evaluation is using a huge amount of data and train some machine learning algorithm. These methods are known in the literature as Genetic Algorithms, Differential Evolution, Simulated Annealing and

so on. Overall, it seems that the GB algorithms, even if characterised by tricky derivatives evaluation, are the most suitable for the Topology Optimisation solution. Indeed, the majority of the Topology Optimisation approaches are solved by means of GB solvers, such as MMA.

However, some specific Topology Optimisation problems may require NGB methods to be solved, especially when discontinuities are present and the derivatives may not be evaluable. Furthermore, non-connected design spaces and Topology Optimisation problems with many local minima may take advantages from NGB solvers. Indeed, in the last years *AI*-based Topology Optimisation are appearing and they promising for solving specific and complex problems [50–54].

This brief description about Topology Optimisation evaluation, approaches and solvers is intended to be an introduction to the following part. Obviously, this is just scratching the surface of the vast possibilities and developments made in the Topology Optimisation field. However, it is useful to locate in the Topology Optimisation panorama the *Top* algorithms presented in this dissertation. All the *Top* algorithms belong to the *density-based* approach. The reason is that this is the most direct approach for the Topology Optimisation problem and the most employed. Since the purpose of this dissertation is to provide to the AM environment useful dedicated design tools, it has been decided to develop the *Top* algorithms in most accessible manner.

Furthermore, the Topology Optimisation problems are solved using GB methods. The reason in this case is double. First, computational cost is a critical issue in the AM industry, so its reduction is critical and beneficial for the AM development. Second, the addressed problems are characterised by continuous variables, or at least not discontinues, and do not require specific NGB solvers. Anyway, it is worth to be noticed that all the problems addressed by the *Top* Suit can be solved using other approaches and solvers.

Overall, the *Top* Suit belongs to the *density-based / gradient-based* Topology Optimisation. Therefore, below a detailed description of this approach is carried out together with related issues and adjustments.

## 1.2.2 Density-Based / Gradient-based Topology Optimisation

In this paragraph, the *density-based* Topology Optimisation approach is introduced. The Topology Optimisation problem is solved in the generic structural field to analyse critical aspects of method. Further details are reported in the related section for each *Top* algorithm.

The first step is the definition of a *Design Domain*  $D$ , a portion of the space (both 2D and 3D) where the material can be distributed. The boundary of the domain  $D$  is named  $\Gamma$ . On the boundary  $\Gamma$  some conditions are imposed, such as applied loads  $F$  or fixed displacement. Since, Finite Elements (FE) are used to discretise and model the domain  $D$ , the Topology Optimisation problem is formulated accordingly [11]. Therefore, the full domain  $D$  can be considered discretised in  $N_{elem}$  finite elements. For each element  $e$ , a design variable  $\rho_e$  can

be defined. The design variable  $\rho_e$  is defined as the element density variable. As a notation remark, **bold** symbols refer to vector or matrix quantity. For example,  $\boldsymbol{\rho}$  stands for the vector containing all the element densities, as reported in Eq.1.

$$\boldsymbol{\rho} = [\rho_1 \quad \dots \quad \rho_e \quad \dots \quad \rho_{N_{elem}}] = \rho_e \text{ with } e = 1, \dots, N_{elem} \quad (1)$$

The meaning of the density variable  $\rho_e$  is essentially the presence or not of the element itself. In other words, the density variable  $\rho_e$  is thought to be constrained in an interval. In case the density is the minimum, usually zero, the element is considered as void material. In case the density is maximum, the element is considered as full material. Overall, the vector  $\boldsymbol{\rho}$  contains all the value of the design variables  $\rho_e$  and therefore the material distribution in the domain  $D$ . In Figure 17 quantities are visually represented. In Figure 17 it is possible to visualise the quantities just described. In addition to the design variables  $\boldsymbol{\rho}$ , another set of variables is present, named state variables. In other words, these are the variable stating the behaviour of the domain.

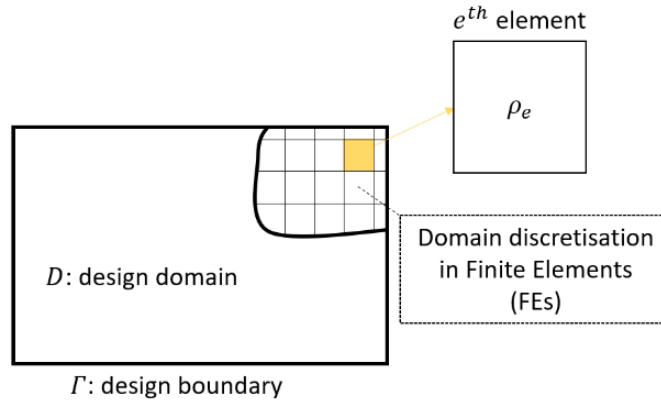


**Figure 17** - Design Domain and related quantities

Referring to structural topology optimisation and in particular to minimum compliance optimisation, the state variable is the overall displacement  $\boldsymbol{U}$ . Supposing to have a number of node equal to  $N_{node}$ , the vector  $\boldsymbol{U}$  is defined as on Eq.2.

$$\boldsymbol{U} = [U_1 \quad \dots \quad U_n \quad \dots \quad U_{N_{node}}] = U_n \text{ with } n = 1, \dots, N_{node} \quad (2)$$

The variables  $\boldsymbol{U}$  and  $\boldsymbol{\rho}$  are linked by the state equation governing the analysed system. In particular, for given and fixed values of the design variables, the state equation provides the values for the state variables. Thanks to these variables it is possible to describe the *density-based* Topology Optimisation in the structural field as in Eq.3.

$$\begin{aligned} & \min_{\rho, U} \phi(\rho, U) \\ & s. t. \begin{cases} g_i(\rho, U) \leq \bar{g}_i & \text{with } i = 1, \dots, M \\ \rho_{min} \leq \rho_e \leq \rho_{MAX} & \text{with } e = 1, \dots, N_{elem} \\ \mathbf{K}(\rho)\mathbf{U} = \mathbf{F} \end{cases} \end{aligned} \quad (3)$$

Where  $\phi$  is the objective function,  $g_i$  is a constraint function and  $\bar{g}_i$  the related threshold,  $M$  is the number of total constraints,  $\rho_{min}$  is the minimum value for the design variable, usually 0,  $\rho_{MAX}$  is the maximum value for the design variable, usually 1,  $\mathbf{K}$  is the global stiffness matrix via FE analysis,  $\mathbf{F}$  is the global load vector via FE analysis. The problem as written in Eq.3 is known as Simultaneous Analysis and Design (SAND) formulation because the state equation  $\mathbf{K}(\rho)\mathbf{U} = \mathbf{F}$  is included as constraining equation in the Topology Optimisation problem. Anyway, usually the solution of the state equation is carried out aside the Topology Optimisation problem and verified by the FE solver. Indeed, another formulation is more likely to be employed named Nested Analysis and Design (NAND) formulation, as expressed in Eq.4.

$$\begin{aligned} & \min_{\rho, U} \phi(\rho, U) \\ & s. t. \begin{cases} g_i(\rho, U) \leq \bar{g}_i & \text{with } i = 1, \dots, M \\ \rho_{min} \leq \rho_e \leq \rho_{MAX} & \text{with } e = 1, \dots, N_{elem} \end{cases} + \mathbf{K}(\rho)\mathbf{U} = \mathbf{F} \end{aligned} \quad (4)$$

In this formulation, the Topology Optimisation is solved iteratively interspersed by FE analysis where the state equation is verified. This solution is the mostly employed since reduces remarkably the complexity of the optimisation problem.

The problem as formulated is named *continuous* or *relaxed*. Indeed, the design variables are free to change continuously between the minimum and the maximum value. However, in order to have a clear topology on the end of the optimisation, the final distribution of  $\rho$  should be discrete made of 0 and 1. For example, a very simple topology is reported in Figure 18, and show the final topology individuated by the discrete distribution of void and full elements.

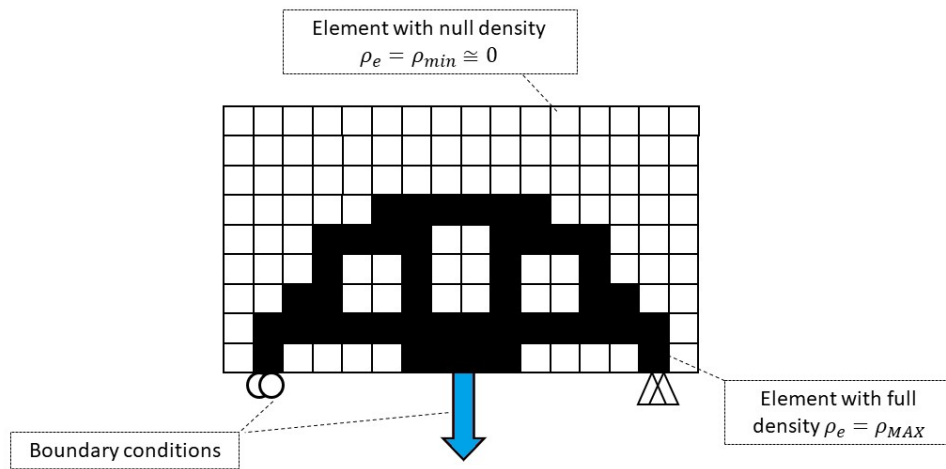


**Figure 18** - Example of simple discrete topology by *density-based* methods

All considered, the problem should be written in a discrete form since the intermediate densities are not admissible in the final result. The discrete formulation is written in Eq.5 below.

$$\begin{aligned} & \min_{\rho, \mathbf{U}} \phi(\rho, \mathbf{U}) \\ \text{s. t. } & \begin{cases} g_i(\rho, \mathbf{U}) \leq \bar{g}_i & \text{with } i = 1, \dots, M \\ \rho_e = \begin{cases} \rho_{min} \\ \rho_{MAX} \end{cases} & \text{with } e = 1, \dots, N_{elem} \end{cases} \quad + \quad \mathbf{K}(\rho)\mathbf{U} = \mathbf{F} \quad (5) \end{aligned}$$

However, the possible combination of discrete values of design variable in this form follows a factorial function. Indeed, for a very limited number of elements, such as 5000, the number of possible combinations raises up to  $10^{29}$  [32]. In addition, NGB approaches are usually based on this type of formulation and this is the reason why they are so computationally expensive.

All considered, the NAND formulation in Eq.4 is the most suitable for the Topology Optimisation solving. However, the continuous formulation does not ensure a clear ‘black and white topology’. If the problem would be solved as it is, the final result may be characterised by intermediate densities since there is no prescriptions on that. This concept can be visually understood looking at Figure 19. Indeed, ‘grey’ scale density distribution characterises the final topology.

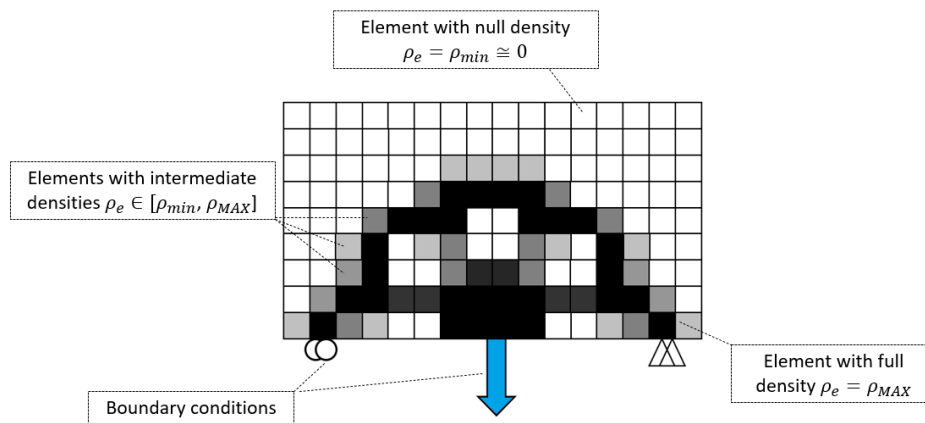


**Figure 19** - Example of simple continuous topology by *density-based* methods

In order to solve this problem, as already mentioned before, the solution consists of interpolating with a penalty factor the density and the stiffness. In other words, for low values of the density variable, the related stiffness is penalised, and the element tends to have less and less importance, up the lower density value during the Topology Optimisation. On the contrary if the element has higher values of density, the related stiffness is rewarded, and the element tend to have more importance during the Topology Optimisation up to its maximum value. In this sense, two main categories of interpolation are used. One is named Solid Isotropic Material with Penalization (SIMP) and the interpolation

between density and stiffness is exponential. The other one is named Rational Approximation of Material Properties (RAMP) [45] and the interpolation is rational. In Eq.6 the two interpolation equations are reported.

$$\begin{aligned}
 SIMP &\rightarrow E(\rho_e) = \rho_e^p E_0 \\
 RAMP &\rightarrow E(\rho_e) = \frac{\rho_e}{1 + q(1 - \rho_e)} E_0
 \end{aligned} \tag{6}$$

Where,  $E$  is the interpolated stiffness,  $p$  is the exponential factor usually,  $E_0$  is the material original stiffness,  $q$  is the rational coupling factor. Both interpolation schemes are quite used in the literature. However, the SIMP methodology found more application and it is spread in commercially available software as well. For this reason, the description below is focused on the SIMP approach. Anyway, the same consideration can be done with the RAMP interpolation scheme as well. The two interpolation are visually represented in Figure 20, as it can noticed they quite similar.

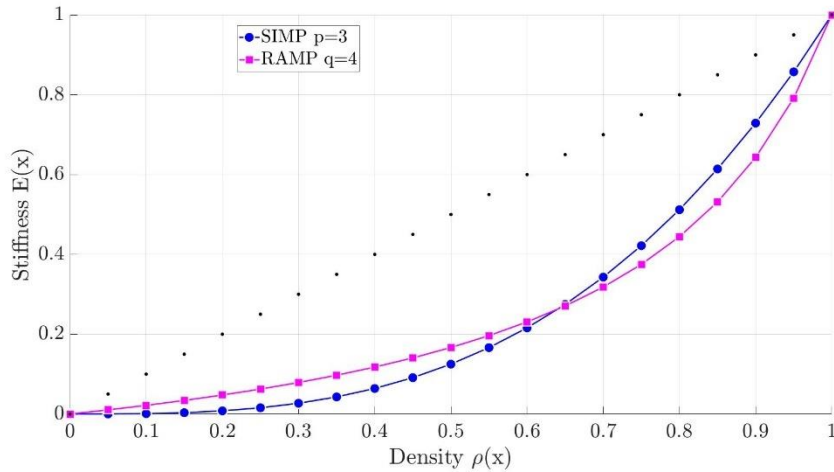


**Figure 20** - SIMP and RAMP interpolation scheme for density and stiffness.

Note: point line indicate linear interpolation.  $E_0$  is set to 1,  $\rho_{min}$  equal to 0,  $\rho_{MAX}$  equal to 1.

As a consequence of this interpolation the original problem in Eq.4 changes as reported in Eq.7.

$$\begin{aligned}
 &\min_{\rho, U} \phi(\rho, U) \\
 &s. t. \begin{cases} g_i(\rho, U) \leq \bar{g}_i & \text{with } i = 1, \dots, M \\ \rho_{min} \leq \rho_e \leq \rho_{MAX} & \text{with } e = 1, \dots, N_{elem} \end{cases} \\
 &+ \begin{cases} \mathbf{K}(\rho)\mathbf{U} = \mathbf{F} \\ E(\rho_e) = \rho_e^p E_0 & \text{with } e = 1, \dots, N_{elem} \end{cases}
 \end{aligned} \tag{7}$$

It is worth noting that this type of interpolation works for isotropic elastic material. Indeed, for composite, anisotropic or non-elastic materials this interpolation scheme would be different as will be detailed thereafter. Under this limitation, the stiffness matrix can be expressed as reported in Eq.8.

$$\mathbf{K}(\boldsymbol{\rho}) = \sum_e \mathbf{K}_e(\rho_e) = \sum_e \rho_e^p \mathbf{K}_e^0 \quad (8)$$

Where  $\mathbf{K}_e$  is the element stiffness matrix and  $\mathbf{K}_e^0$  is the element stiffness matrix considering the base material property, i.e.,  $E_0$ .

The penalty factor  $p$  can assume different values, indeed there is no restriction on it expect for being at least unitary. The penalty factor  $p$  can be chosen experimentally. In other words, it can be suited for the specific Topology Optimisation problem addressed.

For example, the problem in Eq.6 for minimum compliance ( $\phi(\boldsymbol{\rho}, \mathbf{U}) = \mathbf{F}^T \mathbf{U}(\boldsymbol{\rho})$ ), volume constrain of 50%, penalty factor  $p$  equal to 1, 800 squared unitary quad elements, shape ratio 2:1, density values belonging to the 0-1 interval, unitary force,  $E_0$  unitary. The solving algorithm can be easily coded such as in [55] using optimality criteria.

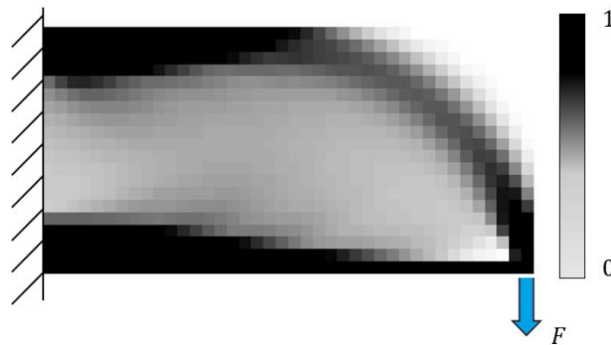


**Figure 21** - Final topology without penalisation

As it can be seen in Figure 21, most of the element present intermediate densities. Indeed, the linear interpolation provide a grey-scale solution which poorly fit real applications. The intermediate densities can be interpreted as different microstructures. In other words, each element can be considered as composed by a particular distribution of void and bulk material in order to have the prescribed density by the Topology Optimisation [42]. An entire branch of the Topology Optimisation has been developed with the aim of concurrently optimising the macro and micro material distribution and it is usually named *multi-scale* Topology Optimisation [56]. For other applications, where the final topology must be characterised by bulk material only, the penalty factor must be greater than 1 and usually it is set to 3. It is worth noting that this value is not prescribed, however applications demonstrated that  $p$  equal to 3 provides the most performant results. For higher values, the penalisation is so strong that forces the solution to fall into local minima. Overall, the use of the penalisation factor permit to obtain discrete solutions at the cost of introduction its variability.

The presence of local minima is the first of a series of problems related to the use of the SIMP approach, and more generally the *density-based* approaches. Other main issues are the *checkerboard* effect, the *mesh dependency*, and the *grey-scale* solution [57]. In the following paragraph, a detailed explanation of these problems are reported together with the related solutions.

The system in Eq.4 can be solved using a linear interpolation for a certain category of problems, such as the minimum compliance under volume constraint [58]. This solution is useful because is much easier to be implemented, it reduces the computational efforts and the number of variables to be defined. However, for more complex problems, especially hardly constrained ones, this solution is no more efficient and the SIMP or RAMP method have to be employed.

Independently from the interpolation scheme used, the problem in Eq.4 requires to be solved. As already hinted before, there are two main categories of solvers to be employed. The first method is the *gradient-based* (GB) method and it exploit the gradient evaluation to look for the minimum. The second method is the *non-gradient-based* (NGB) method where the minimum is searched without the gradient evaluation. About the NGB solvers, in [32] their application is hardly tackled, especially for the greater amount of computational power required compared to GB methods. Some exceptions are present to this general statement, but they are not fitting the *Top Suite* applications.

Hence, all the problems presented in this dissertation are solved using GB method. In particular, for *TopTM* and *TopComp* the gradient evaluation is carried out in the problem setup phase following the method proposed in [58]. Therefore, there is no need to evaluate it again in all the optimisation problem. It is worth noting that this reduces remarkably reduces the computational cost. As for *HyperWorks*, the problem is hardly constrained and therefore the SIMP interpolation scheme is used. In this case, the gradient must be evaluated (sensitivity analysis) during the optimisation iteratively and then employed to solve the minimisation problem.

The gradient evaluation is usually done with the *adjoint sensitivity* analysis rather than using the finite *difference-based sensitivity* analysis. This second numerical method is extremely precise, but it is much more expensive. The *adjoint sensitivity* analysis will be detailed in the *HyperWorks* related paragraph.

### 1.2.3 Numerical Instabilities in Topology Optimisation

As already hinted in the previous paragraph, *density-based* approaches are characterised by a series of problems which affect the Topology Optimisation solution [57].

Below a detailed discussion of these problems is reported. It is useful to understand the criticalities of the *density-based* Topology Optimisation and how the *Top Suite* respond to these issues.

## Checkerboards

The checkerboard effect is the presence of a checkerboard fashion in final topology. Mainly, adjacent elements results to be connected only by corners, poorly modelling the real component behaviour. The checkerboard effect is caused by a numerical instability due to the interaction between the Topology Optimisation solver and the FE analysis [59]. Indeed, two main aspects come into account when a Topology Optimisation for structural stiffens maximisation is considered. Trivially, the overall stiffens of the structure must be maximised and therefore every density distribution which supports this objective is rewarded. Furthermore, the Topology Optimisation should be as cheap as possible in terms of computational power. Consequently, low order elements are preferred to limit the number of degrees of freedom (DoF) to evaluate. The results of these two aspects lead to final topologies characterised by black and white alternate elements in a checkerboard pattern. For example, solving the same problem reported in Figure 21 but with a penalty factor of 3, the final topology is poorly defined as reported in Figure 22.



**Figure 22** - Checkerboard effect on final topology

As a matter of fact, linear quad elements have been used to solve the FE analysis [55]. These elements are preferred due to their low number of DoF compared to higher order elements. However, from a numerical point of view, the checkerboard pattern is characterised by a higher stiffness and the poor connection, namely corner to corner, is not realistically modelled.

In order to solve this problem, many approaches have been developed. Mainly, the use of higher order elements or a *filtering* technique. The employment of higher order elements is easier and increase the overall accuracy. However, the computational cost of the Topology Optimisation is at least doubled. Indeed, the number of DoF is increased of about twice and for large system this may be extremely expensive.

For this reason, the *filtering* technique is preferred and one of the most employed methodology. Furthermore, the *filtering* technique solves another problem, i.e., the mesh dependency as detailed thereafter.

The *filtering* technique consists of using a filtered design variable instead of the real one. In other words, during the optimisation setup the design variable  $\rho$  is substituted by a filtered  $\tilde{\rho}$  [60]. The relationship between these two variables is reported in Eq.9.

$$\begin{cases} \tilde{\rho}_e = \frac{\sum_{i \in \Omega_e} H_{ei} \rho_i}{\sum_{i \in \Omega_e} H_{ei}} & \text{with } e, i = 1, \dots, N_{elem} \\ H_{ei} = R - \|\mathbf{x}_i - \mathbf{x}_e\| \\ \Omega_e = \{i \mid \|\mathbf{x}_i - \mathbf{x}_e\| \leq R\} \end{cases} \quad (9)$$

Where,  $\Omega_e$  is the neighbourhood of the element  $e$ ,  $H_{ei}$  is a weighting function,  $\mathbf{x}_i$  is the location vector between of element  $i$ ,  $\mathbf{x}_e$  is the location vector between of element  $e$ ,  $R$  is the filtering radius. Basically, the design variable is smoothed over the closest elements according to the filtering radius. This procedure is visually represented in Figure 23.

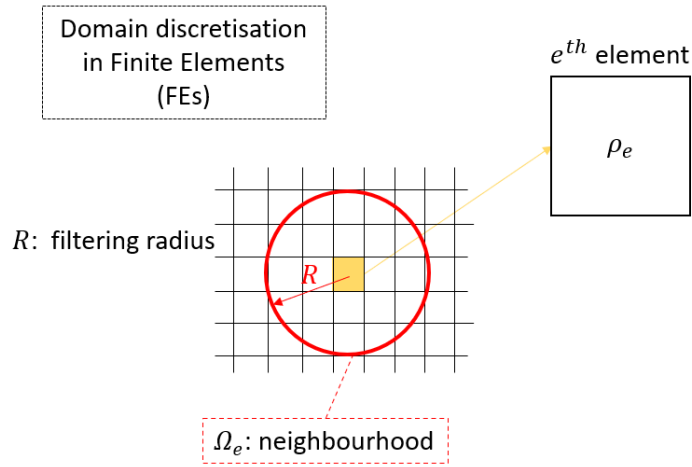


**Figure 23** – Filtering techniques and element neighbourhood

Overall, the filtered density is used in the whole procedure to evaluate the component domain properties and performance response. Eq.6 for the SIMP approach is therefore modified according to the filtering as reported in Eq.10.

$$E(\rho_e) = \tilde{\rho}_e^p E_0 \quad \text{with } e = 1, \dots, N_{elem} \quad (10)$$

However, it must be noticed that during the minimisation problem phase, the design variables remain the unfiltered ones. Consequently, the use of the chain rule to evaluate the sensitivity is required. More detail are provided d in the related section in the *HyperWorks* discussion.

Looking at the problem solved in Figure 22, it is sufficient to implement the detailed filter and imposing a filtering radius of 1.5 time the element size to solve the checkerboard effect. The result is reported in Figure 24.

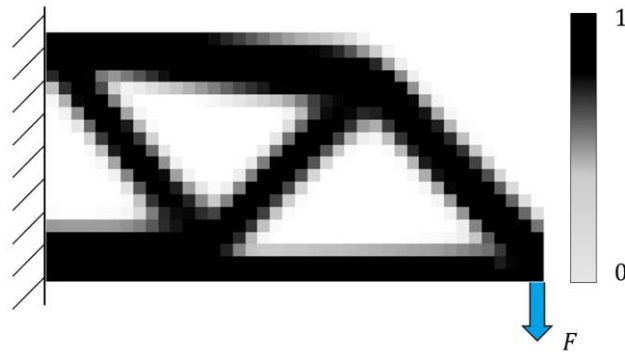


**Figure 24** - Checkerboard solution by filtering approach

The solution reported in Figure 24 is clear and well defined. The checkerboard pattern is absent, and the topology is correctly modelled. The increase in computation time is inferior compared to the higher order element solution counterpart [11].

Even if the filtering technique involves great advantages, some drawbacks are present. First of all, the filtering radius  $R$  is another parameter to be defined empirically. Indeed, there is no analytical procedure which can assess a precise value for this variable. Similarly to the penalty factor  $p$ , the filtering radius must be chosen accordingly to other factors case by case. Sometimes, the radius may be set the minimum manufacturable thickness during the production phase but is not an exhaustive and comprehensive solution. Overall, this raises the need for human interaction which may suffer from design bias. Furthermore, the more the filtering radius is high the more the number of intermediate densities is present in the final topology. In particular, the boundary of the individuated final topology may be characterised by blurred and fuzzy which can create issues in the component realization. Again, this may require the human interaction and interpretation which should be limited as much as possible. This last drawback can be limited by using the so-called *projection* method, as detailed below in the related section.

## Mesh dependency

When the Topology Optimisation is carried out on certain design domain, the optimal topology should be unique. Indeed, the optimisation should provide the globally optimum material distribution. Therefore, the material distribution should not depend on the domain discretisation. In other words, the problem should be independent from the number of elements  $N_{elem}$ . However, this is not true for most of the cases. For example, it is possible consider a cantilever beam and solve the problem in Eq.6 for minimum compliance ( $\phi(\boldsymbol{\rho}, \mathbf{U}) = \mathbf{F}^T \mathbf{U}(\boldsymbol{\rho})$ ) under a volume constrain of 50%, penalty factor  $p$  equal to 3, squared unitary quad elements, shape ratio 3:1, density values belonging to the 0-1 interval, unitary force,  $E_0$  unitary [55]. The result is shown in Figure 25 and the Topology Optimisation is carried out considering 675, 1200 and 2700 elements respectively. As it can be noticed, the more the number of elements is increased, i.e. mesh refinement, the more the final topology changes. In particular, smaller features

tend to appear and a more complicated truss-like structure is present. This mesh-dependency [57] is not a numerical misinterpretation. on the contrary, it is the logical path followed by the Topology Optimisation solver. As a matter of fact, the structure obtained with 2700 elements is stiffer, justifying this final topology. As an additional proof, this tendency is the same found in natural structures such as bones or wood fibres. Usually, these intricated structures with small features are present more than bulky compact ones.

Nevertheless, this mesh dependency is not acceptable for most of Topology Optimisation industrial applications. First, because too little features may not be producible by manufacturing systems. Second, because it must be the possibility to refine the mesh and increase the mesh accuracy without obtaining different final solutions.

In order to solve this problem, many approaches have been developed during the years. Some of them are based on surface limitation to prevent having too many holes, i.e. many thin structures, such as the *perimeter control* or the *gradient control*. However, these solutions are often weak, and it is very difficult to predict a maximum free surface of the final topology.

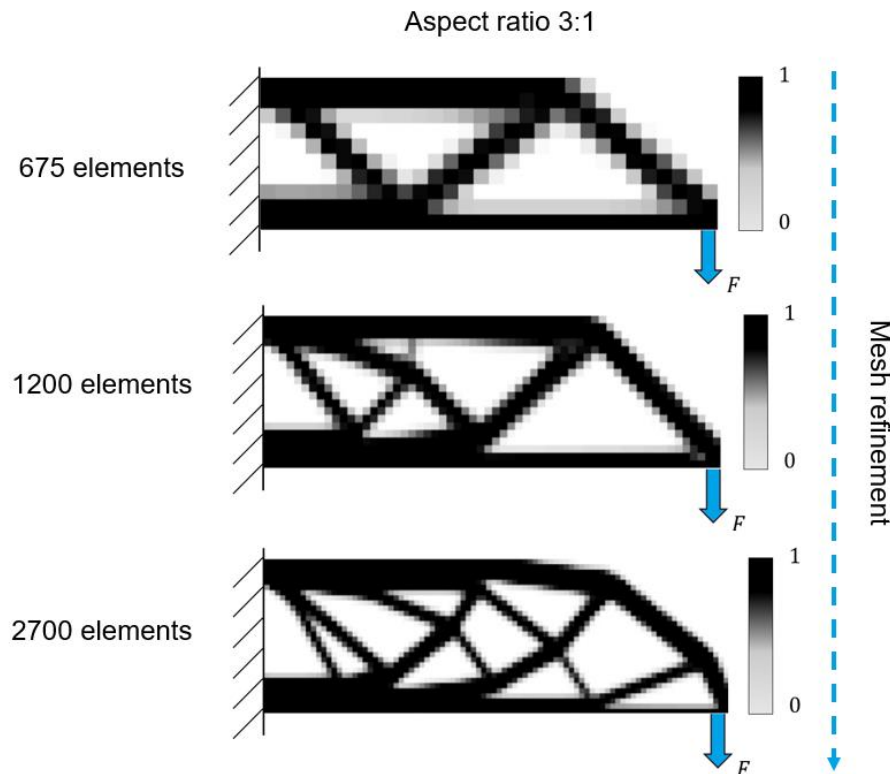


**Figure 25** - Mesh dependency and feature refinement

Indeed, the most suitable techniques to avoid mesh dependency is the already introduced *filtering* method. Using the same filter defined in Eq.9, the final topology is automatically free by the mesh-dependency effect. Using a filtering equal to 2 times the element size, the same topology optimisations carried out in Figure 25 result to be completely different. The results are reported in Figure 26.

As it can be seen, the three different solutions share the same structures, independently by the mesh refinement. Overall, the discretisation increase the solution accuracy, but it does not affect the Topology Optimisation result.

As already hinted previously, the filtering radius should be defined somehow. However, an analytical procedure does not exist, and this value can be chosen only case by case. A possibility is to link the filter radius to the minimum manufacturable thickness in the production process. However, this data is not always available, and it may be inferior to minimum element size, leading to inactive filtering. Furthermore, as it can be seen in Figure 25 and Figure 26, the filtered solution present fuzzy and not clear boundaries. These grey zones must be interpreted by designers and lead to possible misunderstandings.

These filter-induced undefined grey zones can be eliminated using a *projection* method that will be discussed hereafter.

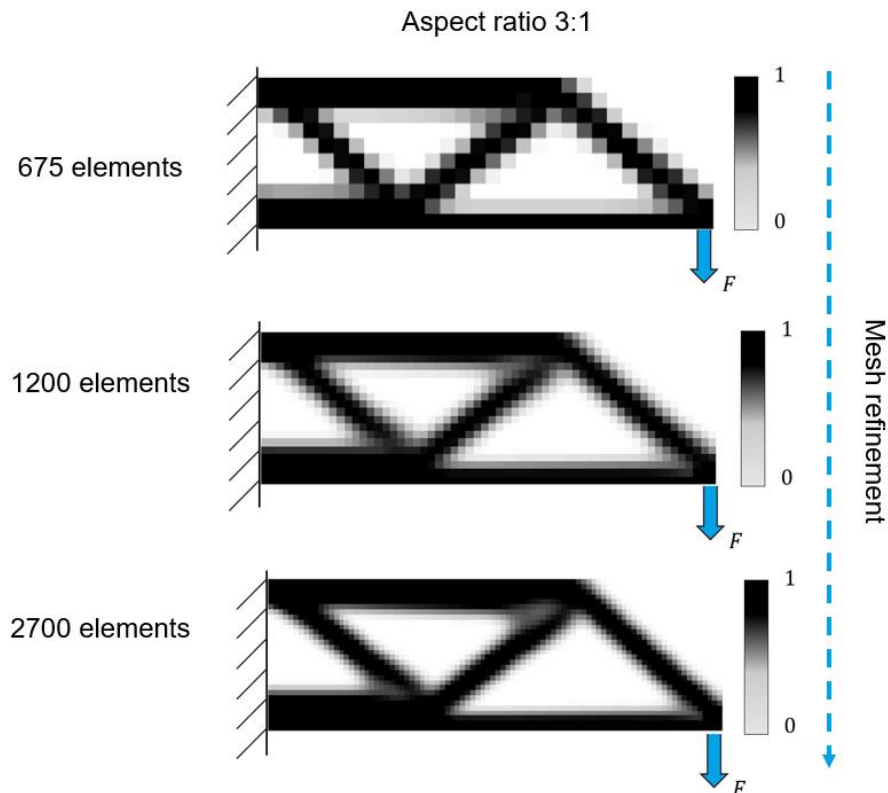


**Figure 26** - Mesh independency by filtering technique

### Undefined grey zones

With the aim of solving the mesh dependency and the checkerboard effect, a filtering technique is used. Even if this solution is well working and solves these problems, some drawbacks are present. First, the lack of a precise methodology to choose the filtering radius. Second, the presence in the final topology of fuzzy boundaries and grey zones. The first problem may be partially solved looking at manufacturing constraints. The second must be solved forcing these intermediate densities to fall into the interval extremes, i.e., 0 or 1.

In order to do that, a procedure named *projection* technique is employed. In particular, the filtered density  $\tilde{\rho}_e$  is substituted with a projected  $\overline{\tilde{\rho}_e}$  defined as reported in Eq.11.

$$\overline{\tilde{\rho}_e} = \frac{\tanh(\beta\rho_0) - \tanh(\beta(\tilde{\rho}_e - \rho_0))}{\tanh(\beta\rho_0) + \tanh(\beta(1 - \rho_0))} \quad (11)$$

Where  $\beta$  is a projection parameter which controls the effect of the projection and  $\rho_0$  is the threshold parameter. The projection erases the ‘grey’ zones, fostering the “black or white” solution [61]. This projection function forces the filtered densities to be full or void material and has great effect on the aforementioned grey zones. The factor  $\beta$  controls how harder the densities are projected. Therefore, for lower values the projection is light and less effective. For greater values the projection is hard and strongly affect the density value. The threshold parameter  $\rho_0$  is usually set at 0.5, or more generally at the average of  $\rho_{min}$  and  $\rho_{MAX}$ . In Figure 27 is visible the effect of the projection especially on the thin branches of the topology. This design is on the most classical employed in the Topology Optimisation. The left side has a fixed temperature  $T$  while the whole plate is uniformly heated by the heat flow  $Q$ . Aim of the Topology Optimisation is to maximise the heat exchange under a volume constraint. More details are reported in [62–64]. As it can be seen, the left topology is fuzzy and difficult to be interpreted. On the contrary, the right topology is perfectly clear and it does not require any human interpretation [62].

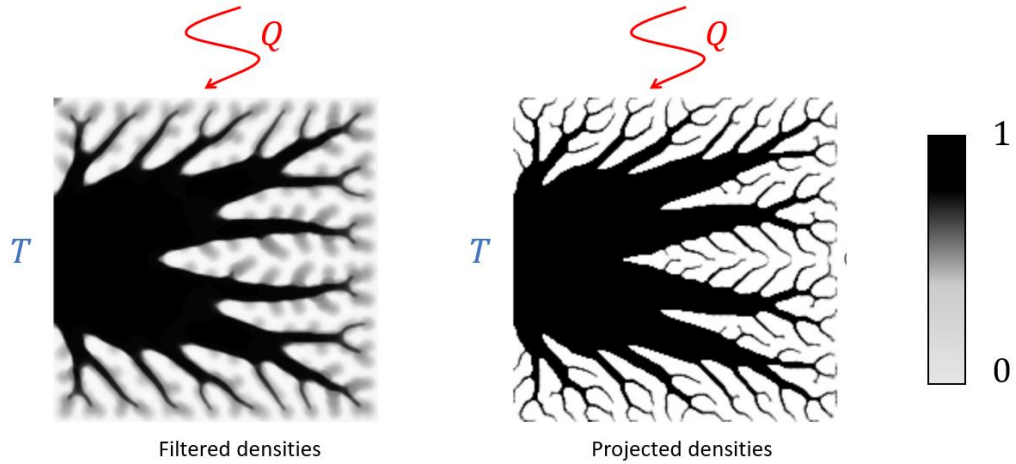


**Figure 27** - Effect of density projection on classical heat transfer case

Overall, the projected density, exactly the filtered one, is used in the whole procedure to evaluate the component domain properties and performance response. Eq.6 for the SIMP approach is therefore modified according to the filtering as reported in Eq.12.

$$E(\rho_e) = \overline{\tilde{\rho}_e}^p E_0 \quad \text{with } e = 1, \dots, N_{elem} \quad (12)$$

Another possible solution to intermediate densities may be raising the penalty factor  $p$  up to 5 or more. However, this solution hardly affects the optimisation stability, making the process unstable and divergent.

## Local Minima

In order to solve the Topology Optimisation and solve the aforementioned problems, many numerical factors have been introduced, mainly the penalty factor  $p$ , the filtering radius  $R$  and the projection parameter  $\beta$ . Hence, the process is strongly dependent from their numerical values. Overall, the initial problem becomes more and more non-convex, and many local minima may appear. In other words, changing the values of these parameters different sub optimal solutions are likely to appear. The more common solution to avoid local minima is to slowly increase the values of this parameters during the optimisation. For example, it is possible consider a cantilever beam and solve the problem in Eq.6 for minimum compliance ( $\phi(\boldsymbol{\rho}, \mathbf{U}) = \mathbf{F}^T \mathbf{U}(\boldsymbol{\rho})$ ) under a volume constrain of 50%, penalty factor  $p$  equal to 3, 800 squared unitary quad elements, shape ratio 2:1, density values belonging to the 0-1 interval, unitary force,  $E_0$  unitary [55]. The result is shown in the upper part of Figure 28. Even if this solution may seem optimal, the initial value of  $p$  equal to 3 may have forced the topology to fall into a local minimum.

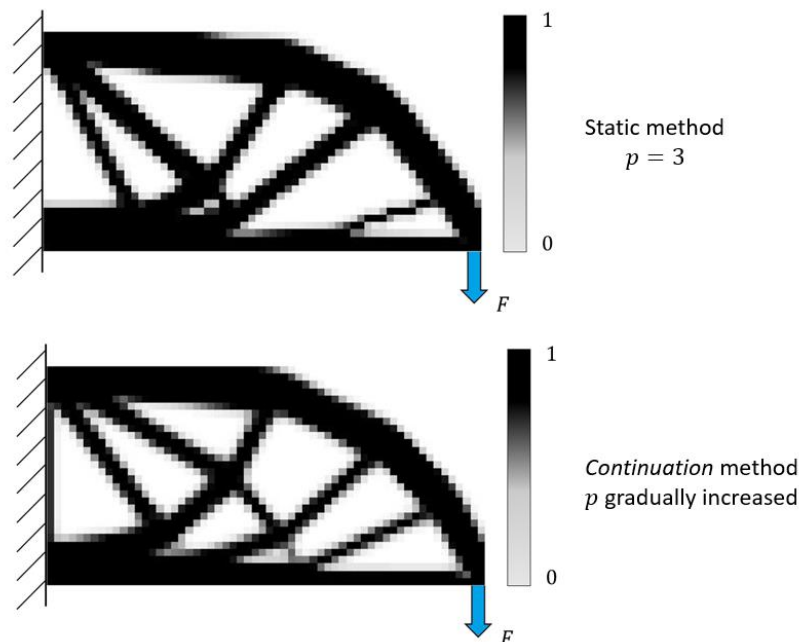


**Figure 28** - Topology optimisation with continuation method

For this reason, the topology in the lower part of Figure 28 is obtained increasing slowly the value of  $p$  iteration by iteration according to Eq.13.

$$p = \min\{1 + \text{floor}((iter - 1)/3) \cdot 0.1, 3\} \quad (13)$$

Where *iter* is the current iteration. As it can be noticed, the solution is quite different and 4% stiffer.

Overall, the continuation method can be applied on the penalty factor *p*, the filtering radius *R* and the projection parameter  $\beta$ . This relaxes the problem and prevents possible local minima during the optimisation. However, Eq.13 has no analytical definition, basically it has been found to be suitable for this type of problem [65]. All the numbers included in the Equation are arbitrary and their choice is based on human intuition.

### 1.2.4 The *Top Suite*

The *Top Suite* is included within the frame of *density-based / gradient-based* Topology Optimisation. The *Top Suite* is composed by three different Topology Optimisation algorithms. The first one is named *TopTM* and solve the coupled problem of thermo-mechanical Topology Optimisation. Aim of *TopTM* is to maximise the heat exchange and the structural stiffness of the part concurrently. As discussed later this coupled Topology Optimisation is extremely useful for industrial applications and a dedicated solver was missing in the literature before *TopTM*. The algorithm is formulated in the *density-based* approach without material penalisation. This avoid the use of the material interpolation factor, preserving the convexity of the problem. As a consequence, the Topology Optimisation problem is solved with the optimality criterium which leads to the global optimum of the structure. In this manner, the problems related to local minima and grey zones are removed. The checkerboard effect and the mesh-dependency are solved using higher order element rather than filtering. The reason behind this choice lays on the fact that *TopTM* is aimed at industrial applications. In other words, the code is thought to be simple and of straightforward implementation using commercially available software. As it is coded, the algorithm remains in few lines of code whereas the use of filtering or more complex features would require greater coding expertise. The same consideration can be carried out on the second algorithm, *TopComp*. This algorithm is able to optimise fibre reinforced composite materials. It is based on two different optimality criteria, one for the material distribution and one the fibre orientation which combined create the global optimal solution. Before *TopComp* the available codes for carrying out this type of coupled of optimisations were complex and sub optimal.

The last algorithm *HyperWorks* can include the AM process induce defect influence on the fatigue response of the part within the Topology Optimisation procedure to obtain reliable designs. Differently, *HyperWorks* requires a different approach. Mainly due to the fact that the problem is formulated with two stress

constraints. These constraints are extremely difficult to be treated within the Topology Optimisation. Furthermore, there is no evidence that an optimality criterium can be extrapolated analytically. Therefore, *HyperWorks* is solved using the SIMP approach and the method of moving asymptotes. The various related problems are solved using filtering, projection and continuation method as explained in the previous paragraph. Overall, the algorithm is coded in Matlab with more than three thousand code lines. Since this implementation limits remarkably the industrial applicability, a methodology to implement the *HyperWorks* algorithm as a procedure in the commercially available software *HyperWorks* is outlined.

In Table 1 a resuming table with the most important aspects of each Top algorithm is reported.

	<i>TopTM</i>	<i>TopComp</i>	<i>HyperWorks</i>
<b>Approach</b>	<i>Density-based Without penalisation</i>	<i>Density-based Without penalisation</i>	<i>Density-based With penalisation</i>
<b>Solver</b>	<i>Gradient-based</i>	<i>Gradient-based</i>	<i>Gradient-based</i>
<b>Method</b>	<i>Optimality Criteria</i>	<i>Optimality Criteria</i>	<i>Method of Moving Asymptotes</i>
<b>Checkerboard</b>	<i>Higher Order Elements</i>	<i>Higher Order Elements</i>	<i>Linear Filter</i>
<b>Mesh-dependency</b>	<i>Minimum element size</i>	<i>Minimum element size</i>	<i>Linear Filter</i>
<b>Grey Zones</b>	<i>Optimality Criteria</i>	<i>Optimality Criteria</i>	<i>Nonlinear projection</i>
<b>Local Minima</b>	<i>Global Optimum Convergence</i>	<i>Global Optimum Convergence</i>	<i>Continuation</i>

**Table 1** - Top Suite characteristics

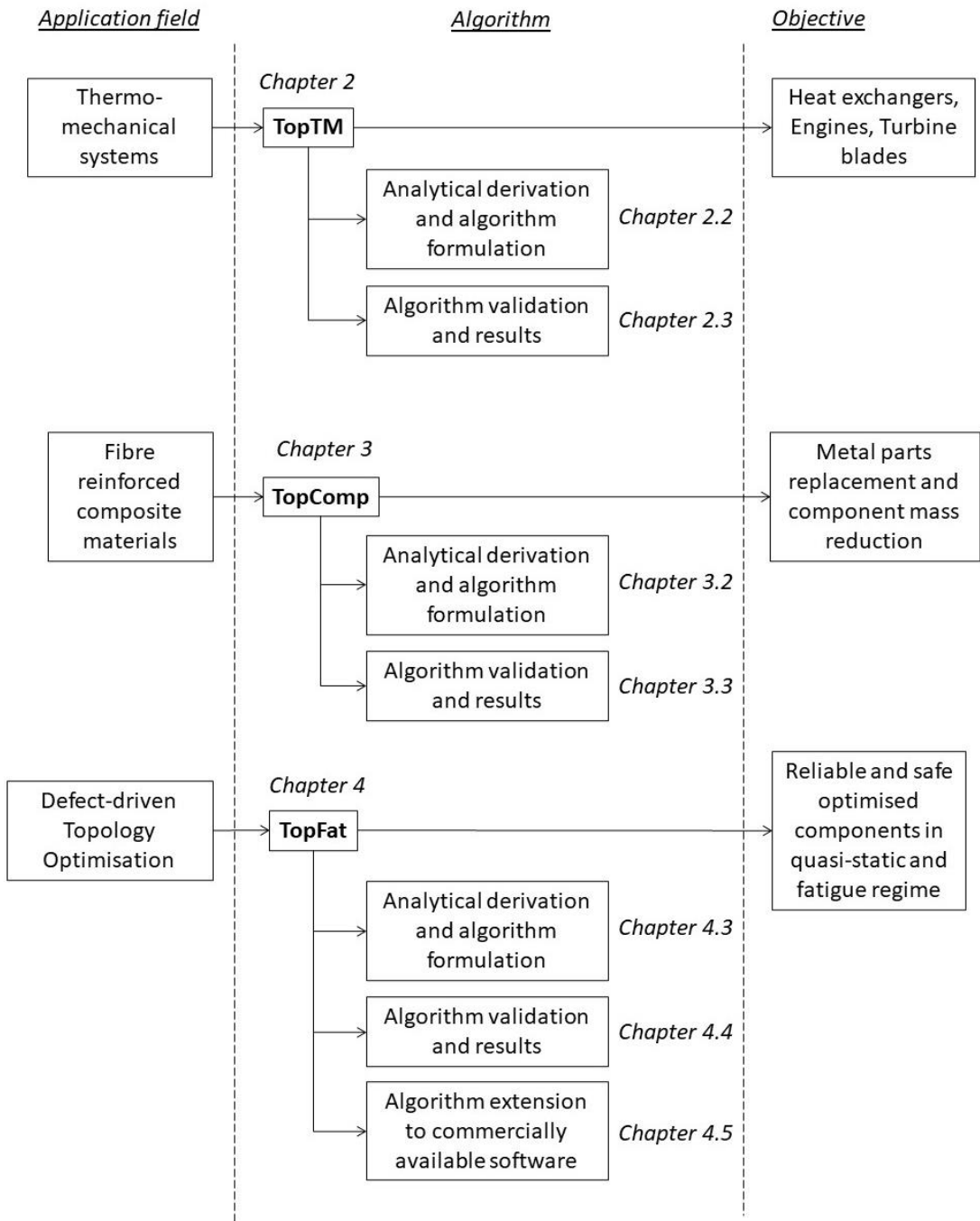
Overall, the *Top* Suite is thought to be a useful tool for industries to foster the AM applications. All the codes are easy to be implanted or transferred to commercially available software. Below, an illustrative scheme regarding the *Top* Suite problem-solution fit is presented. All the algorithms solve a specific problem or opportunity offered by AM technologies in the related application field. The objective is to maximise the component performances.

The first category of problems is related to the thermo-mechanical systems. In particular, the main issue is the optimisation of systems that undergo coupled loads, both mechanical and thermal. In chapter 2, the *TopTM* algorithm is presented, in chapter 2.2 it is analytically obtained and in chapter 2.3 it is validated together with optimisation results. *TopTM* is suitable for the optimisation of components such as heat exchangers, engines, turbine blades and so on where the thermal and mechanical loads cannot be untied.

The second category of problems is related to fibre reinforced composite materials. In particular, the main issue is the optimisation of materials, especially polymers, reinforced by means of rigid fibres. AM processes indeed are able to tune the fibre deposition within the polymer matrix to obtain improved properties. The way these fibres fill in and the overall topology of the component is obtained thanks to the *TopComp* algorithm. In chapter 3, the *TopComp* algorithm is presented, in chapter 3.2 it is analytically obtained and in chapter 3.3 it is validated together with optimisation results. *TopComp* is aimed at obtaining top optimised fibre reinforced composites with mechanical properties comparable to metal, especially aluminium. Accordingly, this novel set of components would be able to replace metal parts and achieve huge mass reduction.

The third category of problems is related to the evaluation of the defect population within the topology optimisation process. Indeed, AM process suffers from a non-negligible defect population characterised by pores, cluster of pores and lack of fusion just to cite a few of them. These defects affect and lower remarkably the fatigue response of the part. Furthermore, classical fatigue models are not able to consider and model this defect population in the part life span evaluation. For this reason, *TopFat* uses the Murakami model to include the defects population within the topology optimisation process. In chapter 4, the *TopFat* algorithm is presented, in chapter 4.2 it is analytically obtained, in chapter 4.3 it is validated together with optimisation results and in chapter 4.4 it is extended to commercially available software. *TopFat* it is aimed at obtaining reliable final designs in both the quasi-static and fatigue regime.

Below, a detailed description of every *Top* code is reported to precisely highlighted the novelty and the characteristics.



# Chapter 2

## ***TopTM*: thermo-mechanical topology optimisation**

### **2.1 Thermo-mechanical topology optimisation background**

Topology Optimisation algorithms are usually employed to design components subjected to mechanical and structural loads. However, Topology Optimisation in the thermal field has been investigated in the literature as well and cover a vastity of industrial applications. Indeed, algorithms permitting to maximize conduction heat transfer have been proposed during the last years. Most of them are analysed and reviewed in [66]. Furthermore, experimental investigations of this type of Topology Optimisation have been carried out as well [67]. It is worth to note that the optimisation strategies are the same employed for the enhancement of the mechanical stiffness. As already described before, the SIMP strategy for the heat conduction Topology Optimisation [68] and the BESO method have been employed [69].

Nevertheless, some components in real applications can be subjected to combined structural and thermal loads, like as turbine blades, engines, or heat exchangers. Consequently, the development of optimisation algorithms allowing to design structures subjected to coupled thermal and structural loads is of utmost interest among researchers and industry.

These algorithms can be divided in two main categories. The first one consists of a classical stiffness maximisation considering the effect of the induced thermal stress and strains. In other words, the structural Topology Optimisation must consider the presence of a temperature field which modifies the strain distribution. The most important and last achievements in this direction are described hereafter. [70] presented a temperature-constrained Topology Optimisation method for thermo-mechanical coupled problems. [71] proposed a multiple material Topology Optimisation under the conditions of steady-state temperature and mechanical loading. [72] presented a method for Topology Optimisation of

structures with combined mechanical and thermoelastic (temperature) loads subjected to stress constraints. [73] proposed a mean compliance and elastic strain energy minimization for thermoelastic problems. Lastly, [74] presented a guide-weight method to solve the Topology Optimisation problems of thermoelastic structures.

The second category of algorithms for thermo-mechanical optimisation problems consists of methods aimed to find the final topology which maximise/minimize the heat exchange and maximise structural stiffness. Therefore, the objective function is no more purely mechanical but must also consider thermal objective, such as guarantee a defined heat exchange. Most importantly, [75] defined a Topology Optimisation method that considers both thermal and mechanical objectives. [76] proposed a Topology Optimisation algorithm with constraints on structural strength and thermal conductivity. [39] present a method for the Topology Optimisation of the microstructure of a composite material with the aim of finding the material with the most effective values of the bulk modulus of elasticity and thermal conductivity. [77] developed a hybrid cellular automaton model combined with finite element method for structural Topology Optimisation with mechanical and heat constraints.

According to the literature, thermo-mechanical Topology Optimisation has been widely investigated and there are many publications in this area. However, further improvements in this field can be achieved. First, the majority of the algorithms is based on SIMP or RAMP (Rational Approximation Material Properties) approaches which require the penalisation factor. This factor is often linked with convergence problems such as local minima as already described in the previous paragraphs. Considering evolutionary methods, such as BESO, a lack of an analytical generality and convergence criteria has been observed [29]. Furthermore, if the objective function and the constraints are fairly complex, the formulated optimisation problem often needs advanced programming methods such as MMA (Method of Moving Asymptotes) [25] and sensitivity analysis to be solved.

The presented *TopTM* algorithm consists of an innovative methodology for the maximization of the thermal exchange and the mechanical stiffness of a structure under thermo-mechanical loads. Differently from other classical *density-based* approach, penalisation factors are not required and there is no need of numerical corrections. In addition, a simple formulation for the optimality criteria is analytically derived and physically verified. The proposed objective function parametrisation allows to analytically solve the optimisation problem, i.e. numerical programming methods and sensitivities analysis are not required. The stresses induced by the thermal loads are considered in the optimisation and the thermal exchange and the structural stiffness are concurrently optimized, thus permitting to assess a more effective material distribution.

In the following paragraph, the analytical formulation of the problem is reported and solved and the criteria for the global optimum are defined. Thereafter, *TopTM* is validated with several benchmark and applicative examples. Finally, a real component employed for aerospace applications is

thermo-mechanically optimised, proving the applicability and effectiveness of *TopTM*.

## 2.2 *TopTM* solution

In the following paragraphs the analytical formulation of the proposed methodology is firstly reported. In particular, the optimality criterium for a system subjected to thermo-mechanical loads is defined. Then, the flowchart of the *TopTM* is reported and described. It is worth note to highlight that **bold** letters stand for vector or matrix quantities.

### 2.2.1 Optimality criterium derivation

The current topology optimization formulation provides a method allowing to assess the best material exploitation for a component subjected to structural and thermal loads. In particular, the heat exchange and the mechanical stiffness are maximized at the same time. In order to achieve this goal, the expression of the potential energy of the system has to be obtained and then the structural optimisation problem consists in its minimization under selected constraints. In other words, through the minimization of the potential energy, the component deformation is minimized while the stiffness is maximized.

The starting point of the proposed optimization method is the equilibrium equation for a system subjected to thermo-mechanical loads, shown schematically in Figure 29. Let consider as domain of existence a portion of a system  $\Omega$  limited in the space ( $\Omega \subseteq \mathbb{R}^3$ ) containing the material  $M$ , with regular frontier  $\Gamma$ . The spatial coordinates are called  $x, y, z$  or, in vector notation,  $\mathbf{x}$ . The displacement field of  $M$  is  $\mathbf{u} = \mathbf{u}(\mathbf{x})$  and the temperature field is  $\theta = \theta(\mathbf{x})$ . The material  $M$  is assumed to be isotropic with a linear elastic behaviour (i.e., it follows the Hooke's law [78]) and it is characterized by Young's modulus  $E$ , Poisson's ratio  $\nu$ , thermal expansion coefficient  $\alpha$ , thermal conductivity  $k$  and density  $\rho$ . In addition, all the applied boundary conditions satisfy the border completeness [79], according to Eq.13. In other words, each portion of the frontier  $\Gamma$  is defined by a boundary condition, both thermal and structural:

$$\begin{aligned} \Gamma_N^\theta \cup \Gamma_D^\theta &= \Gamma & \text{and} & & \Gamma_N^\theta \cap \Gamma_D^\theta &= \emptyset \\ \Gamma_N^u \cup \Gamma_D^u &= \Gamma & \text{and} & & \Gamma_N^u \cap \Gamma_D^u &= \emptyset \end{aligned} \quad (13)$$

where  $\Gamma_N^\theta$  is the Neumann boundary condition of the thermal field,  $\Gamma_D^\theta$  is the Dirichlet boundary condition of the thermal field, Figure 29,  $\Gamma_N^u$  is the Neumann boundary condition of the structural field and  $\Gamma_D^u$  is the Dirichlet boundary condition of the structural field (Figure 29). The symbol  $\emptyset$  stands for empty set.



**Figure 29** – Thermostructural system

The overall equilibrium of an infinitesimal portion  $d\Omega$  of the system  $\Omega$  is described by Eq.14, as reported in [79].

$$\begin{bmatrix} \nabla \boldsymbol{\sigma} & \beta \nabla \\ \mathbf{0}^T & k \nabla^2 \end{bmatrix} \begin{pmatrix} \mathbf{u} \\ \theta \end{pmatrix} + \begin{pmatrix} \mathbf{F} \\ H \end{pmatrix} = \mathbf{0} \quad (14)$$

in which  $\nabla$  is the operator of derivation with respect to the three space dimensions,  $\nabla^2$  is the Laplacian operator,  $\beta$  is the thermo-mechanical coupling term (i.e., equal to the product of the Young's modulus  $E$  and the thermal expansion coefficient  $\alpha$ ,  $\beta = E\alpha$ ),  $k$  is the thermal conduction coefficient,  $\boldsymbol{\sigma}$  is the stress tensor,  $\mathbf{F}$  is the vector of internal forces,  $H$  is the internal generated heat and  $\mathbf{0}$  is the null vector. Applying the variational methodology as done in [80], by integrating Eq.14 in the domain  $\Omega$ , it is possible to obtain the weak expression of the potential energy of the system. In particular, the solution of a thermo-mechanical topology optimization problem can be achieved by implementing the weak expression of the potential energy by excluding differential terms. The resulting potential energy equation is a scalar quantity and corresponds to the *thermo-mechanical potential energy*,  $\Pi(\mathbf{u}, \theta)$  of the system shown in Eq.15:

$$\Pi(\mathbf{u}, \theta) = -\frac{1}{2} \left( \int_{\Omega} \mathbf{e}^T(\mathbf{u}) \mathbf{A} \mathbf{e}(\mathbf{u}) dx + \xi \int_{\Omega} k \nabla^2 \theta dx + \int_{\Omega} \beta \nabla^T \theta \mathbf{u} dx \right) \quad (15)$$

where the term  $\mathbf{e}$  is the vector of the structural deformations or strains,  $\mathbf{A}$  is the constitutive matrix. The term  $\xi$  represents the linker between thermal and mechanical energy (measure unit [time/temperature]). It allows to consider in the same potential equation both the contributes without violating physical continuity.  $\xi$  must be chosen in order to balance the structural and the thermal contributes, assigning therefore the same importance to each contribution. It has to be evaluated according to the design constraints before the optimization process as will be detailed after.

Eq.15 is the objective function that must be minimised in order to find the optimal topology. A system that has a smaller coupled potential energy is subjected to smaller variations of its state, i.e. temperature and displacement. In order to define the optimisation problem, it is necessary to define an artificial variable, called  $\eta$ . This variable represents the material effectiveness in each point of the domain  $\Omega$ . In other words,  $\eta$  stands for the presence and consistency of the material in the domain, point by point. This variable is design variable of the system and it is the base for the *density-based* method here proposed. The variable

$\eta$  must be limited both by an upper boundary  $\eta_{max}$  and by a lower boundary  $\eta_{min}$  as reported in Eq.16 [58].

$$\begin{aligned} \eta &= \eta(\mathbf{x}) \\ 0 &< \eta_{min} < \eta < \eta_{max} < \infty \end{aligned} \quad (16)$$

For  $\eta = \eta_{max}$  the material is considered full, so the material properties are the same of the base material  $M$ , for  $\eta = \eta_{min}$  the material considered void, and its properties are close to be null. The topology optimisation problem, reported in Eq.17, consists in finding the distribution of  $\eta(\mathbf{x})$  that minimises the coupled potential energy  $\Pi(\mathbf{u}, \theta)$  for a volume  $\bar{V}$ .  $\bar{V}$  is a portion of the initial volume and the second equation in Eq.17 represents the volume optimisation constraint.

$$\left\{ \begin{aligned} \max_{\eta} \Pi(\eta, \mathbf{u}, \theta) &= \min_{\eta} \frac{1}{2} \left( \int_{\Omega} \mathbf{e}^T(\mathbf{u}) \mathbf{A} \mathbf{e}(\mathbf{u}) \eta \, dx + \xi \int_{\Omega} k \nabla^2 \theta \, \eta \, dx + \int_{\Omega} \beta \nabla^T \theta \, \mathbf{u} \, \eta \, dx \right) \quad s. t. \\ \int_{\Omega} \eta \, d\Omega &\leq \bar{V} \\ 0 &< \eta_{min} < \eta < \eta_{max} < \infty \end{aligned} \right. \quad (17)$$

The optimization problem in Eq.17 can be solved by iteratively applying Kuhn-Tucker optimality criteria (Lagrange multiplier method, [58]). In particular, the Lagrangian function  $L(\eta, \lambda, t)$ , has to be defined and all its derivatives must be equal to zero (Eq.18) in order to identify a stationary point of the function:

$$L(\eta, \lambda, t) = \frac{1}{2} \left( \int_{\Omega} \mathbf{e}^T(\mathbf{u}) \mathbf{A} \mathbf{e}(\mathbf{u}) \eta \, dx + \xi \int_{\Omega} k \nabla^2 \theta \, \eta \, dx + \int_{\Omega} \beta \nabla^T \theta \, \mathbf{u} \, \eta \, dx \right) - \lambda \left( \int_{\Omega} \eta \, d\Omega - \bar{V} + t^2 \right) \quad (18)$$

If the problem is discretized by using  $N_{elem}$  elements, e.g. using the Finite Element Method (FEM), Eq.18 is defined on each  $e$  portion of the domain called  $\Omega_e$  and the effectiveness variable  $\eta$  must be discretised too as reported in Eq.19.

$$\left\{ \begin{aligned} \eta(\mathbf{x}) &= \eta_e \quad \forall \mathbf{x} \in \Omega_e \quad e = 1, \dots, N_{elem} \\ 0 &< \eta_{min} < \eta_e < \eta_{max} < \infty \end{aligned} \right. \quad (19)$$

Following the same passages shown in Eqs.15-19, the value of the *Lagrange multiplier* for each element can be evaluated as reported in Eq.20:

$$\lambda_e = \frac{\frac{1}{2} (\mathbf{e}_e^T(\mathbf{u}) \mathbf{A} \mathbf{e}_e(\mathbf{u}) + \xi \nabla_e^T \theta k(\mathbf{x}) \nabla_e \theta + \beta \nabla_e^T \theta \, \mathbf{u}_e) \Omega_e}{\Omega_e} = \epsilon_e = \lambda = \epsilon \quad e = 1, \dots, N_{elem} \quad (20)$$

The Lagrange multiplier for each element corresponds therefore to the thermo-mechanical energy density for that element. According to [58], the Lagrange multiplier must be the same for the entire structure, thus every  $\lambda_e$  needs to be equal to the value found by considering a continuous solution (i.e.,  $\lambda = \lambda_e$ , with  $\lambda$  defined according to Eq.20). Therefore, the thermo-mechanical energy density in each element has to be uniformly distributed within the structure in the

optimized topology (optimality criterium). The assessment of the material distribution ensuring a uniform thermo-mechanical energy density is therefore the objective of the optimization algorithm. For more, the optimisation problem as formulated is convex since no material interpolation is employed [57]. Therefore, *TopTM* guarantees that a global minimum for the thermo-mechanical topology optimisation problem is achieved.

### 2.2.2 Iterative solution implementation

The flowchart in Figure 30 shows the iterative optimisation process developed to obtain the optimized topology, i.e. a uniformly distributed thermo-mechanical energy density.

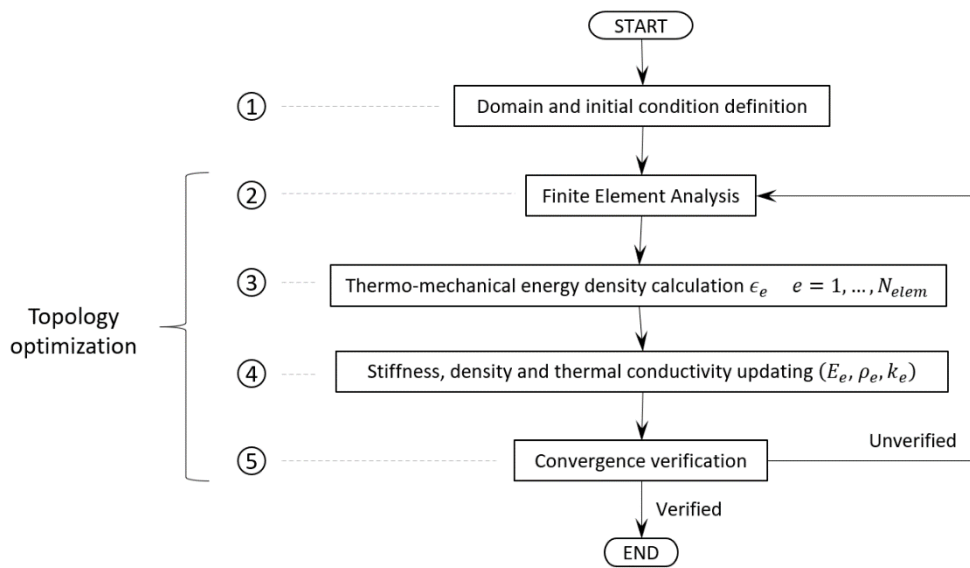


**Figure 30** - Flow chart of thermo-mechanical topology optimisation.

The preliminary phase is the definition of the Finite Element Model and the initial conditions, which corresponds to phase number 1 in Figure 30. Then phase number 2 consists of a FE simulation on the initial model. This simulation allows to evaluate the distribution of the thermal gradient and mechanical strain. These quantities are used to calculate the thermo-mechanical energy density  $\epsilon_e$  for each element as shown in Eq.20 and it represents step number 3 in Figure 30. The 4th phase corresponds to the update of the local properties of material, i.e. Young's modulus, density and thermal conductivity. This procedure is the main core of the optimisation process and it allows to obtain the final material distribution. It is possible to achieve a final topology that ensures the uniform distribution of the thermo-mechanical energy density by modifying the local properties of the material according to a precise updating law. This updating law can be achieved considering the effectiveness of the material together with Eq.20 [58]. Eq.21 expresses the relationship between the local effectiveness and the thermo-mechanical energy density. It is worth to note that the updating process is iterative, this is because the effectiveness variable is limited, and the modification of this variable causes the variation of the thermal gradient and mechanical strain

distribution [58,80]. Therefore, in Eq.20 index  $j$  refers to a single iteration while  $p$  is its total number.

$$\eta_e^{j+1} = \frac{\epsilon_e^j}{\epsilon^j} \eta_e^j \quad e = 1, \dots, N_{elem} \quad j = 1, \dots, p \quad (21)$$

In the previous equation, considering element  $e$  and iterations  $j$  and  $j + 1$ ,  $\eta_e^{j+1}$  is the updated effectiveness,  $\eta_e^j$  is the current one, while  $\epsilon_e^j$  represents the thermo-mechanical energy density for the element and  $\epsilon^j$  stands for the average thermo-mechanical energy density in the global structure.

In order to link the artificial material effectiveness variable to the real parameters of the material,  $\eta_e$  is considered multiplying the Young's modulus  $E_e$ , the density  $\rho_e$  and the thermal conductivity  $k_e$  as shown in Eq.22. The material properties and the material effectiveness  $\eta$  with the subscript  $e$  refer to a single element considered for the discretization of the domain and vary during each iteration, whereas the material properties of the base material, indicated with the subscript 0 in Eq.22, remain constant (i.e.,  $E_0$ ,  $k_0$  and  $\rho_0$  stand respectively for the Young's modulus, the density, and the thermal conductivity of the material at the beginning of the process):

$$\begin{cases} E_e^{j+1} = \frac{\epsilon_e^j}{\epsilon^j} E_e^j \\ \rho_e^{j+1} = \frac{\epsilon_e^j}{\epsilon^j} \rho_e^j \\ k_e^{j+1} = \frac{\epsilon_e^j}{\epsilon^j} k_e^j \end{cases} \quad e = 1, \dots, N_{elem} \quad j = 1, \dots, p \quad (22)$$

During the iterative procedure, the elements of the material that participate scarcely to the load sharing are characterized by a low energy density, hence their effectiveness is reduced, i.e. the density, the Young's modulus and the conductivity of the element are lowered and vice versa. In order to define when the final topology has been achieved, a convergence criterion of the iterative process is needed. This represents phase 5 in Fig. (2). The convergence occurs when the change in the variables is less than the imposed convergence parameter, usually less than 1 percent. At this condition corresponds a discrete distribution of material, i.e. full or void material without intermediate values. This criterion is the same used by O. Sigmund in [57]. It is possible to verify the volume constraint imposing a certain value to the Lagrange multiplier in Eq.20 using a bi-sectioning algorithm.

Another convergence criterion is proposed in [58,80]. In particular, the volume constraint can be considered in term of reference energy. In this case, an objective thermo-mechanical energy density in the structure  $\epsilon_{ref}$  is defined before the optimization process. For example,  $\epsilon_{ref}$  can be defined by considering the maximum allowable stress within the structure and the maximum allowable

thermal gradient. The convergence is reached if the percentage difference between  $\epsilon_{ref}$  and the average thermo-mechanical energy density  $\bar{\epsilon}$  evaluated in the structure is lower than 0.1% for three consecutive iterations. This criterion considers concurrently the changing of the variables and the energy constraint.

Depending, on the application and on the final objective of the optimization process, these two criteria can be alternatively considered.

### 2.2.3 Benchmarking validation

In the following paragraph, two comparative benchmarks for thermal and structural topology optimisation are provided. The main purpose is to validate the *TopTM* on classical literature benchmarks. Considering the thermal or mechanical energy density null, the algorithm works as purely structural or thermal topology optimization respectively. Therefore it is possible to verify the algorithm effectiveness on well-known existing examples.

In Figure 31 the thermal model of the heat condition topology optimisation problem is presented. It is a square domain with a portion of the left side at a fixed temperature. In the whole domain a heat generation rate is imposed. This example has been taken from [11] at page 271 where all the details on the numerical implementation, boundary conditions and the employed material are reported.

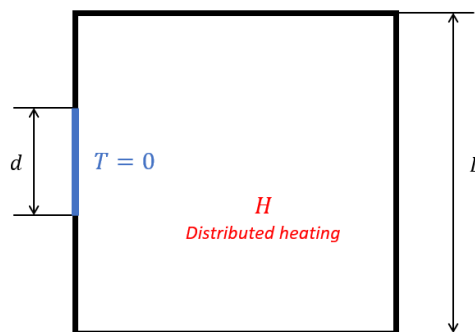


**Figure 31** - Thermal boundary conditions and geometry settings

The result of the thermal Topology Optimisation is reported in Figure 32. On the right side the result obtained with the *TopTM* (red-blue topology) is shown whereas on the left the benchmark solution by is reported (black-withe topology). As it can be noticed, the two results are almost identical. It is worth to note that with *TopTM* no intermediate densities have been found in the final structure. The final topology obtained with *TopTM* is defined by the red zones in the Figure.

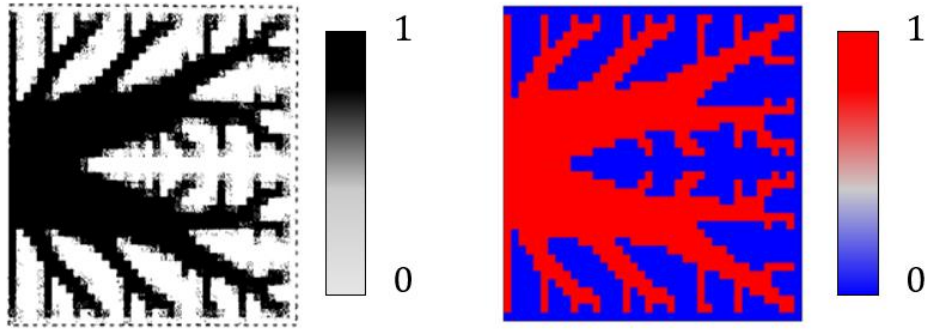


**Figure 32** - Heat conduction topology optimisation benchmark

In Figure 33 the structural model of minimum compliance topology optimisation is presented. It is a rectangular domain with the left side fully constrained and a nodal downwards vertical force on the right lower vertex. This example has been taken from [55] page 123 Fig. (2).

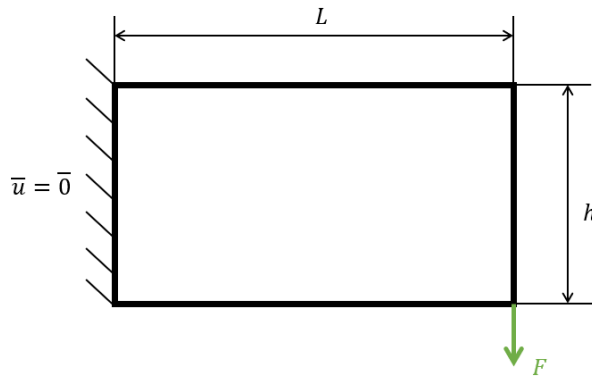


**Figure 33** - Structural boundary conditions and geometry settings

The result of the structural Topology Optimisation is reported in Figure 34. On the right side the result obtained with the *TopTM* (red-blue topology) is shown whereas on the left the benchmark solution by is reported (black-withe topology). Similarly to the pure thermal benchmark, the two results are almost identical, and no intermediate densities have been found in the final structure. The final topology obtained with *TopTM* is defined by the red zones in the Figure.

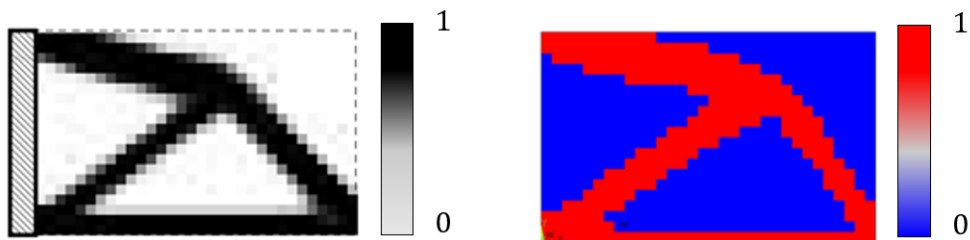


**Figure 34** – Structural topology optimisation benchmark

## 2.3 *TopTM* results

In this paragraph, the *TopTM* algorithm is validated. Firstly, *TopTM* is verified considering two bidimensional literature test cases. Then, a three-dimensional component employed for aerospace applications is optimised. Overall, *TopTM* is tested on literature benchmarks, teste cases and industrial cases, demonstrating its applicability.

For the *TopTM* implementation, the commercial software Ansys has been used. A routine has been written in the Ansys APDL software for iteratively assessing the stress and the thermal gradients for each element and thereafter updating the material properties until the convergence criterion is met, according to flowchart in Figure 30.

The 1<sup>st</sup> phase is implemented coding the geometry settings and boundary conditions of the initial domain in APDL code. The 2<sup>nd</sup> phase, consisting of the finite element analyses, is processed by the solution command. Automatically, all the results information is achieved, i.e. stresses, strains, displacements, energies and so on. At this point, it is possible to evaluate the thermo-mechanical energy density for each element through Eq.15, namely the 3<sup>rd</sup> phase. Given this coupled energy density for each element, it is possible to update the material parameters of each element following Eq.22. In particular, since the energy reference criterion is employed, the term  $\epsilon^j$  is substituted with  $\epsilon_{ref}$ . Therefore, the elements which have an energy density lager than the reference will be rewarded. On the other hand, if the energy density is smaller than the reference value, the element is penalized. Therefore, only the elements which are most meaningful for the load bearing purpose are selected in the final topology. After that, the updated material parameters are cut according to the minimum and maximum value imposed in Eq.21.

This updating procedure refers to the 4<sup>th</sup> phase. At this point, the convergence criterion can be checked as stated in the 5<sup>th</sup> phase. Since in the following cases a reference thermo-mechanical energy density is imposed, the convergence can be considered reached when the average thermo-mechanical energy density matches the reference one for three consecutive iterations. At this condition corresponds a discrete distribution of material, i.e. full or void material without intermediate values of the material properties. This means also that each element shares in average the same  $\epsilon_{ref}$  and the updating law in Eq.22 is no more effective. All the described processes can be easily coded in less than 150 code lines in APDL.

### 2.3.1 Test cases

A beam with length  $L = 200$  mm, height  $h = 100$  m, with mechanical and thermal loads applied concurrently was considered for the validation of *TopTM*. In every bidimensional case considered, the plane stress assumption has been employed. In the first case, shown in Figure 35a, the beam is simply supported with a vertical force  $F = 1000$  N applied in the middle of the lower edge. In

addition, a portion of each edge with length  $d = 10$  mm, symmetric with respect to the beam axes presents a fixed constant temperature. On the horizontal edge portions (shown in red in Figure 35a) the imposed temperature,  $T_1$ , is equal to  $100^\circ\text{C}$ , whereas it is equal to  $0^\circ\text{C}$  on the vertical edge portions ( $T_2$ , shown in blue in Figure 35a). In the second case, shown in Figure 35b, the beam is fixed at the left edge (cantilever beam condition), with a vertical force  $F$  applied at the right end. Thermal loads are represented by the constant temperature  $T_1$  along the entire left edge and an outgoing heat flow  $Q = 1\text{W}$  (according to Figure 35b) applied on a central portion  $d$  of the right vertical edge. A common steel was considered for the constitutive model of the material and its properties are reported in Table 2. Plane square quad 8 nodes elements, with the side length of 1 mm, were employed for the analysis. A detailed description of element PLANE 223 definition is provided by the ANSYS guide manual.

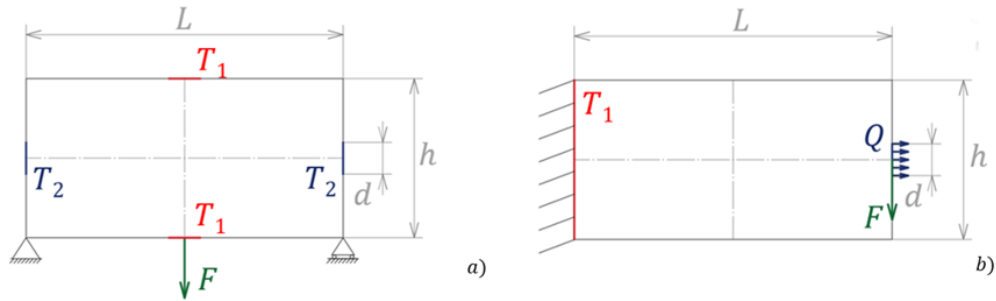


**Figure 35** - Validation of the *TopTM* on a 2D domain

Material	E [GPa]	$\nu$	$\rho$ [kg/m <sup>3</sup> ]	k [W/mK]	$\alpha$ [1/K]
Steel	210	0.3	7800	50	12e-6

**Table 2** - Properties of the steel for the benchmark validation

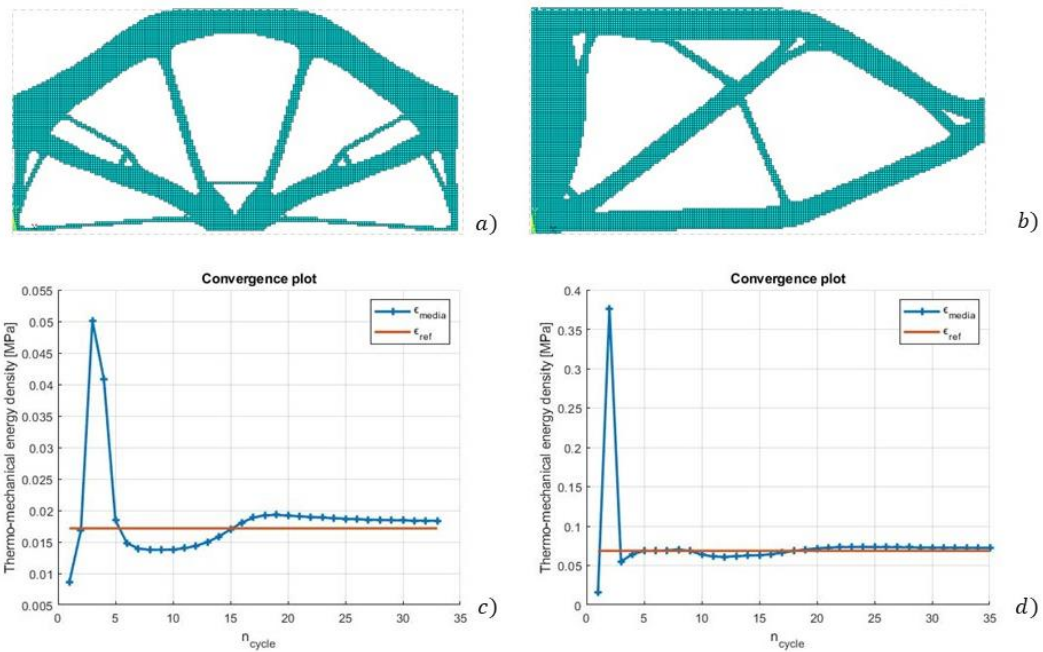
The convergence criterion was thereafter defined. In particular, a reference thermo-mechanical energy density  $\epsilon_{ref}$  (convergence criterion) evaluated as a balanced sum between the reference strain energy density  $\epsilon_{ref}^\sigma$  and the reference thermal energy density  $\epsilon_{ref}^\theta$  was considered.

$$\epsilon_{ref} = \epsilon_{ref}^\sigma + \xi \epsilon_{ref}^\theta \quad (23)$$

This separated reference energy densities  $\epsilon_{ref}^\sigma$  and  $\epsilon_{ref}^\theta$  can be calculated according to [58]. In particular,  $\epsilon_{ref}^\sigma$  can be computed as function of a reference stress  $\sigma_{ref}$  (for example the maximum allowable stress within the component with the formula  $\epsilon_{ref}^\sigma = \sigma_{ref}^2/2E$ ), whereas  $\epsilon_{ref}^\theta$  can be calculated as a function of a reference thermal gradient  $\nabla\theta_{ref}$  (i.e., in order to limit the maximum temperature within the component with the formula  $\epsilon_{ref}^\theta = k\nabla\theta_{ref}^2/2$ ). In particular, for the simply supported beam,  $\sigma_{ref}$  was chosen equal to  $60\text{MPa}$  and  $\nabla\theta_{ref} =$

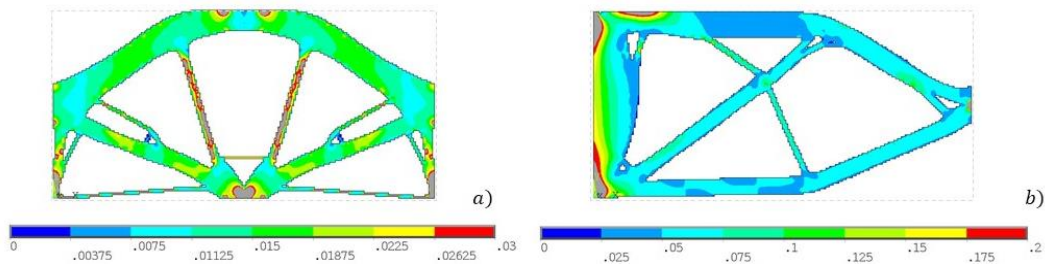
0.825 K/mm, whereas for the cantilever beam  $\sigma_{ref} = 120 \text{ MPa}$  and  $\nabla\theta_{ref} = 1.1 \text{ K/mm}$ . These values have been chosen as samples for reference thermal gradient and mechanical stress. As a matter of fact, any value could be employed to run the optimisations. The only limit is to use values that can be reasonable for the employed materials, e.g. reference stress inferior to the material yield strength. Clearly, different values of these references would bring to different final topologies which would represent the optimal material distributions for that specific case. The linker term  $\xi$  can be evaluated with the formula  $\xi = \sigma_{ref}^2 / Ek\nabla\theta_{ref}^2$  which guarantees the same weight to both thermal and structural reference contribution. As already stated, this term allows combining the mechanical and the thermal energy. A random value of this linker term may artificially increase the thermal contribute or vice versa. This term must be chosen to balance the two energy contributions. Hence, the reason why this term must be evaluated with this formula can be easily understood by analysing the possible scenarios during the optimisation. For an element characterized by only a structural task, i.e.  $\epsilon^\theta$  is null, the thermo-mechanical energy density of this element would be identical to the strain energy density. Vice versa, if the element had only a thermal task, i.e.  $\epsilon^\sigma$  is null, the thermo-mechanical energy density of this element would be equivalent to the thermal energy density. Hence, in both the extreme situations the numerical value of the coupled energy must be the same. If not, an element with the only thermal task would be considered differently with respect to another with only mechanical one. Therefore, in the end, the topology would be affected by a disparity in task contribute and the final material distribution would foster much more one of them. Choosing the linker term as  $\xi = \sigma_{ref}^2 / Ek\nabla\theta_{ref}^2$  this condition is avoided. This consideration is valid for all the intermediate conditions too. Both the thermal and mechanical tasks are kept equally into consideration. For different values of  $\xi$ , it would be as if the thermal or structural references would be set to different values from the prescribed ones. The reference thermo-mechanical energy densities  $\epsilon_{ref}$  for the two cases were finally respectively  $\epsilon_{ref}^1 = 1.17 \cdot 10^{-2} \text{ MPa}$  (for the simply supported beam) and  $\epsilon_{ref}^2 = 6.86 \cdot 10^{-2} \text{ MPa}$  for the cantilever beam.

The results of the optimization process are shown in Figure 36a for the simply supported beam with fixed temperatures and in Figure 36b for the cantilever beam with fixed temperature and outgoing heat flux. The thermo-mechanical energy density convergence plots for load case 1 and load case 2 are reported in Figure 36c and Figure 36d respectively. As it can be seen, the curves both converge fairly fast to the prescribed reference value. In both cases the convergence is reached with less than 40 iterations.



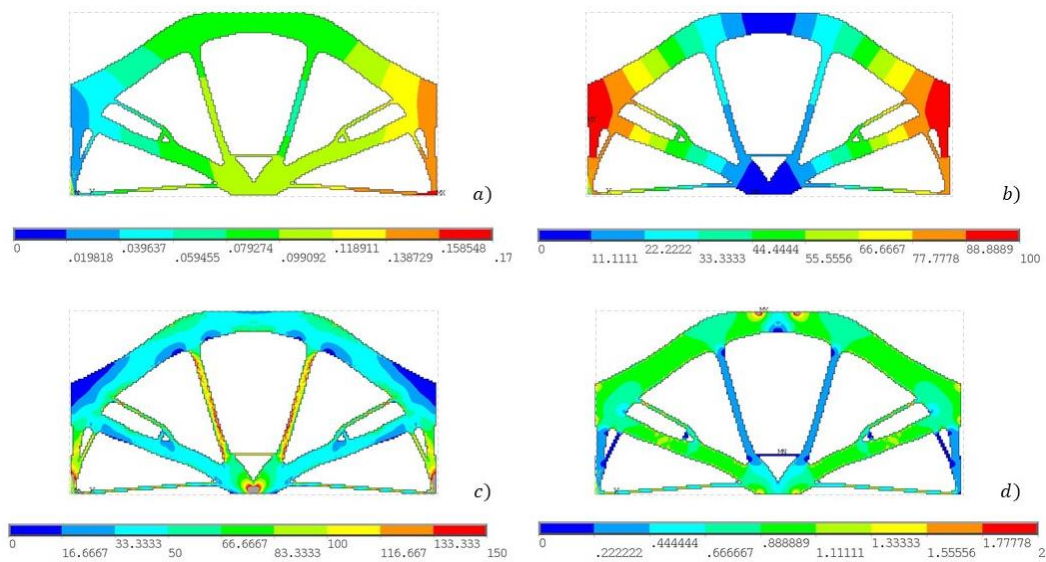
**Figure 36** - Final optimised topologies obtained with *TopTM*

Figure 37 shows the distribution of the thermo-mechanical energy density for the simply supported beam Figure 37a and for the cantilever beam Figure 37b. As it can be seen, this quantity has a range of variability almost uniform around the central reference value, according to Eq.19. This means that in the final topology all the elements bear equally the thermo-mechanical loads, with the material fully exploited and no inactive elements. It is worth to note that some grey zones are present in the Figure 37. However, these figures have been shown mainly to highlight the uniform distribution of the energies, stress, and gradients around the reference values. Indeed, since the loads are applied only on single nodes, nearby this points the stresses and the energies are extremely high. This is due to the fact that the process is numerical, and these extremely large values have not a real physical meaning. If the range from the maximum to the minimum value was considered, almost the whole structure would be characterized by the same colour. This would have avoided grey zones, but it would have not permitted to recognize the slighter variations of the plotted quantity within the domain, which is the real objectives of the figures.



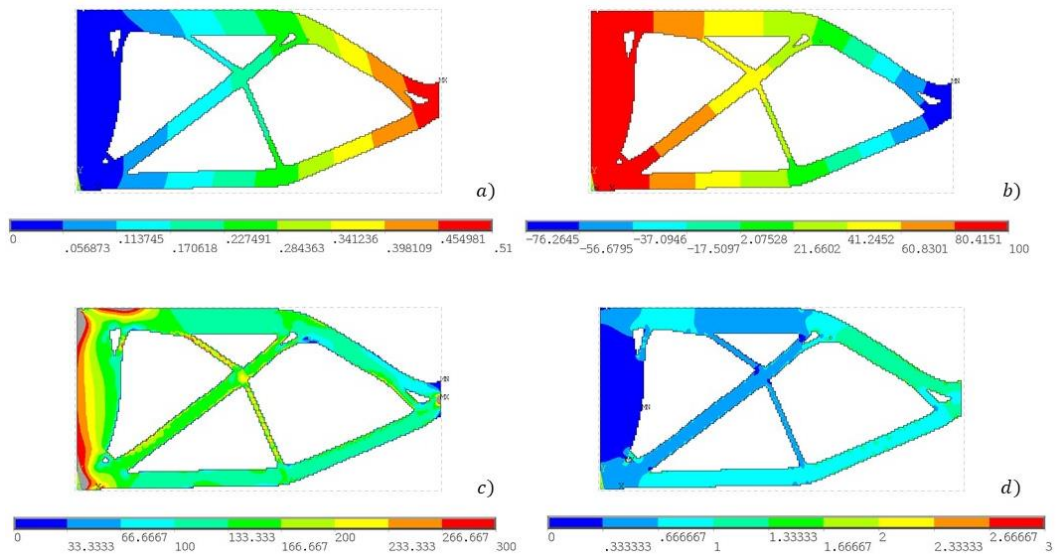
**Figure 37** - Thermostructural energy density distribution

Fig. Figure 38a and Figure 38b show respectively the global displacement and temperature field for the topology obtained in Figure 35a. As it can be seen, they are both limited and within a reasonable range. Moreover, Fig. Figure 38c and Figure 38d show the distribution of Von Mises ideal stress and thermal gradient for the same case, respectively. It is worth to note, that the prescribed references for the stress and thermal gradient were not the maximum allowable ones. Instead, they represent the values at which the average stress and thermal gradient must converge in order to achieve a uniform energy density distribution as done in [58]. From a practical point of view, since the zones with the stress exceeding the reference stress are limited, they can be eliminated when the component is “reconstructed” to generate the .cad or the .stl file with the appropriate fillets or with a subsequent shape optimization. Moreover, a larger safety factor can be also considered for reducing the areas with stress larger than the reference stresses.



**Figure 38** - Meaningful quantities in the final topologies LC1

The same considerations are valid for the cantilever beam. Fig. Figure 39a and Figure 39b show the global displacement and temperature field respectively and they are limited as for the previous case. In Fig. Figure 39c and Figure 39d the Von Mises ideal stress and the thermal gradient are shown. As before, it is possible to observe that both the quantities are almost uniform around the reference values within the final domain, thus proving that the material is fully exploited.



**Figure 39** - Meaningful quantities in the final topologies LC2

For the sake of comparison and to highlight the importance of concurrently considering the structural and the thermal loads during the optimization process, structural topology optimisations and thermal topology optimization were run separately on the presented load cases. It is important to note that the load cases remain the same reported in Figure 35. Hence, the boundary conditions are both structural and thermal. However, in the following cases the objective function neglects the structural objective or the thermal one. As it will be demonstrated, by considering only the structural or the thermal objective in components subjected to both types of loads, the resulting topology is characterized by a slightly larger effectiveness for the selected objective (thermal or structural depending on the objective of the optimization) but by a limited effectiveness for the neglected functionality. Therefore, this may lead to null heat conduction or overloaded structure. . Figure 40a shows the final topology obtained for the load case 1 by considering only the structural reference ( $\sigma_{ref} = 60$  MPa). Figure 40b and Figure 40c show the Von Mises stress and the thermal gradient, respectively. By considering Figure 40b, the stress distribution is uniform, with the same maximum value found through the coupled thermo-mechanical topology optimization, ensuring a very good exploitation of the material in terms of structural loads. Nevertheless, the thermal gradient, Figure 40c, results to be almost null over the domain, basically there is no thermal conduction. This happens because the algorithm focuses on the structural task and neglects the thermal one. Therefore, as in this case, only the portion of material important for the structural task are selected. Since they do not coincide with portion of material which guarantee the heat conduction, the thermal gradient results to be almost null over the domain. That's why considering a real application, the component would not be able to guarantee a sufficient heat flow.

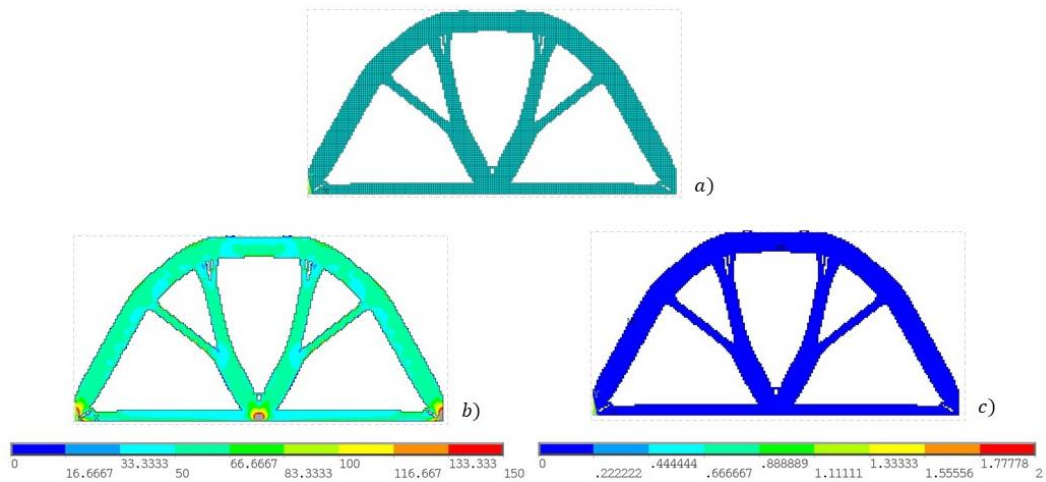


**Figure 40** - Meaningful quantities after structural topology optimisation of LC1

Figure 41a shows the thermal topology optimisation carried out on the load case 1, with  $\nabla\theta_{ref} = 0.825$  K/mm, whereas Figure 41b shows the Von Mises stress distribution and Figure 41c the thermal gradient sum. In this case the thermal gradient is uniform over the domain providing a very good thermal conduction. On the other hand, according to Figure 41c the Von Mises stress distribution significantly increases by considering only the thermal task, being almost four time greater than in the thermo-mechanical topology optimisation, Figure 38c). This could bring to possible static failure in the component or faster crack initiation and propagation.

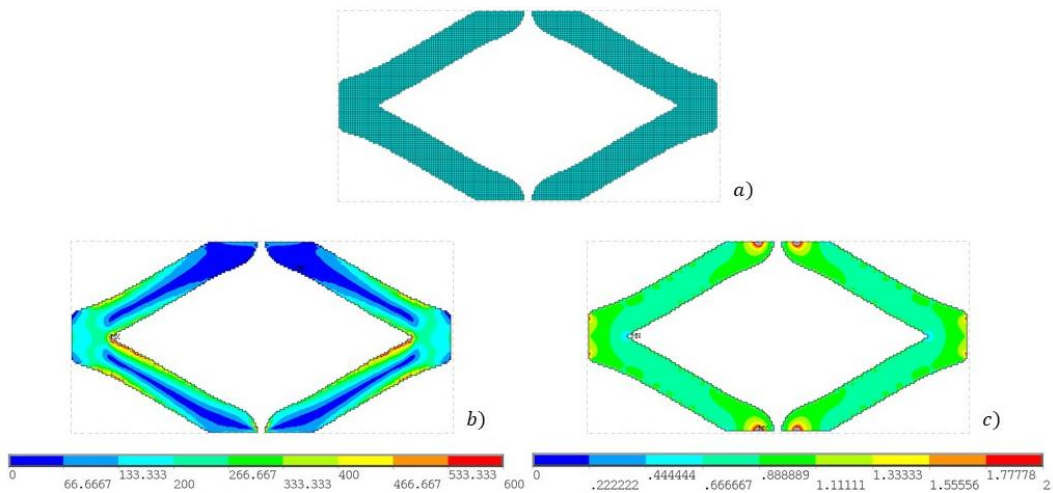


**Figure 41** - Meaningful quantities after thermal topology optimisation of LC1

Similarly, Figure 42a shows the final topology obtained for the load case 2 by considering only the structural reference ( $\sigma_{ref} = 120$  MPa), with Figure 42b and Figure 42c showing the Von Mises stress and the thermal gradient distributions, respectively. The same considerations made for the previous example on load case 1 are applicable. As a matter of fact, Von Mises stresses are well distributed and almost uniform within the domain. On the contrary, the thermal gradient

distribution presents remarkable differences in intensity depending on the material zones. Therefore, the heat flows inside the material in a very inefficient way. It is worth to note that the final topology is not identical to the minimum compliance topology optimisation problem for cantilever beam, well known in the literature. This is due to the temperature field inside the domain that modifies the strain distribution.

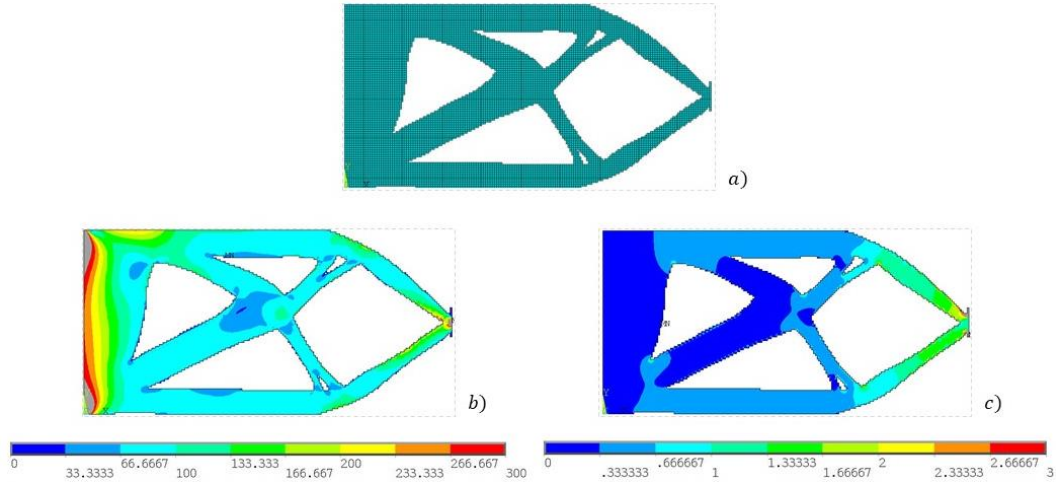


**Figure 42** - Meaningful quantities in the final topologies LC2

Figure 43a shows the thermal topology optimisation carried out on the load case 2, with  $\nabla\theta_{ref} = 1.1$  K/mm, whereas Figure 43b shows the Von Mises stress distribution and Figure 43c the thermal gradient sum. In this case the thermal gradient distribution is uniform over the domain providing a very good thermal conduction. In particular, Figure 43c shows a very good distribution of the gradient inside the domain. On the contrary, the structural task is not considered, and this can be detrimental for the structural integrity.

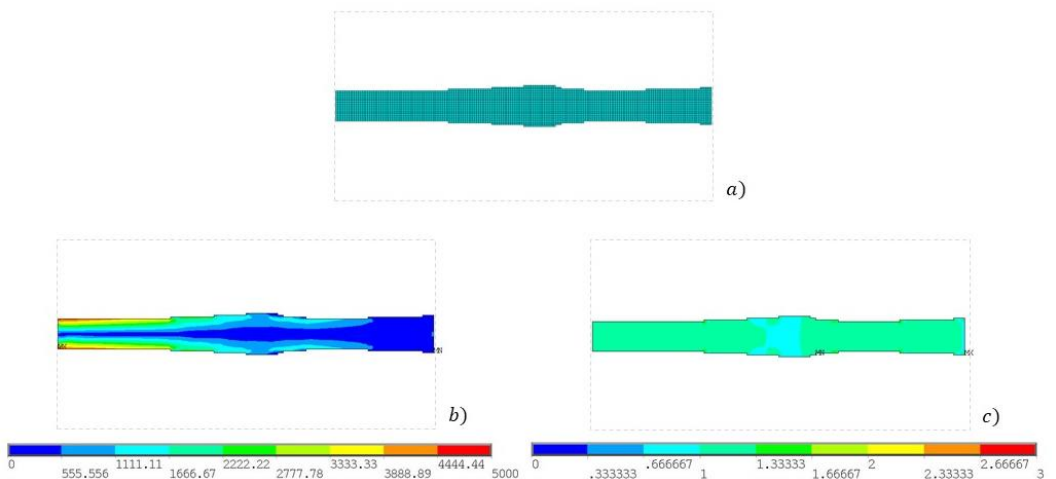


**Figure 43** - Meaningful quantities after thermal topology optimisation of LC2

The validation of *TopTM* in this Section clearly shows the importance of considering concurrently structural and thermal loads, if present, in the topology

optimization process. The thermo-mechanical topology optimisation provides the best topology for a component which undergoes coupled constraints and loads, permitting to obtain a uniform distribution of the thermo-mechanical energy density (Figure 37). Indeed, the coupled optimisation provides the best compromise between the structural and the thermal properties distribution and considers both the contributions, ensuring an optimal material distribution and the least material waste in order to concurrently achieve the best heat conduction and structural performance.

### 2.3.2 Industrial application

In this paragraph, *TopTM* is applied to a thermo-mechanical real application. In particular, the topology of a radiator for a loop heat pipe (LHP) is optimized. The applied loads and constraints are taken from the literature and data not available have been assumed, with the aim of proving that *TopTM* can be employed for real components allowing to maximise the performance of components subjected to thermo-mechanical loads.

The radiator of a Titanium Loop Heat Pipes (LHP) for Space Nuclear Power System similar to that analysed in [81] is considered. As shown in Figure 44, the radiator has a parallelepiped shape with a square base with  $L = 305$  mm and height  $h = 26.2$  mm. Two pipes enter symmetrically in the radiator and exit after three folds each from the same side. The fluid path (dash-dot black line) is also shown in Figure 44.

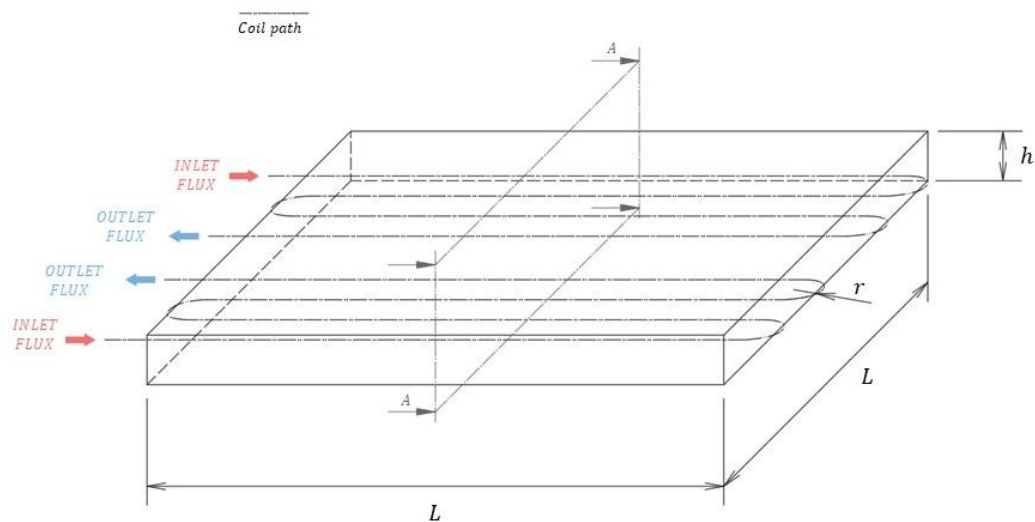


**Figure 44** - Radiator model and design domain with dimensions

Considering a cross section A as shown in Figure 45, it is possible to notice that for each section eight holes are present. They are symmetric with respect to both the axes of the rectangular section. The radius of the pipe is constant all over

the radiator and is equal to  $R = 9.55 \text{ mm}$ . Each fold has a radius of  $r = 15 \text{ mm}$ , causing a distance between the pipes inside the domain of  $d = 30 \text{ mm}$ . Given this geometry it is easy to notice that the cross section is constant along the radiator.

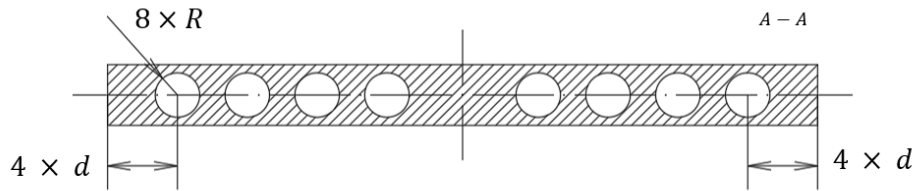


**Figure 45** - Cross section A of the radiator with dimensions.

The first phase of the optimization process involves the definition of the design and the non-design domain. The heat pipes are in almost all the applications inserted in a sandwich panel, with the core composed by a honeycomb structure [81]. For the redesign of the radiator with *TopTM*, the honeycomb structure is filled with a single isotropic material (design domain). On the contrary, the dimensions of the cross-section, of the radiator and heat pipes are left unaltered. A Titanium alloy Ti6Al4V, whose structural and thermal properties are reported in Table 3, was considered for the redesign and for the production of the component through an AM process [82]. Indeed, the complex shape obtained as a result of the optimization process, which can be hardly produced through traditional process, can be more easily produced through an AM manufacturing process.

Material	E [GPa]	$\nu$	$\rho$ [Kg/m <sup>3</sup> ]	k [W/mK]	$\alpha$ [1/K]
Ti6Al4V	113.8	0.342	4430	6.7	9e-6

**Table 3** - Ti6Al4V properties

It is worth to note that the component has a constant cross section, i.e. extrusion symmetry, and the cross section itself presents a double symmetry with respect to its axes. Therefore, for the optimization of the radiator only a quarter of the entire cross section, shown in Figure 46a, was considered and symmetric boundary conditions were applied. More in detail and by considering the structural loads, the radiator is supposed to carry the entire weight of Space Nuclear Power System which it is cooling [83]. Usually, the devices which are to be cooled are connected by pots and inserts inside the panels. However, in order to avoid many assumptions and computational complications, the load is uniformly distributed over the surface. In particular, the forces applied on the radiator are defined considering the entire weight of the Space Nuclear Power System multiplied by the average accelerations during the launch phase of the spacecraft (worst possible and conservative condition). The weight of a model of

the Power System for this type of radiator is about  $M = 56 \text{ kg}$ , as reported in [84]. Commonly the maximum acceleration during launch phase of spacecraft are 20 times the gravity acceleration,  $g$ , on Earth. Overall, the forces applied to the quarter of the cross section, Figure 46b, is the product of the Power System weight and the total acceleration in both directions split by four per unit of length, as reported by Eq.24:

$$F_x = F_y = \frac{20Mg}{4L} = 9 \frac{N}{mm} \quad (24)$$

In addition, internal pressure caused by the fluid inside the pipes is considered. The maximum internal pressure is  $p_{int} = 2.63 \text{ MPa}$ , as reported in [85]. For what concern the constraints, the radiator is supposed to be locked all along its lateral sides, as shown in Figure 46b.

From the thermal point of view Figure 46c, [85] provides the constant internal temperature of the fluid inside the pipes  $\theta = 413\text{K}$  and a total absorbed heat  $Q_{tot} = 590\text{W}$ . As for the structural field, the inlet heat applied on the portion of cross section is split by four and considered per unit of length as in Eq.25.

$$Q = \frac{Q_{tot}}{4L} = 0.48 \frac{W}{mm} \quad (25)$$

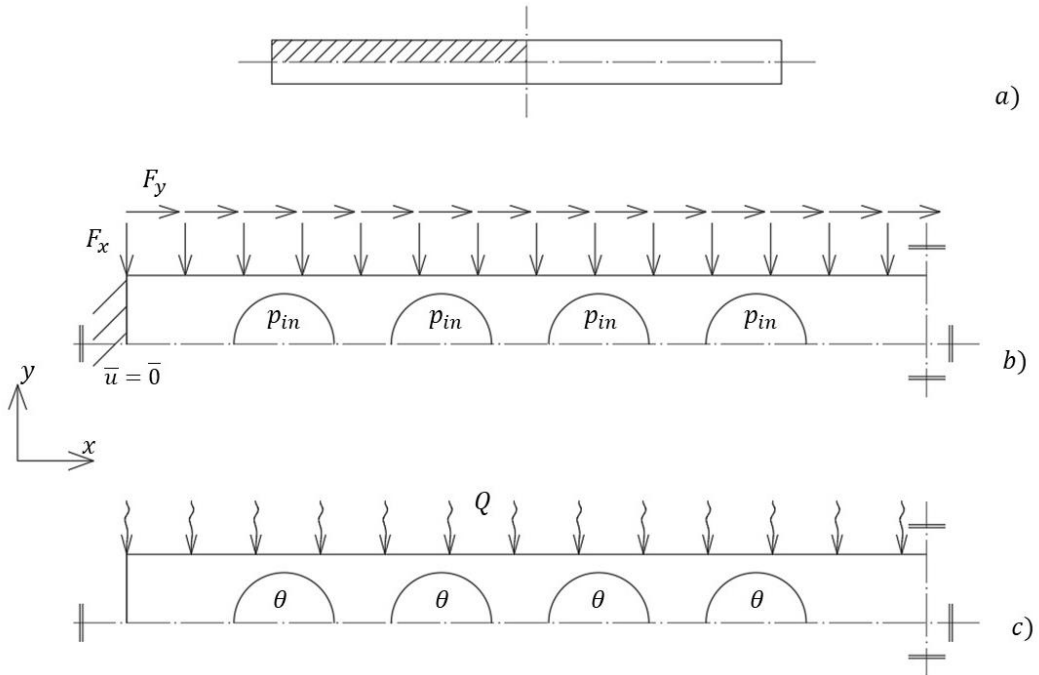


**Figure 46** – Loads and constraints applied to redesigned panel

Given the aforementioned boundary conditions, three different optimisations problems have been set up and the final topologies are shown in Figure 47. Figure 47a shows the result of a structural topology optimisation with a stress reference  $\sigma_{ref} = 130 \text{ MPa}$ . Figure 47b shows the result of the thermal topology optimisation with a thermal gradient reference  $\nabla\theta_{ref} = 2.5 \text{ K/mm}$ . Finally, Figure 47c shows the final material distribution after the thermo-mechanical

topology optimisation with a stress reference of  $\sigma_{ref} = 130 \text{ MPa}$ , a thermal gradient reference of  $\nabla\theta_{ref} = 2.5 \text{ K/mm}$  and a linker term evaluated as  $\xi = \sigma_{ref}^2 / Ek\nabla\theta_{ref}^2$ . These quantities provide a value of the reference thermo-mechanical energy density  $\epsilon_{ref} = 0.149 \text{ MPa}$  according to Eq.23. 14145 plane quad elements, 8 nodes each one, are employed for the analysis.



**Figure 47** - *TopTM* application on real component

In order to compare the three optimisation results reported in Figure 47 and to understand the effectiveness of the coupled method, further analyses have been carried out. Figure 48 - Figure 51 show the displacement field, the Von Mises stress distribution, the temperature field, and the thermal gradient vector sum distribution respectively within the three different final topologies. Each topology is reported together with a letter index and in particular: subscript a) refers to the pure thermal optimisation, subscript b) refers to the pure structural optimisation and subscript c) refers to the coupled optimisation. The same considerations made on the simple cases analysed in the previous paragraph are still valid. Observing the displacement vector sum in Figure 48, it is clear that the pure thermal topology optimisation is not able to predict the structural load causing an enormous displacement, i.e. the component would be broken. Looking at the other final topologies Figure 48b and Figure 48c, the displacement vector sum is always less or much less than 0.1 mm which can be considered an acceptable value for the analysed geometries, proving the verification of the structural constrains. The validity of this consideration is enhanced if the Von Mises stress distribution is observed in Figure 49. This quantity in the thermal optimisation presents great underloaded portions and other with stress peaks, i.e. it is highly irregular and ununiform. On the contrary, in the pure structural optimisation Figure 49b and in the coupled one Figure 49c this quantity is almost uniform within the final domain, especially in the pure structural optimisation as expected.

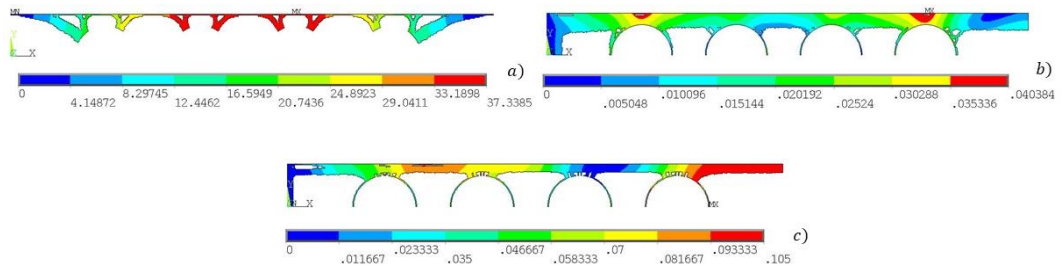


**Figure 48 - Displacement vector sum distribution [mm]**

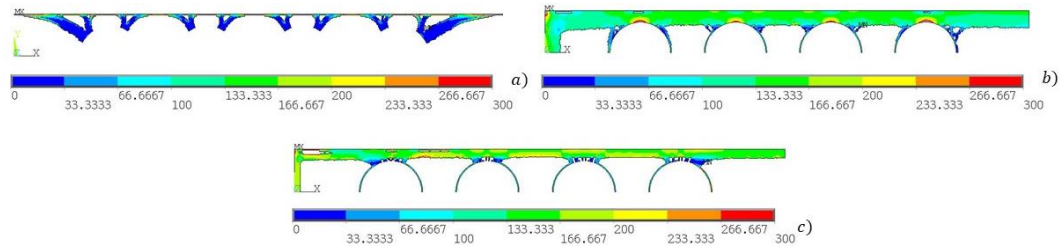


**Figure 49 - Von Mises ideal stress distribution [MPa]**

Similarly, looking at the temperature field Figure 50 and the thermal gradient vector sum distribution Figure 51, it is clear that the structural optimisation alone is not able to provide a good result. In particular, in the pure thermal optimisation, Figure 50a, the temperature fluctuations inside the domain are low. In the other optimisations, Figure 50b and Figure 50c the temperature undergoes more dispersions. For more, looking at the thermal gradient vector sum distribution of the thermal optimisation Figure 51a it is incredibly uniform within this final domain, while is highly scattered in the structural in Figure 51b. However, in the couple optimisation Figure 51c it is well distributed, a good compromise between the two extreme optimisations.

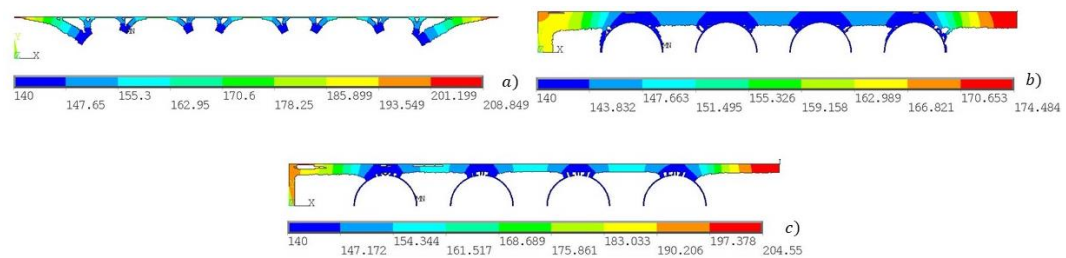


**Figure 50 - Temperature field [°C]**

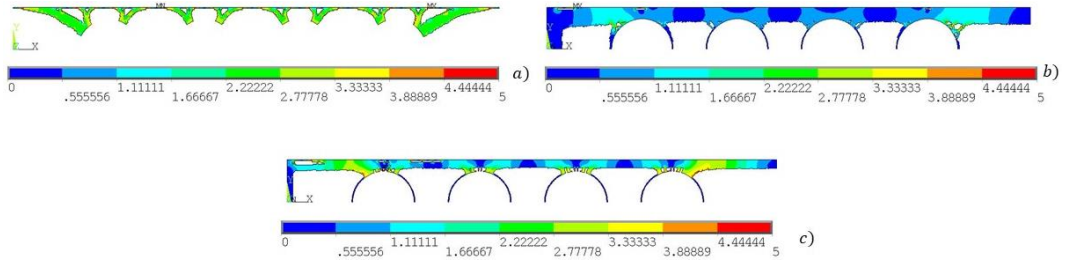


**Figure 51** - Thermal gradient vector sum distribution [ $^{\circ}\text{C}/\text{mm}$ ]

As a matter of fact, it is evident that the coupled optimisation is able to provide the best compromise between the two different limit conditions. In other words, it is able to provide a final topology in which no constraint is neglected, and heat exchange and structural stiffness are concurrently optimised. The same consideration cannot be made on the single optimisation cases, in fact the structural optimisation provides very poor result in terms of heat exchange, with disperse thermal gradient. Similarly, the single thermal optimisation leads to unfeasible topology under the structural loads.

Figure 52 displays the distribution of the thermo-mechanical energy density that is almost uniform around the reference value of  $\epsilon_{ref}$ . Overall, the coupled potential energy has been spread equally in the optimised structure, in accord with the analytical formulation, while stress and thermal gradient find in this topology the best compromise.

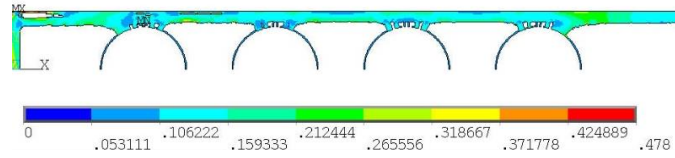


**Figure 52** - Thermostructural energy density distribution [MPa]

In order to highlight the potentialities of *TopTM*, Table 4 compares important quantities evaluated for the three final structures. The first row displays the maximum temperature  $\theta_{max}$  within the domain whereas the second the maximum displacement vector sum  $\bar{u}_{max}$ . The third and the fourth rows show the final mass  $M_{opt}$  per quarter of section and as a percentage with respect to the initial quarter cross section mass,  $M_{opt\%}$ . The structural stiffness,  $S^u$ , the v stiffness per unit of mass,  $s^u$ , the thermal stiffness,  $S^{\theta}$ , and the thermal stiffness per unit of mass,  $s^{\theta}$ , defined in Eq.26, are also reported in the last four rows of Table 4, respectively.

$$\begin{aligned}
 S^u &= \frac{\sqrt{F_x^2 + F_y^2}}{\bar{u}_{max}}; & s^u &= \frac{S^u}{M_{fin}} \\
 S^{\theta} &= \frac{Q}{\theta_{max}}; & s^{\theta} &= \frac{S^{\theta}}{M_{fin}}
 \end{aligned} \tag{26}$$

	<b>Thermal</b>	<b>Structural</b>	<b>Thermostructural</b>
$\theta_{max}$ [ $^{\circ}C$ ]	209	175	205
$\bar{u}_{max}$ [ $mm$ ]	37,339	0,040	0,105
$M_{opt}$ [ $g/mm$ ]	1,02	3,47	1,92
$M_{opt\%}$ [%]	16%	55%	30%
$S^{\theta}$ [ $Wmm^{-1}^{\circ}C^{-1}$ ]	0,0023	0,0028	0,0024
$s^{\theta}$ [ $Wmm^{-1}^{\circ}C^{-1} kg^{-1}$ ]	2,269	0,796	1,229
$S^u$ [ $Nmm^{-2}$ ]	0,34	318,20	121,22
$s^u$ [ $Nmm^{-2} kg^{-1}$ ]	337	91700	63135

**Table 4** - Comparison between optimisation results

According to Table 4, the temperature and the displacement after the structural optimization are the smallest, but the mass is significantly larger (more than 3 times  $M_{opt}$  obtained through thermal optimization and more than twice  $M_{opt}$  after the coupled thermo-structural optimization). Considering the thermal optimisation, it is clear that this solution is not feasible, since the displacement is out of scale, i.e. the component would break immediately under the structural loads. On the contrary, the displacement and the temperature in the coupled solution are reasonable and a good compromise between the separated optimisations. In addition,  $M_{opt}$  results to be remarkably smaller than  $M_{opt}$  obtained through a structural optimization. Moreover, the stiffnesses per unit of mass are concurrently enhanced after the coupled optimisation and tend to the values obtained by considering only the structural and the thermal optimisations (i.e., the highest achievable performances). It is worth to note that the thermal peak in the pure thermal topology optimisation is localised in a very little portion of material, as shown in Figure 50a, about just one or two elements. In order to have a rigorous comparison between all the optimisation, this value has been reported unaltered from the analysis. However, it would be sufficient to add a very little quantity of material in that point to remarkably reduce the temperature peak that is mainly due to a numerical instability. As already pointed out, the presented final topologies depend on the reference stress  $\sigma_{ref}$  and on reference thermal gradient  $\nabla\theta_{ref}$  prescribed at the beginning of the optimisation. In the present paper, qualitatively high values of these references have been employed to clearly show the effect of the optimisation and highlight the most critical zones in the component. Surely, in a real design phase, these references can be lowered, and the final mass would be much more increased. To conclude, this validation on a real component proves furthermore that *TopTM* is able to provide the optimized compromise between the structural and the thermal constraints, providing a final topology characterized by high structural and thermal performances and reduced mass.

In Figure 53 the final radiator is displayed. In particular, the figure shows an internal section of the radiator in order to highlight the redesigned topology and proving that topology obtained with *TopTM* can be easily converted in a CAD file. Nevertheless, the proposed final topology doesn't consider manufacturability constraints. As it can be noticed, the great mass removal especially close to the cooling channels may be problematic in the manufacturing phase. It is worth to note that, as for other commercial software for topology optimization, the manufacturing constraints have not been considered, since the aim of topology optimization is to provide the ideal mass distribution under selected loads and constraints. Considerations on the specific manufacturing limits and constraints have to be faced during the rebuilding of the model. Indeed, topology optimisation provides a guideline about the best material distribution within a certain domain and under some constraints and boundary conditions.



**Figure 53** - redesign by *TopTM* of real LHP radiator

## 2.4 *TopTM* final remarks

Before *TopTM*, components subjected to mechanical and thermal loads were generally optimized with separate mechanical and thermal optimizations. Moreover, in many cases thermal loads were not considered and only structural topology optimization was carried out. *TopTM* is able to optimise under simultaneous thermo-mechanical constraints and objectives any components. Some main final remarks can be summarized as follows:

- 1) The theoretical condition for the optimum consists in the uniform thermo-mechanical energy density distribution, with the convergence reached within few iterations. In all analysed cases full or void material distribution without intermediate properties has been achieved after about 40 iterations.

- 2) *TopTM* permits to obtain the maximum material exploitation, reaching the optimized heat exchange and stiffness concurrently. Indeed, for a component subject to coupled loads, *TopTM* is able to provide the best compromise, optimising concurrently the above-mentioned quantities and respecting the coupled constraints.

- 3) *TopTM* has been successfully validated on an LHC radiator for aerospace application, proving its applicability in real and complex cases. As it can be

observed from the reported data, within the final structure, the heat exchange and the structural stiffness are maximised. From the topology optimisation result, it had been possible to redesign entirely the component quite easily. Hence, it had been possible to obtain a CAD model, first step in the manufacturing chain.

# Chapter 3

## *TopComp*: fibre and topology optimisation

### 3.1 Composite material topology optimisation

Over the last decades, the use of fibre-reinforced composite (FRC) structures has significantly increased in many industrial sectors (e.g., automotive, aerospace). Fibre-reinforced composites are made of axial particulates embedded in fitting polymer matrices. The primary objective of fibre-reinforced composites is to obtain materials with high specific strength and high specific elastic modulus, which means high strength and stiffness with respect to weight [13]. Therefore, they are widely employed for the production of structural lightweight components in several sectors such as automotive, aerospace, and offshore extraction. FRC laminates are currently manufactured with different production processes, like roll wrapping, spray-up or compression moulding. The Classical Lamination Theory (CLT) parameters, such as layer thickness, layer fibre orientation, number of layers, significantly affect the mechanical properties of the FRC [86]. Therefore, depending on the specific application, the optimisation of these parameters is fundamental to maximize the performance of the FRC composite [87,88].

As already described previously, novel AM processes permit to create highly customised fibre reinforced composites (FRC). There is an increasing interest in the use of AM processes for the production of FRC components since they have the possibility to substitute metals parts with great saving in terms of mass and weight. Hence, specific design methodologies for AM FRC are needed to obtain fully optimised parts.

In the literature, multi-objective topology optimisation methodologies are currently employed to design FRC components to be produced through AM processes. The research focused on the development of algorithms which can consider both the topology and the fibre orientation in the optimisation process.

One of the first research in this field has been proposed by [89] who optimized the orientational and density distribution for a short cantilever problem. As well, [90] extended SIMP technique to simultaneous fibre-angle and topology design of composite laminae in a cellular automata (CA) framework. Other approaches more related to the production processes have been suggested such as methodologies capable to define the optimum geometry and the best lamination

parameters for composites produced through classic manufacturing processes [91–93].

Recently, algorithms for the optimisation of laminates to be produced through AM processes have also been proposed in the literature. Considering FRC printing, Safonov [94] proposed a new method capable of simultaneously optimise the density distribution (i.e., the topology) and the local fibre orientation using an evolutionary method. The design algorithm should provide the topology and the local fibre orientation in each lamina together with the stacking sequence. Indeed, *TopComp* focuses on these AM layered structures and provides the required design information. Considering fibre orientation, two families of algorithms, Discrete Material Orientation (DMO) or a Continuous Fibre Angle Orientation (CFAO), have been analysed in the literature. In particular, in the DMO methodology, a discrete set of different angles, which are a-priori assumed or calculated during the optimisation process [95,96], are imposed in the optimisation process. On the other hand, in the CFAO technique, each point of the material can have its specific fibre orientation and, therefore, the fibre orientation can continuously vary within the domain [97,98]. *TopComp* belongs to this last family of fibre optimisation approaches.

The optimisation sequence is another fundamental parameter. Namely, both the fibre orientation and the topology optimisation share the aim of maximising the stiffness of the system and fully exploit the material. However, the same objective can be obtained by considering topology optimisation and fibre orientation simultaneously or sequentially. For example, [96] has proposed a sequential method, which involves, at first, the definition of the component topology and, thereafter, the assessment of the fibre density and orientation. Despite of that, [97] and [95] have suggested to simultaneously optimise the topology and the fibre orientation. In particular, during each cycle of the optimisation process, both the topology and the fibre orientation are concurrently considered. Clearly, the use of different optimisation strategies affects the results and brings to different shapes and fibre distributions. For example, the sequential approach is faster and computational cheaper with respect to the simultaneous one. However, for materials with a strong anisotropy it can provide final structures with undesired stress peaks absent using the simultaneous optimisation. On the other hand, simultaneous methods work properly also for composite materials characterized by a strong anisotropy.

However, the available simultaneous methods exhibit some shortcomings, as the difficulty of reaching the global minimum [96] and the need for corrections and filtering techniques if the SIMP method is used to solve the optimisation problem [57]. At present, a simultaneous approach which permits to reach the global minimum, and it is not affected by critical numerical instabilities is not present in the literature.

*TopComp* is able to optimize simultaneously the fibre orientation and the topology. In the following chapter, the analytical method proposed in [58,64] for isotropic materials is adapted to anisotropic materials and the procedure for the simultaneous coupled optimisation is defined. This method is able to guarantee

the global optimum and provide the final topology without a priori volume constraints. Lastly, *TopComp* is verified on several literature benchmarks and compared to a sequential method. In addition, the optimal geometry and fibre orientation of a 3D part is obtained and analysed.

## 3.2 *TopComp* solution

In this paragraph, the analytical formulation of *TopComp* is defined. Firstly, the analytical formulation of the topology optimisation problem for an anisotropic material is reported. The problem solution leads to the optimality criterium that is the uniform distribution of strain energy density, i.e. the best material distribution is the one with all the material subjected to the same deformation. Secondly, the FRP constitutive matrix is obtained and analysed. The optimality criterion, which permits to define the fibre orientation that maximises the stiffness, is outlined in the following. Finally, the methodology that permits to couple topology optimisation and optimized fibre orientation in a multi-objective programming problem is presented.

### 3.2.1 Optimality criterium for material distribution

Let  $\Omega$  be a domain of existence limited in the space,  $\Omega \subseteq \mathbb{R}^3$  and containing the material  $M$ , with regular frontier  $\Gamma$  as shown in Figure 54. The spatial coordinates are  $x, y, z$  (in vector notation  $\mathbf{x} = \{x, y, z\}$ ), whereas the displacement field of  $M$  is  $\mathbf{u} = \mathbf{u}(\mathbf{x})$ . In the following, bold letters stand for vector quantities.

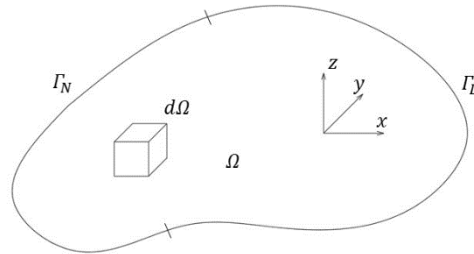


**Figure 54** - Design Domain for a generic material

The material  $M$  is considered linear anisotropic. The equation that establishes the load equilibrium of an infinitesimal portion  $d\Omega$  in a generic body is reported in Eq.27:  $\sigma_{ij}$  is the stress tensor ( $\sigma_{ij} \in \mathbb{R}^{3 \times 3}$ ),  $x_j$  are the independent spatial variables ( $x_j \in \mathbb{R}^3$ ),  $f_i$  are the applied forces per unit volume ( $f_i \in \mathbb{R}^3$ ). Neumann boundary conditions are applied to the part of the frontier called  $\Gamma_N$  (second equation in Eq.27) and Dirichlet boundary conditions are applied to the part of the frontier called  $\Gamma_D$  (third equation in Eq.27). Together, they must verify the condition of completeness of the boundary conditions defined in [79]. In Eq.27,  $n_i$  is the unit vector normal to the frontier  $\Gamma_N$  ( $n_i \in \mathbb{R}^3$ ),  $\bar{\tau}_i$  is the imposed stress on frontier  $\Gamma_N$  ( $\bar{\tau}_i \in \mathbb{R}^3$ ) and  $\bar{u}_i$  is the imposed displacement on frontier  $\Gamma_D$  ( $\bar{u}_i \in \mathbb{R}^3$ ).

$$\begin{cases} \frac{\partial \sigma_{ij}}{\partial x_j} = -f_i & \text{in } \Omega & i, j = 1, \dots, 3 \\ \sigma_{ij} n_i = \bar{\tau}_i & \text{on } \Gamma_N & i, j = 1, \dots, 3 \\ u_i = \bar{u}_i & \text{on } \Gamma_D & i = 1, \dots, 3 \end{cases} \quad (27)$$

The term  $\sigma_{ij}$  can be expressed in term of strains  $\mathbf{e} = e_{ij}$  by means of the constitutive matrix  $\mathbf{A} = a_{ij}$ . Since the coefficients of this matrix must satisfy the symmetry and positivity conditions [79], it is possible to obtain the expression of the potential energy of the system Eq.28,  $\Pi(\mathbf{u})$ , according to [58].

$$\begin{aligned} \Pi(\mathbf{u}) &= \frac{1}{2} \int_{\Omega} \mathbf{e}^T(\mathbf{u}) \mathbf{A} \mathbf{e}(\mathbf{u}) d\mathbf{x} - \int_{\Omega} \mathbf{f}^T \mathbf{u} d\mathbf{x} - \int_{\Gamma_N} \bar{\boldsymbol{\tau}}^T \mathbf{u} d\Gamma = \\ &= -\frac{1}{2} \int_{\Omega} \mathbf{e}^T(\mathbf{u}) \mathbf{A} \mathbf{e}(\mathbf{u}) d\mathbf{x} = -\frac{1}{2} \left( \int_{\Omega} \mathbf{f}^T \mathbf{u} d\mathbf{x} + \int_{\Gamma_N} \bar{\boldsymbol{\tau}}^T \mathbf{u} d\Gamma \right) \end{aligned} \quad (28)$$

In order to define the structural optimisation problem, it is necessary to define an artificial variable, called  $\eta$ . This variable represents the material effectiveness, i.e. the participation rate of the material in the component behaviour, in each point of the domain  $\Omega$ . In other words,  $\eta$  stands for the presence and consistency of the material in the domain, point by point. The variable  $\eta$  must be limited both by an upper boundary  $\eta_{max}$  and by a lower boundary  $\eta_{min}$  [58]. The expression of this variable is reported in Eq.16.

The topology optimisation problem, reported in Eq.29, consists in finding the distribution of  $\eta(\mathbf{x})$  that maximises the stiffness for a volume  $\bar{V}$ .  $\bar{V}$  is a portion of the initial volume and the second equation in Eq.29 represents the volume optimisation constraint.

$$\begin{cases} \max_{\eta} \Pi(\eta, \mathbf{u}) = \min_{\eta} \frac{1}{2} \int_{\Omega} \mathbf{e}^T(\mathbf{u}) \mathbf{A} \mathbf{e}(\mathbf{u}) \eta d\mathbf{x} & s. t. \\ \int_{\Omega} \eta d\Omega \leq \bar{V} \\ 0 < \eta_{min} < \eta < \eta_{max} < \infty \end{cases} \quad (29)$$

The optimisation problem shown in Eq.29 can be solved by using the *Lagrange multipliers method*. In particular, the Lagrangian function,  $L(\eta, \lambda, t)$ , has to be defined and all its derivates must be equal to zero (Eq.30).

$$L(\eta, \lambda, t) = \frac{1}{2} \int_{\Omega} \mathbf{e}^T(\mathbf{u}) \mathbf{A} \mathbf{e}(\mathbf{u}) \eta d\Omega - \lambda \left( \int_{\Omega} \eta d\Omega - \bar{V} + t^2 \right) \quad (30)$$

Where  $\lambda$  is the *Lagrange multiplier* and the term  $t$  is an additional variable employed to simplify the solution of the system.  $\lambda$  results to be equal to the *strain energy density*  $\epsilon$  and its expression is reported in Eq.31.

$$\lambda = \frac{\frac{1}{2} \int_{\Omega} \mathbf{e}^T(\mathbf{u}) \mathbf{A} \mathbf{e}(\mathbf{u}) d\Omega}{\int_{\Omega} d\Omega} = \epsilon \quad (31)$$

If the problem is discretized, e.g. using the Finite Element Method (FEM), the equations are defined on  $N_{elem}$  portions of the domain called  $\Omega_e$  and also the effectiveness variable  $\eta$  must be discretised:

$$\begin{cases} \eta(\mathbf{x}) = \eta_e & \forall \mathbf{x} \in \Omega_e \quad e = 1, \dots, N_{elem} \\ 0 < \eta_{min} < \eta_e < \eta_{max} < \infty \end{cases} \quad (32)$$

Following the same passages shown in Eqs.27-31 the value of the *Lagrange multiplier* for each element can be evaluated as follows:

$$\lambda = \frac{\frac{1}{2} \mathbf{e}_e^T(\mathbf{u}) \mathbf{A} \mathbf{e}_e(\mathbf{u}) \Omega_e}{\Omega_e} = \epsilon_e = \epsilon \quad e = 1, \dots, N_{elem} \quad (33)$$

The multiplier  $\lambda$  must be the same both in the global continuum structure and in each single portion of the discretised one. Hence, the strain energy density in each portion  $\Omega_e$  must be the same. Accordingly, the strain energy density in the optimal structure must be *uniformly distributed*. This represents the optimality criteria for any type of material which has a constitutive matrix like  $a_{ij}$ .

### 3.2.2 Optimality criterium for fibre orientation

Below the *TopComp* optimality criterium for fibre orientation is defined. From an analytical point of view, an FRC lamina behaves like an orthotropic material if the reference system for computing the compliance matrix is aligned with the fibre direction (e.g., the reference system with coordinate axes 1, 2 and 3 in Figure 55). In particular, in Figure 2 the axes 1 – 2 define the plane of the lamina (i.e., the axis 1 is parallel to fibre direction and the axis 2 is perpendicular to fibre direction) and the axis 3 is normal to this plane. In this coordinate system, the lamina compliance matrix, the inverse of  $a_{ij}$ , is called  $\mathbf{C} = c_{ij}$ .

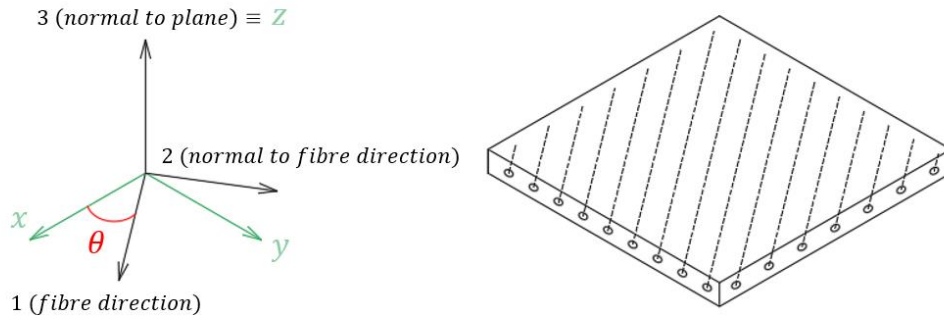


**Figure 55** - FRC problem coordinate system

If another coordinate system is taken into consideration, as the  $x - y - z$  coordinate system in Figure 55, with the same out of plane axis (i.e., axis 3 and axis  $z$  coincide) but with the in-plane axes  $x - y$  rotated by an angle  $\theta$  with respect to axes 1 – 2, the compliance matrix is subjected to a rotation transformation.

The transformed compliance matrix  $\bar{\mathbf{C}}$ , in the rotated  $x - y - z$  coordinate system has twelve different coefficients  $\bar{c}_{ij}$  that depend on the nine material parameters  $E_1, E_2, E_3, \nu_{12}, \nu_{13}, \nu_{23}, G_{12}, G_{13}, G_{23}$  and on the angle of rotation  $\theta$ .

The transformed compliance matrix  $\bar{\mathbf{C}}$  allows to evaluate the properties of the lamina in a generic rotated coordinated system. Moreover, it provides the compliance matrix of the lamina which has orientation  $\theta$  with respect to a fixed reference system aligned with the fibre orientation.

In the proposed method, the orientation angle  $\theta$  for the fibres is chosen according to the principal stress criterion. In particular, the fibres are aligned with the maximum principal stress in the plane. According to [90,99], if the fibres are aligned with the maximum principal stress in the plane, the stiffness is maximized. Therefore, the aim of the proposed multi-objective optimisation is to uniformly distribute the strain energy density and to align the fibres along the principal direction. In order to achieve this objective, the first step is to generate the design domain with loads and constraints. Since the fibre directions are not known at the beginning, in this first step an artificial isotropic material is considered. Nevertheless, the employment of the artificial isotropy does not distort the results, as proved in [97]. As for the optimisation process, the second step involves the discretization of the component volume. Accordingly, each element can be considered as a lamina itself and all the previous considerations (i.e., constitutive matrix and orientation parameter  $\theta$ ) are still valid, thus permitting to orient the fibre direction of each element. Once the principal directions for each element are locally evaluated, the FRC is generated.

### 3.2.3 Coupled topology optimisation

The algorithm developed to simultaneously couple the material distribution and the fibre orientation process is schematically shown in Figure 56.

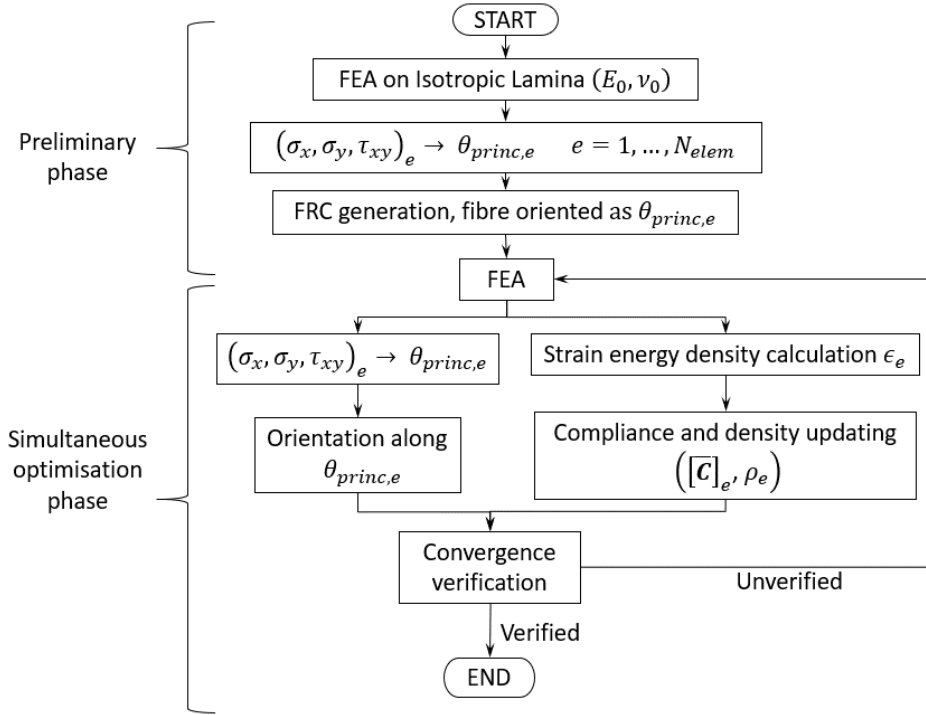


Figure 56 - TopComp flowchart

According to Figure 56, the first phase for the coupled optimisation process involves the assessment of the stress distribution in order to define the stress principal directions for each element (i.e.,  $\theta_{princ,e}$  for the  $e_{th}$  element). The process has been developed by considering an isotropic material, with elastic modulus  $E_0$  and Poisson ratio  $\nu_0$  (i.e.,  $E_0 = E_1 = E_2 = E_3$ ,  $\nu_0 = \nu_{12} = \nu_{13} = \nu_{23}$ ,  $G_0 = G_{12} = G_{13} = G_{23}$ ). An FRP is thereafter generated by aligning the fibre for each element along the principal stress direction. This represents the preliminary phase of the optimisation process. The second phase involves an iterative process aiming at assessing the optimized topology and fibre orientation. During the iterative phase, at first an FEA is carried out in order to assess the principal direction  $\theta_{princ,e}$ , and the strain energy density  $\epsilon_e$  for each element. Then all the fibres are locally aligned along the principal directions  $\theta_{princ,e}$  for each element. At the same time, the strain energy density is used to update the material distribution by means of the artificial variable expressed in Eq.33. In order to link this artificial variable to the real material parameters the compliance matrix is employed as shown in Eq.34.

$$\eta_e = \frac{[\mathbf{C}]_0}{[\mathbf{C}]_e} \quad e = 1, \dots, N_{elem} \quad (34)$$

$$0 < 10^{-4} \div 10^{-5} \leq \eta_e \leq 1 < \infty \quad e = 1, \dots, N_{elem}$$

In the previous Equation,  $[\bar{\mathbf{C}}]_e$  denotes the value of the compliance matrix on element  $e$ . In addition,  $[\bar{\mathbf{C}}]_0$  represents the compliance matrix of the base material before the optimisation. The maximum value is represented by the *full stiff* material, i.e.  $\eta_{max}$  is unitary and  $[\bar{\mathbf{C}}]_e$  is equal to  $[\bar{\mathbf{C}}]_0$ . On the contrary, the minimum value should be zero since it denotes an *empty* material. However, the zero value should be avoided in numerical approximation since it could bring to instabilities. A good approximation for  $\eta_{min}$  is around  $10^{-4}$  to  $10^{-5}$  [58]. In this case,  $[\bar{\mathbf{C}}]_e$  is much greater than  $[\bar{\mathbf{C}}]_0$ , in other words the element  $e$  is fully compliant. The material consistency is updated, considering an undefined number  $p$  of iterations, as reported in Eq.35, which represents the updating law of the optimisation process. This law can be achieved by following the same passages in [58] coupling Eqs.31, 32 and 34.

$$[\bar{\mathbf{C}}]_e^{j+1} = \frac{\epsilon^j}{\epsilon_e^j} [\bar{\mathbf{C}}]_e^j \quad e = 1, \dots, N_{elem} \quad j = 1, \dots, p \quad (35)$$

The convergence to the optimized solution can be checked in several ways. One criterion can be the verification of a minimum difference between the volume at the  $j_{th}$  step and the objective volume  $\bar{V}$ . According to [58], a percentage difference of 0.1% between these values for three consecutive iterations can be considered a good approximation. In particular, if this condition is verified, the convergence is reached.

A second criterion concerns the analysis of the strain energy. In this case, before the optimisation process, an optimal strain energy density in the structure  $\bar{\epsilon}$  [58] is defined. The convergence is reached if the percentage difference between  $\bar{\epsilon}$  and the average strain energy density evaluated in the structure is inferior to 0.1% for three consecutive iterations. The choice of  $\bar{\epsilon}$  can be based on displacement, stiffness, or stress constraints.

The analytical formulation for the assessment of the optimized topology and the fibre orientation can be also implemented with a sequential approach Figure 57. In the first phase, the material is considered isotropic, and the optimized topology is defined. In the second phase, the principal directions are evaluated in each element and the FRC is generated by orienting the fibre along these directions. In the sequential method this last operation is required just once, at the end of the topology optimisation process. On the contrary, in the simultaneous approach Figure 56 the orientation of the fibres is required in each cycle. Therefore, it is clear that the simultaneous method is computationally more expensive than the sequential one. However, this last method could bring to sub-optimized structures.

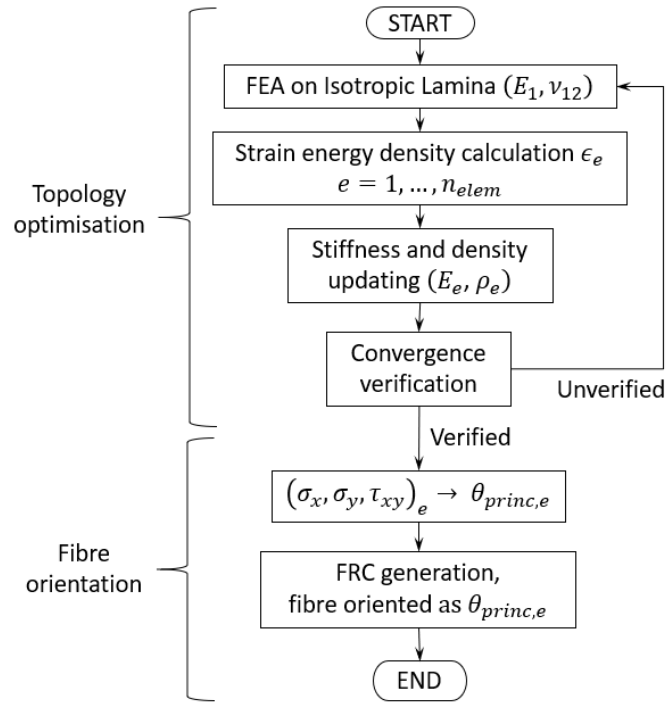


Figure 57 - *TopComp* sequential approach

### 3.3 *TopComp* results

In this paragraph, the *TopComp* algorithm is verified on several benchmark and test cases. Firstly, the proposed algorithm is verified with two benchmarks taken from the literature [95,97]. The simultaneous and the sequential approaches are thereafter compared in order to highlight the main differences between the two processes. Finally, *TopComp* is applied to a three-dimensional component.

The proposed algorithms are implemented in the commercial software ANSYS Mechanical. In particular, an Ansys APDL code has been written to execute the optimisation processes, following the flow charts showed in Figure 56 and in Figure 57. It can be fully run as an ANSYS routine proving its versatility and ease of use. As for *TopTM*, the code copies step by step what reported in the flowcharts taking all the required information, such as strain energy density, stiffness, and volume directly from ANSYS postprocessing data.

#### 3.3.1 Benchmarking validation

For a first verification, two benchmarks proposed in the literature are considered. In Figure 58a the optimized topology for the short cantilever beam obtained by [95] is reported. This image displays the final material distribution and the continuous orientation of the fibres, represented by black lines inside the matrix. Figure 58b displays the structural model, in [95] a detailed description of dimensions, loads and materials is present. Figure 58c shows the final material distribution obtained by employing the proposed simultaneous optimisation. In order to compare the topology in [95] and the one obtained through *TopComp*,

the edges of Figure 58a (solid black continuous line) are superimposed on Figure 58c. It can be noticed that the number and position of the holes is the same. In addition, the thickness of the connecting rods is almost the same, with limited differences. The only slight difference is the position of the right cross like portion of the structure. Nevertheless, it is reasonable since a different optimisation method and FE solver are employed.

Figure 58d shows the fibre orientation within the matrix obtained with *TopComp*. Namely, the fibres are aligned with the directions of the rods, as found in [95] and shown in Figure 58a.

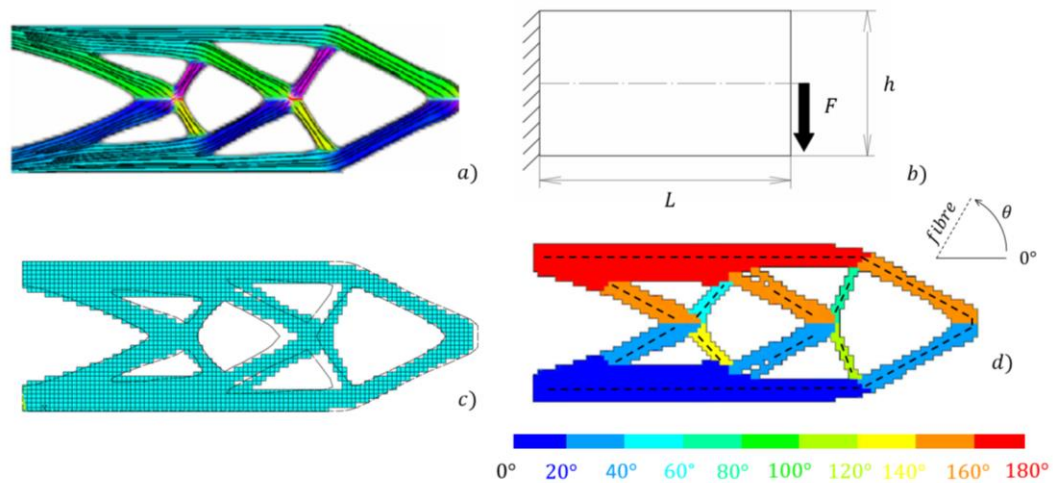


**Figure 58** - First *TopComp* 2D benchmark

In Figure 59a, the topology obtained by [97] is shown. The design domain is a simple cantilever beam loaded by a vertical force on the bottom-right corner as shown in Figure 59b. As for the previous benchmark, the reader is referred to [97] for a detailed description of boundary conditions and material parameters. The optimized topology obtained through the proposed algorithm is shown in Figure 59c together with the topology obtained by [97] (solid black continuous line). It can be easily seen that the topologies are almost equal except for the thicknesses of the bottom and right rods that are lightly different. However, the same considerations for the previous case are still valid. Moreover, the same value of strain energy (2.471 Nmm) is obtained in the present paper and in [97]. For this case as well, the fibres are aligned with the directions of the rods (Figure 59d).

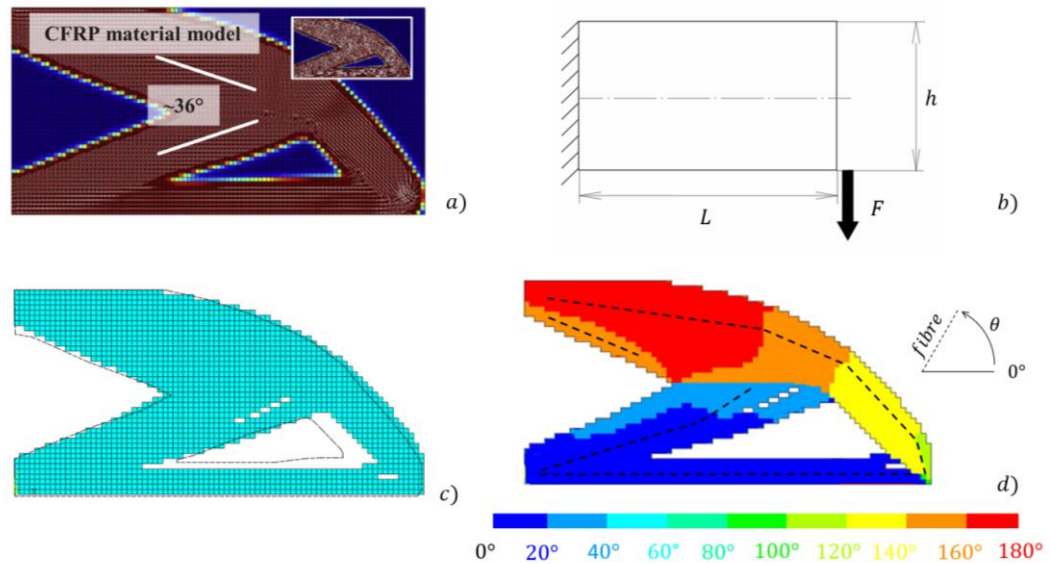


Figure 59 - Second *TopComp* 2D benchmark

### 3.3.2 Sequential and simultaneous approach

In this paragraph, a comparison between the simultaneous and the sequential approaches is carried out. The *TopComp* sequential approach is faster and computationally cheaper. However, as it will be demonstrated hereafter, for composite materials with a strong anisotropy, the optimized topology can be significantly different. To highlight this critical aspect, let us consider the commercial composite material graphite-epoxy (AS/3501) with the material properties reported in Table 5 [80]. The same structural model shown in Figure 58b are considered: the left side is fully clamped,  $L = 200 \text{ mm}$ ,  $h = 100 \text{ mm}$  and  $F = 1 \text{ kN}$ . Both in sequential and simultaneous optimisation a reference strain energy density of 0.0362 MPa is imposed. In order to obtain comparable results, the Young's modulus and the Poisson ratio are set equal to  $E_1$  and  $\nu_{12}$ , respectively, in the first topology optimisation phase. Five thousand 8-nodes plane elements with unit thickness are used in the models. In both cases, the convergence has been reached in less than 50 iterations and no middle-density elements are found at the end of the process.

	$E_1$ [MPa]	$E_2$ [MPa]	$E_3$ [MPa]	$\nu_{12}$	$\nu_{13}$	$\nu_{23}$	$G_{12}$ [MPa]	$G_{13}$ [MPa]	$G_{23}$ [MPa]
AS/3501	137935	8966	8966	0.3	0.3	0.3	7104	7104	6208

Table 5 - FRC material data

Figure 60 compares the topology and the fibre orientation obtained with the *TopComp* simultaneous and the sequential approach. In particular, Figure 60a and Figure 60b show the topology and the fibre orientation obtained for the investigated cantilever beam with a simultaneous approach, respectively. In

Figure 60c and Figure 60d the topology and the fibre orientation obtained with the sequential approach are shown, respectively.

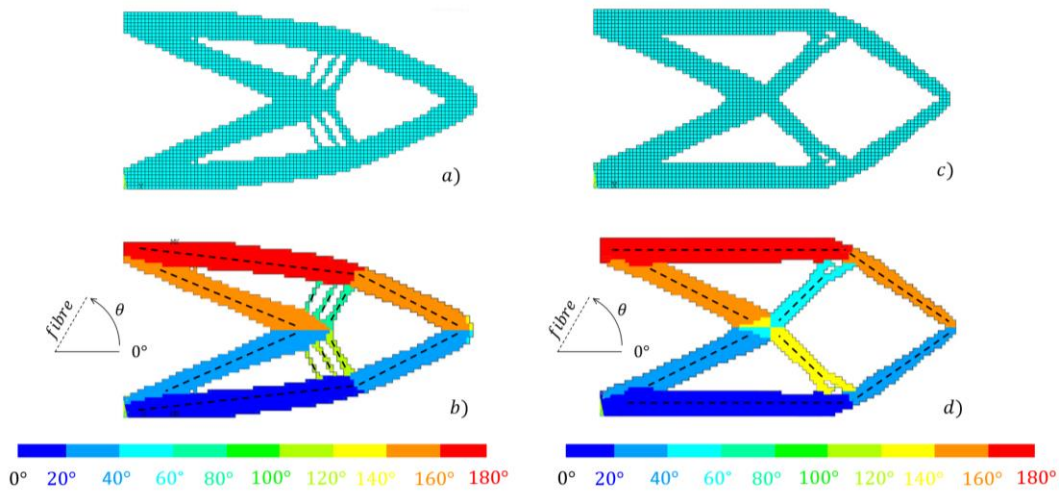


**Figure 60** - *TopComp* simultaneous vs sequential approach

By comparing Figure 60a and Figure 60c, the final shapes obtained with simultaneous and sequential approaches are significantly different. The final topology of the sequential approach is obtained by considering an isotropic material. It is obtained employing the algorithm described in [58] without modifications. In addition, all the fibres are aligned along the rod directions since these are the principal directions in the final structure (Figure 60d). For what concerns the final topology obtained by simultaneous approach, the angles of inclination of the rods are smoother than in the sequential case. Again, the fibre orientation coincides with the inclinations of the rods (Figure 60b). The differences between the two topologies are mainly due to the large anisotropy of the investigated FRC which is not considered in the topology generation of the sequential process. It is worth to note that sharp changes of direction within the component may lead to fibre orientations that are perpendicular each other. This induces large deformations in the structure and local peak stresses, due to the anisotropy. On the contrary, if the fibre orientation and the strain energy density are optimised simultaneously, sharp changes of the fibre direction are avoided, since during each iteration the strain energy density is uniformly distributed. At the end of the process, the rods are linked with angles that are different from  $90^\circ$ . Figure 61 shows the elastic strain energy density distribution within the optimized component obtained through a simultaneous approach (Figure 61a) and through a sequential approach (Figure 61b). Figure 61c shows a magnification of the strain energy peak in the optimized topology obtained through a sequential approach.

According to Figure 61a, no strain energy peaks are present. On the contrary as shown in Figure 61b and Figure 61c, a large strain energy peak at the centre cross-like portion of the structure is present, in the region where the rods are perpendicularly to each other. The value of the elastic strain energy density in that

point is 1.13 MPa, whereas it is averagely equal to 0.05 MPa in the rest of the structure. Hence, it can represent a point of static failure or the possible starting point for a fatigue crack. It should be noted that this local strain energy increment inside the material is far from the zones where the boundary conditions are applied, so it cannot be considered as a numerical instability.

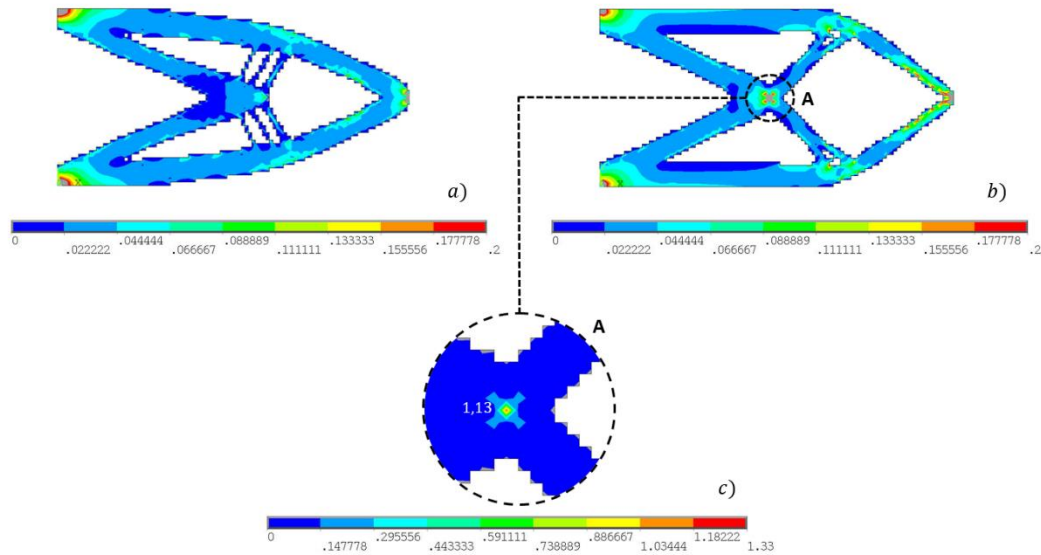


**Figure 61** - Elastic strain energy density [MPa]

For what concerns the global stiffness and the volume reduction of the structure, the results are reported in Table 6. In particular, the structure obtained through the simultaneous approach has a larger specific stiffness (i.e., the ratio between the global stiffness and the total volume) and, most important, it avoids the presence of peak stresses.

	Simultaneous optimisation	Sequential optimisation
Final Volume [mm <sup>3</sup> ]	8415	8090
Maximum displacement [mm]	0.614	0.662
Global stiffness [Nmm <sup>-1</sup> ]	1629	1511
Stiffness per unit volume [Nmm <sup>-4</sup> ]	0.194	0.187

**Table 6** - *TopComp* data result with different approaches

This analysis confirms the effectiveness of the simultaneous approach and it also highlights that, with the sequential approach, strain energy density concentrations may dangerously occur, especially for materials characterized by a strong anisotropy.

### 3.3.3 3D component optimisation

For the verification of the simultaneous approach with a 3D component, the parallelepiped design domain with a squared base reported in Figure 62 is analysed. The parallelepiped is characterized by height  $h$  equal to 10mm and length  $L$  equal to 50mm. In the four squared areas with striped background in Figure 62 with side length  $t$  equal to 2mm, the nodal displacement is set equal to 0. Two nodal forces  $F$  with intensity of 500N along the  $z$  direction are applied on the two squared areas with white background on the right end of the plate (at the middle of the length  $L$ , on the upper and lower faces). The material properties are the same reported in Table 5 and the fibres are assumed to be perpendicular to the  $z$ -axis. The design domain is sliced in laminae with thickness equal to  $s$  along the  $z$ -axis. The aim of this optimisation is to provide the three-dimensional topology as the combination of single laminae together with bidimensional optimal fibre distribution of each lamina.

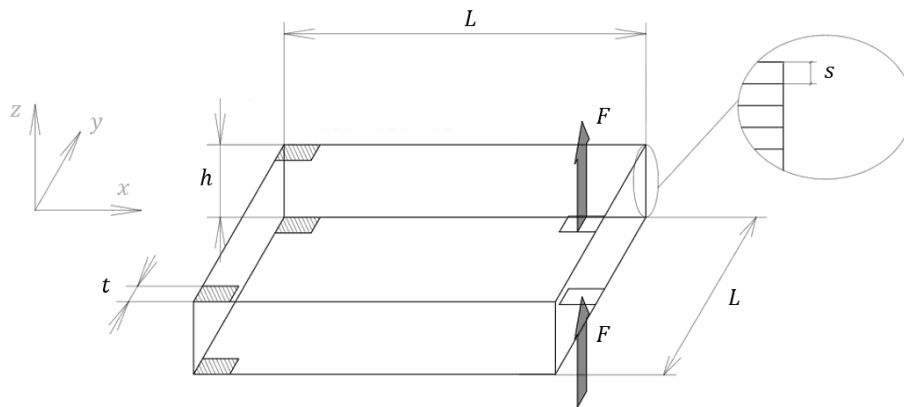


**Figure 62** - Three-dimensional design domain with constraints

The *TopComp* simultaneous approach is used to optimise the component. In order to discretize the domain, a mesh, made of twenty-five thousand 20-nodes brick elements, is used. The commercial solver Ansys Mechanical is employed for the FEA. The final topology is shown in Figure 63: the convergence has been reached in 39 iterations with no middle-density elements.

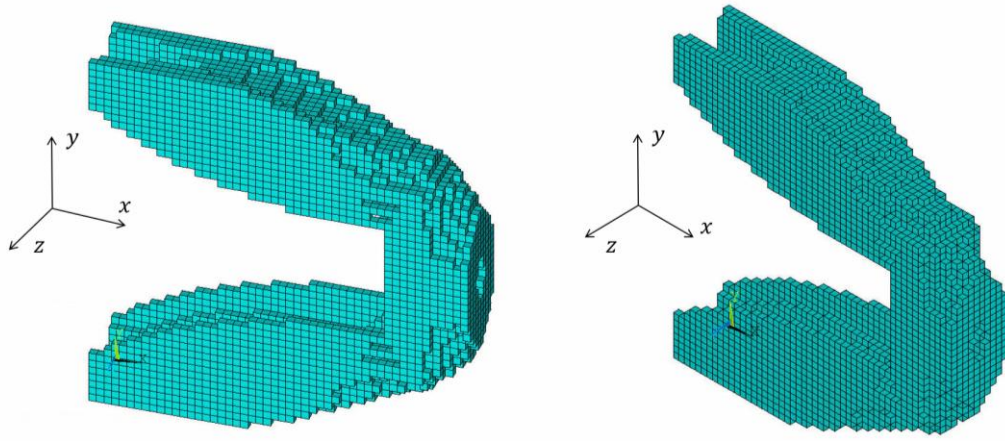


**Figure 63** - *TopComp* on a three-dimensional component

The mechanical properties along the z-axis are assumed to be isotropic since the fibres lie exclusively on x-y plane. Therefore, in z-direction, the mechanical properties are constant in the whole component with stiffness module equal to  $E_3$  and Poisson ratio equal to  $\nu_{13}$ . The final topology and the fibre orientation of each layer are reported in Figure 64, together with the stacking sequence along the z-axis (Figure 64 (1) is the first layer, whereas Figure 64 (10) is the last layer). Clearly, the global topology in Figure 63 can be seen as the combination of these ordinated layers. Since the total height  $h$  and thickness are imposed by the load conditions, the number of resulting layers is 10.

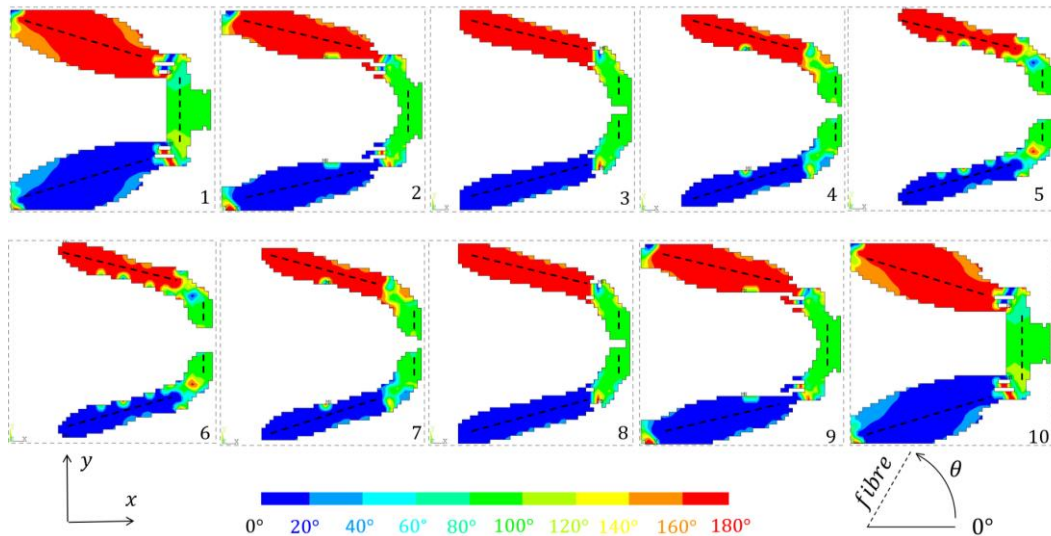


**Figure 64** - *TopComp* layered result with fibre direction

It should be noted that *TopComp* does not consider the principal stress along the z direction. The orientations found on each layer represent the projection of the 3D principal directions in the x-y plane. So, if the state of stress is strongly oriented along the z-axis (i.e., the stress along the z direction is significantly larger than the stress in the plane), the difference between the fibre orientation in each layer increases. However, it worth to note that, the presented algorithm is thought for those manufacturing processes able to produce only stacks of bidimensional

laminae. Therefore, the fibre can be oriented only in the x-y plane and this is the reason why the most critical loads should lie in this plane.

### **3.4 *TopComp* final remarks**

Overall, *TopComp* is capable to simultaneously optimise the fibre local orientation and to define the optimized topology of FRC.

*TopComp* has been verified with benchmarks found in the literature. It is shown that checker-boarding effects and middle-density elements do not occur and that no filtering tools are needed to obtain the global maximum. The reason is related to the optimality criteria chosen, similarly to *TopTM*.

*TopComp* has been also compared with its sequential algorithm counterpart, which is cheaper from a computational point of view. The numerical comparison shows that, with a sequential algorithm, peak stresses are possible, especially for composite materials characterized by a strong anisotropy. On the other hand, with the simultaneous proposed approach, the stress is uniformly distributed within the component and peak stresses are avoided.

Furthermore, *TopComp* has been successfully applied to a 3D component. In particular, the 3D topology has been obtained as the combination of laminae together with the bidimensional fibre distribution of each lamina. This information is perfectly suitable for fibre-reinforced composites (FRC) manufacturing through Additive Manufacturing (AM) processes.

To conclude, *TopComp* exploit the possibility to produce composite components with limited manufacturing constraints through AM processes. It permits an effective lightweight design, with significant advantages in terms of weight and mechanical performance in many industrial sectors, like aerospace, automotive, motorsport, aviation, and robotics.

# Chapter 4

## *TopFat*: defect driven topology optimisation

### 4.1 Defect population and topology optimisation

As already discussed in the first part of this dissertation, topology optimisation provides an ideal tool for the design of optimized components [10,22,80,100,101] to be produced with additive manufacturing processes. Generally, topology optimisation permits to find the ideal material distribution to optimize one or more properties (e.g., stiffness) under various constraints [11]. Commonly, the objective of topology optimisation is to maximise the stiffness of the structure under a volume constraint. However, in this case the maximum allowable stress in the structure is not considered and the optimized topology can hardly be used since it probably does not meet the safety requirements. For this reason, limits on the allowable stress, depending on the application, must be included in the topology optimisation problem formulation. Generally, when a component is designed with a topology optimisation algorithm, the stress is limited by considering the quasi-static material strength (i.e. von Mises stress [102] or buckling stress [103]). More recently, algorithms also capable to consider the fatigue strength have been proposed [13-24]. For example, in [104] a fatigue driven topology optimisation algorithm where the fatigue constraint is substituted by multiple stress constraints according to traditional high-cycle fatigue design methodology [115] is proposed. Similarly, in [107] the equivalent static stress approach has been employed for the high-cycle fatigue stress assessment considering the Sines method and a modified Goodman criterion. In [44] the dynamic fatigue failure constraints according to Crossland's criterion are included. In [108] a topology optimisation algorithm for finite-life high-cycle fatigue damage using a density approach and analytical gradients is proposed. In [105] random fatigue loads are analysed with different methodologies, such as narrow-band solution, the Wirsching and Light method, the Ortiz and Chen method, and the Dirlik method and taken into account in structural topology optimisation.

It is therefore clear, according to the literature results, that the research of topology optimisation algorithms capable of considering the fatigue constraints is of utmost interest.

However, the fatigue limit inserted as a constraint in topology optimisation algorithms is generally extrapolated by classical fatigue theory (e.g., the asymptote at the end of the S-N curve for steel materials), which is surely effective for a large of real applications but can miss the crucial influence of defects inside the material. Indeed, it is well-known that in many practical applications and in-service conditions, the fatigue response of components is controlled by defects (e.g., inclusions, porosity) which form during the manufacturing process. In this case, the fatigue strength is smaller than the fatigue strength of a component free of defects, according to [116]. Therefore, the topology optimisation algorithm as a design tool must include this defect-driven constrain for the fatigue response in order to avoid premature failures in the optimised components. For example, it is well-known that the fatigue response of additive manufacturing parts is critical and the main reason is the presence of large defects that originates during the production process [117–121]. The influence of defects therefore cannot be neglected to ensure a safe and appropriate design. It must be considered when the component is designed through topology optimisation algorithms, thus permitting to define the topology which ensures the best material exploitation while guaranteeing the structural safety.

The influence of defects on the (lowered) fatigue response was not included in the topology optimisation yet. Interestingly, in [122] the influence of porosity on structural safety is included in the topology optimisation algorithm. However, the parameters related to the porosity size and shape of the holes are not fitted with experimental data and a direct link with the fatigue response of the optimised part is missing. Moreover, the defect size is a priori or randomly assumed and the dependence between the defect size and the material volume is not considered. Furthermore, an arbitrary choice of the defect size could not be effective, since the defect size and its influence on the fatigue response depend on many factors (e.g., the material microstructure) and must be properly assessed for each material. In the following paragraph, the *TopFat* algorithm for considering the influence of defects on the fatigue response is presented. The fatigue limit of the component is assessed by considering the Murakami formulation [116]. In order to take into account, the presence of defects with different morphologies and chemical composition, an equivalent defect size is considered, according to [116]. In order to model the dependence between the defect size and the material volume, the distribution of defects size is assumed to follow the Largest Extreme Values Distribution (LEVD). Indeed, according to [116], the largest defect within the material controls the fatigue response. Therefore, the size of the largest defect, rather than the defect density, controls the fatigue response. For example, the fatigue response of a component with a large number of small defects (higher defect density) is larger than that the fatigue response of a part with a small number of defects, but with larger size. This experimental evidence [116,123] justifies the use of the LEVD for the estimation of the defect size [123]. All the information about the Murakami theory and its application in the *TopFat* algorithm is detailed in the following paragraph. The analytical formulation of *TopFat* is firstly defined, by considering concurrently quasi-static and fatigue

stress constraints, when the component is subjected to load cycles with minimum stress equal to 0 (i.e., stress ratio equal to 0). *TopFat* is finally validated with literature benchmarks, proving its effectiveness and the importance of considering the presence of defects to guarantee the overall structural integrity of the part.

## 4.2 Fatigue response in presence of defects

The influence of small defects on the fatigue response of components has been widely investigated in the literature and the well-known Murakami formulation [116] is generally considered to assess the fatigue strength,  $\bar{\sigma}^f$ , in presence of defects:

$$\bar{\sigma}^f = \frac{C_1 \cdot (HV + 120)}{(\sqrt{a})^{\frac{1}{6}}} \cdot \left( \frac{1 - R}{2} \right)^{0.226 + HV \cdot 10^{-4}} \quad (36)$$

where  $C_1$  is a constant parameter depending on the defect location,  $HV$  is the Vickers hardness of the material accounting for the influence of the microstructure,  $\sqrt{a}$  is the square root of the area of the defect measured in a plane perpendicular to the maximum applied stress and  $R$  is the stress ratio. From a physical point of view, Eq.36 states that the fatigue strength of the material in presence of defects depends on the material hardness, correlated to the microstructure, on the defect size and on the stress ratio. In particular, an increment of the Vickers hardness has a positive effect on the fatigue strength. On the other hand, the larger the defect size, the smaller the fatigue strength. Since different defects (i.e., with different chemical composition and morphology) could form during the manufacturing processes, especially for AM processes, an equivalent defect size can be considered for  $\sqrt{a}$ , according to [116]. Moreover, for  $\sqrt{a}$ , positive stress ratios  $R$  lower the fatigue response. According to [116], Eq.36 is obtained by equating the Stress Intensity Factor (SIF) associated with the defect to the SIF threshold of the material and permits to assess the stress amplitude below which a crack does not propagate from a defect with size equal to  $\sqrt{a}$ . Accordingly, in order to prevent fatigue failures originating from defects, the most critical defect in the component volume should be reliably known. The critical defect corresponds the largest defect present in the material: according to Eq.36, the larger the defect size, the smaller the fatigue limit. Therefore, the largest defect is the “critical defect”. It is clear that the size of the critical defect is not known when a component is designed, since the defect population depends on a large bulk of different factors and mainly on the manufacturing processes. For example, for parts produced through AM processes [117–121], the process parameters strongly affect the defect population.

In order to clarify this aspect, Figure 65 shows the steps that are generally followed for the design of components with topology optimisation algorithms (e.g., AM parts). After setting the design domain and the optimisation parameters, the topology optimisation algorithm provides the topology that minimizes the

compliance under the volume constraint. The component is finally manufactured and, depending on the manufacturing process, it may contain manufacturing defects, highlighted in Figure 65 with yellow circles, which significantly affect the fatigue response. Material defects can be detected with non-destructive techniques: however, the assessment of the defect population once the component has been manufactured prevents any possible modification.

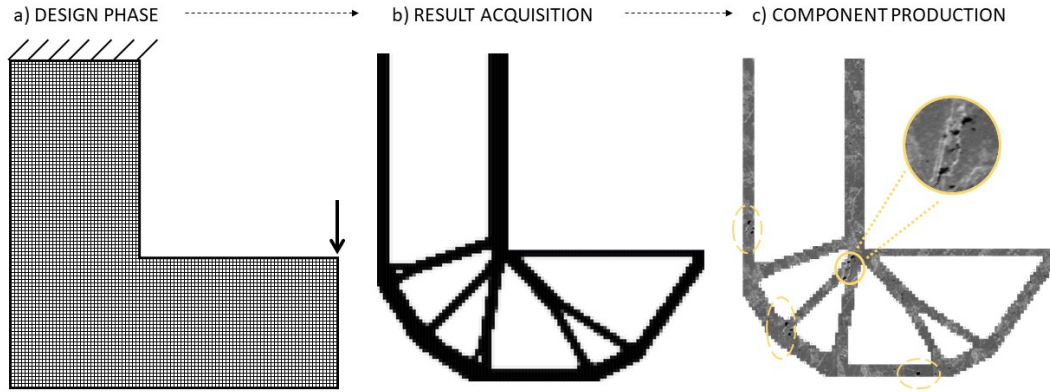


**Figure 65** - Component flow from the initial design domain to the realisation

Therefore, for a proper fatigue design, the possible presence of defects must be taken into consideration when the component is designed. In particular, the defect size distribution in the material and, accordingly, the critical defect size (i.e., the size of the largest defect within the material volume) must be reliably assessed. According to the literature, the defect size is a random variable and is assumed to follow the Largest Extreme Value Distribution (LEVD). The related Cumulative Distribution Function (CDF),  $P_{\sqrt{a}}$ , of the LEVD is given as follows:

$$P_{\sqrt{a}}(\sqrt{a}) = e^{-e^{-\left(\frac{\sqrt{a}-\mu_{\sqrt{a}}}{\sigma_{\sqrt{a}}}\right)}} \quad (37)$$

where  $\mu_{\sqrt{a}}$  and  $\sigma_{\sqrt{a}}$  are the location and the scale parameters of the distribution, respectively. From a physical point of view, Eq.37 permits to compute the probability  $P_{\sqrt{a}}$  of having a defect with size smaller than  $\sqrt{a}$ . The parameters  $\mu_{\sqrt{a}}$  and  $\sigma_{\sqrt{a}}$ , that depends on the material, the production process and on possible post treatment, can be estimated experimentally by assessing the largest defect within samples with a defined volume  $V_0$  (reference volume in the following). Different methodologies are employed in the literature for the parameter estimation, like defect sampling on polished metallurgical samples or by considering the defect originating the fatigue failure in fatigue tests. According to the properties of the LEVD, Eq.37 can be also rewritten to predict the size of the largest defect in a volume  $V_n$   $n$  times  $V_0$ . Indeed, the defect size is dependent on the material volume, i.e., the larger the volume, the larger the probability of defects with larger size. Therefore, the parameters  $\mu_{\sqrt{a}}$  and  $\sigma_{\sqrt{a}}$  estimated for a material volume equal to  $V_0$ , can be used to predict the size of the largest defect within a larger volume  $V_n$ , by exploiting the properties of the LEVD distribution.

The largest defect size,  $\sqrt{a_n}$ , in a material volume  $n$  times  $V_0$  can be obtained through Eq.38 by shifting the original distribution in Eq.37; for more details on the LEVD and on its properties for the assessment of the defects in the material, the reader can refer to [116].

$$\sqrt{a_n} = \mu_{\sqrt{a}} + \sigma_{\sqrt{a}} \cdot (-\ln(-\ln(P)) + \ln(n)) \quad (38)$$

Eq.38 permits to assess the probability of a defect with size  $\sqrt{a_n}$  in a volume  $V_n$  or to assess the  $P$  percentile of the defect size in the volume  $V_n$ .

Therefore, estimated the constant coefficients  $\mu_{\sqrt{a}}$  and  $\sigma_{\sqrt{a}}$  and for a probability  $P$ , the fatigue strength in the component volume  $V_n$  can be reliably predicted by combining Eq.36 and Eq.38:

$$\bar{\sigma}^f = \frac{C_1 \cdot (HV + 120)}{\left( \mu_{\sqrt{a}} + \sigma_{\sqrt{a}} \cdot (-\ln(-\ln(P)) + \ln\left(\frac{V_n}{V_0}\right)) \right)^{\frac{1}{6}}} \cdot \left( \frac{1-R}{2} \right)^{0.226+HV \cdot 10^{-4}} \quad (39)$$

Eq.38 can therefore be used for assessing the fatigue strength in a volume where defects are present and could originate the fatigue cracks. The fatigue strength in Eq.39 can be used as stress limit when components are to be designed. In the proposed methodology, Eq.39 is implemented in a topology optimisation algorithm in order to consider the influence of defects on the fatigue response.

### 4.3 *TopFat* solution

In this paragraph the analytical formulation of the topology optimisation algorithm is provided. Firstly, the optimisation function and the constraints are defined, then the numerical implementation is described. Finally, the solution algorithm is outlined.

#### 4.3.1 Optimisation analytical definition

For the *TopFat* implantation the SIMP approach is employed as already described previously.

Eq.40 shows the proposed topology optimisation formulation, which involves the minimization of the component compliance with defined volume and stress constraints (i.e., von Mises and first principal alternate stress):

$$\begin{aligned}
& \text{find } \boldsymbol{\rho} = \{\rho_1, \rho_2, \dots, \rho_{N_e}\} \\
& \min C = \mathbf{F}^T \mathbf{U}(\boldsymbol{\rho}) = \mathbf{U}(\boldsymbol{\rho})^T \mathbf{K}(\boldsymbol{\rho}) \mathbf{U}(\boldsymbol{\rho}) \\
& \quad \mathbf{K}(\boldsymbol{\rho}) \mathbf{U}(\boldsymbol{\rho}) = \mathbf{F} \\
\text{s. t. } & \left\{ \begin{array}{l} V(\boldsymbol{\rho}) \leq \bar{V} \\ \sigma_e^{\text{vM}}(\boldsymbol{\rho}) \leq \bar{\sigma}^s \quad e = 1, 2, \dots, N_{elem} \\ \sigma_e^1(\boldsymbol{\rho}) \leq \bar{\sigma}^f \quad \text{if } \hat{\sigma}_e^1(\boldsymbol{\rho}) > 0 \quad e = 1, 2, \dots, N_{elem} \\ \underline{\rho} \leq \rho_e \leq 1 \quad e = 1, 2, \dots, N_{elem} \end{array} \right. \quad (40)
\end{aligned}$$

where  $\boldsymbol{\rho} = \rho_e$  ( $e = 1, 2, \dots, N_{elem}$ ) are the design variables, i.e. the densities.  $N_{elem}$  is the total number of elements,  $C$  is the global compliance,  $\mathbf{F}$  is the vector of the global forces,  $\mathbf{U}$  is the vector of the global displacements,  $\mathbf{K}$  is the global stiffness matrix,  $V$  is the volume of the component,  $\bar{V}$  is the upper volume limit,  $\sigma_e^{\text{vM}}$  is the von Mises stress for the  $e^{\text{th}}$  element,  $\bar{\sigma}^s$  is the von Mises upper bound,  $\sigma_e^1$  is the first principal alternate stress for the  $e^{\text{th}}$  element,  $\bar{\sigma}^f$  is the upper limit of the first principal alternate stress defined in Eq.39,  $\hat{\sigma}_e^1$  is the first principal stress for the  $e^{\text{th}}$  element and  $\underline{\rho}$  is the minimum density of the element. The complete expressions of  $\sigma_e^{\text{vM}}$ ,  $\sigma_e^1$  and  $\hat{\sigma}_e^1$  are reported below and properly described. The parameter  $\underline{\rho}$  is usually set in topology optimisation problems in the range [0.0001,0.001], in order to avoid singularities in the global stiffness matrix [42].

The solution that minimizes the compliance under the volume constraint and no other stress or fatigue constraint, provides the optimized material distribution, but stress peaks are likely and are not controlled. This would be detrimental for the structural integrity of the optimized topology and would prevent the use of the topology optimisation algorithm for components. For this reason, the stress constraints are included in the formulation. In particular, the formulation defined in Eq.40 permits to assess the optimized topology for a component subjected to a cyclic force in the range  $[0, F_{max}]$ ,  $F_{max}$  being the maximum applied force in the load cycle, corresponding to a stress ratio  $R$  equal to 0. In order to prevent failures from defects that are randomly distributed within the material volume, the first principal alternate stress in each element is limited by the first principal alternate stress upper limit,  $\bar{\sigma}^f$ , corresponding to the fatigue strength defined in Eq.38. Indeed, the first principal alternate stress is responsible for the crack propagation from defects. However, the first principal alternate stress is always a positive term, but it must be limited only in the elements with a positive first principal stress (i.e., if  $\hat{\sigma}_e^1(\boldsymbol{\rho}) > 0$  in Eq.40), since only positive first principal stresses permit the crack propagation up to failure. For the sake of clarity, only positive  $\hat{\sigma}_e^1$  permits the crack propagation, if a defect is present. On the other hand, if the element is subjected to a compression stress, the crack will not propagate, according to [115,116]. As the volume constraint will be active, the fatigue limit is computed by considering  $V_n = \bar{V}$ . Accordingly, it is conservatively assumed that a defect with the same size of a defect that can be statistically found in a volume corresponding to  $\bar{V}$  is present in each element. In other words, the fatigue

stress constraint is applied to each element, as if the largest defect is found in each element. This assumption is rather conservative, but it permits a rapid convergence of the method. On the other hand, it is worth to note that the fatigue crack does not propagate in regions of material subjected to a compression state during the load cycle. However, if a stress limit is not considered for elements in compression, the optimized component could fail due to possible peak stresses in these elements (e.g., the stress in the element could be larger than the quasi-static strength of the material). For this reason, a second stress constraint is introduced to ensure that the von Mises stress for each element is below an admissible stress (e.g., the yield strength divided by an appropriate safety factor). This second stress constraint is verified for each element: it is worth to note that, for elements subjected to a positive first principal stress and therefore at risk of crack propagation in presence of defects, the most restrictive stress constraint prevails in the optimisation process. This simplifies the numerical implementation of the proposed methodology.

### 4.3.2 Hybrid stress element model

*TopFat* has been numerically implemented for bidimensional cases. In the literature, for bidimensional cases, density-based topology optimisation is commonly carried out using bilinear quadrilateral four-node elements. The main reason lies in the low computational cost of this element model. However, when an explicit stress evaluation is required, these elements may produce inaccurate results due to the shear locking effect, especially in bending dominated regions [61]. To overcome this issue and improve the accuracy of the results, a four-node hybrid stress element model is employed in this study. In this model, both the displacement and stress fields are approximated by means of interpolation functions. The basic idea behind this method is to make the element less sensitive to geometrical distortions and improve therefore the stress accuracy evaluation. This result can be achieved by adding additional nodes too, but this would increase remarkably the computational cost. It has been proved that this method can produce more accurate results, at the same mesh discretization, with respect to classical bilinear quadrilateral four-node elements [124].

All considered, the element stress vector  $\boldsymbol{\sigma}_e$  in the hybrid stress element (Voigt notation) and the SIMP framework is given by:

$$\boldsymbol{\sigma}_e(\boldsymbol{\rho}, \xi, \eta) = [\sigma_{ex} \quad \sigma_{ey} \quad \tau_{exy}]^T = \rho_e^\gamma \boldsymbol{\Phi}(\xi, \eta) \boldsymbol{\beta}_e \quad (41)$$

where  $\sigma_{ex}$ ,  $\sigma_{ey}$  and  $\tau_{exy}$  are the element stress components,  $\gamma$  is a scalar parameter which value depends on the type of stress interpolation employed (detailed in the following paragraph),  $\boldsymbol{\Phi}(\xi, \eta)$  is the geometrical interpolation matrix depending on the element natural coordinates  $\xi$  and  $\eta$ ,  $\boldsymbol{\beta}_e$  is the stress parameter vector. The first term modifies the stress according to the local density dictated by the topology optimisation approach. The second term defines where

the stress is evaluated within the element according to the natural coordinates  $\xi$  and  $\eta$ . The third term  $\boldsymbol{\beta}_e$  relates the displacement fields with the stress considering the material elasticity, the strain-displacement matrix, and the structure thickness, similarly to the classical finite element model. The analytical derivation of Eq.41 the term  $\boldsymbol{\beta}_e$  starts from Eq.42 where the displacement element vector expression is reported.

$$\mathbf{u}_e(\xi, \eta) = [u_{ex} \quad u_{ey}]^T = \mathbf{N}(\xi, \eta) \mathbf{d}_e \quad (42)$$

Where  $u_{ex}$  and  $u_{ey}$  are the element displacement components, and  $\mathbf{N}(\xi, \eta)$  are the geometrical interpolation matrices depending on the element natural coordinates  $\xi$  and  $\eta$  for the stress and displacement respectively, and  $\mathbf{d}_e$  is the element nodal displacement. As for the displacement field, the same interpolation scheme of bilinear quadrilateral four-node elements is used. As for the stress field, following [124] it is possible to express the stress parameter vector  $\boldsymbol{\beta}_e$  as:

$$\boldsymbol{\beta}_e = \mathbf{H}^{-1} \mathbf{G} \mathbf{d}_e \quad (43)$$

where the two matrices read:

$$\mathbf{G} = \int_{-1}^1 \int_{-1}^1 \boldsymbol{\Phi}^T \mathbf{B} t_0 |\mathbf{J}| d\xi d\eta \quad (44)$$

$$\mathbf{H} = \int_{-1}^1 \int_{-1}^1 \boldsymbol{\Phi}^T \mathbf{S}_0 \boldsymbol{\Phi} t_0 |\mathbf{J}| d\xi d\eta \quad (45)$$

The terms reported in Eq.44 and Eq.45 are:  $\mathbf{J}$  the Jacobian matrix and  $|\mathbf{J}|$  its determinant,  $\mathbf{B}$  the strain-displacement matrix,  $\mathbf{S}_0$  the compliance matrix, i.e. the inverse of the elasticity matrix, and  $t_0$  the structure thickness. Overall, the element stiffness matrix  $\mathbf{k}_e$  and the element vector stress  $\boldsymbol{\sigma}_e$  respectively read:

$$\mathbf{k}_e = \mathbf{G}^T \mathbf{H}^{-1} \mathbf{G} \quad (47)$$

$$\boldsymbol{\sigma}_e = \boldsymbol{\Phi} \mathbf{H}^{-1} \mathbf{G} \mathbf{d}_e \quad (48)$$

Thanks to Hellinger-Reissner variational principle [61,124] it is possible to find out the dependency with the density design variable  $\rho$ . The above-described matrixes in the SIMP framework read:

$$\boldsymbol{\beta}_e = \rho_e^\gamma \mathbf{H}^{-1} \mathbf{G} \mathbf{d}_e \quad (49)$$

$$\mathbf{k}_e = \rho_e^\gamma \mathbf{G}^T \mathbf{H}^{-1} \mathbf{G} \quad (50)$$

$$\boldsymbol{\sigma}_e = \rho_e^\gamma \boldsymbol{\Phi} \mathbf{H}^{-1} \mathbf{G} \mathbf{d}_e \quad (51)$$

In all the further analysis, it has been chosen to evaluate the stress element vector  $\boldsymbol{\sigma}_e$  in the element centre, i.e.  $\boldsymbol{\Phi}(0,0)$ , according to [61]. In order to simplify the notation, the stress element vector evaluated in the element centre  $\boldsymbol{\sigma}_e(\boldsymbol{\rho}, 0,0)$  is renamed as  $\boldsymbol{\sigma}_{ce}(\boldsymbol{\rho})$  in the following.

### 4.3.3 Stress constraints implantation

When the stress constraint is considered in the topology optimisation problem formulation, some issues must be managed in order to obtain a clear convergence and a correct final topology. Firstly, the stress constraint is for its own nature a local constraint and during the optimisation it is likely to be discontinue within the domain, leading to singular optimum. This problem is so-called *stress singularity* and it belongs to the set of singularity problems in structural optimisation, well-known and widely described in the literature from many decades [125].

In this study, the stress singularity is avoided through the *qp-relaxation strategy* [126], which uses two different penalization factors for the stiffness and the stress. This strategy consists of penalizing the element stiffness in Eq.6 with the parameter  $p$  while the stress in Eq.41 is penalized with another exponent,  $q$ . Therefore, the discontinuity in the constraints is smoothed by relaxing the penalization applied to the stress measure. Namely, the predefined parameter  $\gamma$  in Eq.41 is equal to  $q$ , whose value has been set equal to 0.5 as done in [61]. Some other relaxation approaches are also available in the literature: e.g., the  $\varepsilon$ -relaxation method [127] or the *stress penalization* method [128]. However, it has been decided to employ the *qp-relaxation strategy* since it has been found to be one of the most effective and straightforward technique to solve the stress singularity [61].

Given the element stress vector properly penalised and evaluated in the element centre  $\boldsymbol{\sigma}_{ce}(\boldsymbol{\rho})$ , it is possible to calculate the von Mises and first principal alternate stress. In particular, the von Mises stress for the  $e^{\text{th}}$  element can be evaluated as follows:

$$\sigma_e^{\text{vM}}(\boldsymbol{\rho}) = (\boldsymbol{\sigma}_{ce}^T \mathbf{V} \boldsymbol{\sigma}_{ce})^{\frac{1}{2}} \quad (42)$$

where:

$$\mathbf{V} = \begin{bmatrix} 1 & -1/2 & 0 \\ -1/2 & 1 & 0 \\ 0 & 0 & 3 \end{bmatrix} \quad (43)$$

The first principal alternate stress, under the plane stress hypothesis for bidimensional structure, is, in matrix notation:

$$\sigma_{ce}^1 = \boldsymbol{\sigma}_{ce}^T \mathbf{V}_1 + \frac{1}{2} (\boldsymbol{\sigma}_{ce}^T \mathbf{V}_2 \boldsymbol{\sigma}_{ce})^{\frac{1}{2}} \quad (44)$$

where the two matrices are respectively:

$$\mathbf{V}_1 = \begin{bmatrix} 1 & 1 & 0 \\ 2 & 2 & 0 \end{bmatrix}^T, \quad \mathbf{V}_2 = \begin{bmatrix} 1 & -1 & 0 \\ -1 & 1 & 0 \\ 0 & 0 & 4 \end{bmatrix} \quad (45)$$

In the analysed optimisation problem, where the stress ratio  $R$  is set equal to zero, the value of  $\hat{\sigma}_e^1$  is simply twice the alternate stress  $\sigma_e^1$ . A second problem related to stress constrained topology optimisation comes into account when looking at the number of equations involved. Indeed, if the domain is discretised by a large number,  $n$ , of elements, the stress constraint must be checked for each element, leading possibly to  $2n$  constraints,  $n$  for each stress constraint. In this case, aggregation functions are used to reduce the number of constraints to a single value and improve the computational efficiency of the topology optimisation. The most employed are the  $P$ -norm aggregation function [129] and the *Kreisselmeier-Steinhauser (KS)* aggregation function [102,130–132]. In the presented study the K-S function is employed for both the constraints on von Mises stress and the first principal alternate stress. The aggregation functions are evaluated following Eq.46 and Eq.47 within the domain  $\Omega$  and the subdomain  $\Omega^1$  respectively. This last sub domain is defined as the portion of the domain where the elements undergo traction stress, i.e. the first principal stress is positive as already stated in Eq.40. It can be defined analytically as  $\Omega^1 = \{e \in \Omega \mid \hat{\sigma}_e^1(\boldsymbol{\rho}) \geq 0\}$ .

$$\sigma^{vM, KS} = \frac{1}{\mu_\sigma} \ln \left[ \sum_{e \in \Omega} \exp \left( \frac{\mu_\sigma \sigma_e^{vM}}{\bar{\sigma}^s} \right) \right] \quad (46)$$

$$\sigma^{1, KS} = \frac{1}{\mu_\sigma} \ln \left[ \sum_{e \in \Omega^1} \exp \left( \frac{\mu_\sigma \sigma_e^1}{\bar{\sigma}^f} \right) \right] \quad (47)$$

where  $\mu_\sigma$  is the stress aggregation parameter and it controls the approximation of  $\max(\sigma_e^{vM})$  and  $\max(\sigma_e^1)$  which are the parameters to be effectively constrained. For lower values of  $\mu_\sigma$ , the approximation is poor and the final mismatch between the real maximum and that evaluated through the aggregation function raises. For higher values, the accuracy increases but the induced non-linearity in the problem also rises. It must be balanced properly to achieve the best compromise. A more detailed discussion about this term and the K-S aggregation function is provided in [133].

Whereas the aggregation functions solve the high number of constrain problems, they induce approximations and higher non-linearities in the topology

optimisation problems. These K-S related issues can be overcome by means of the *STM (stability transformation method)-based* stress correction scheme [134]. In all non-trivial cases, the approximations induced by the K-S aggregation function overestimates the actual maximum of element stress. Therefore, two stress constraint functions,  $f^{vM}$  and  $f^1$ , are computed by scaling down the term  $\sigma^{vM, KS}$  and  $\sigma^{1, KS}$ , according to the STM-based stress correction scheme which reads:

$$f^{vM} = c_s^{I, vM} \cdot \sigma^{vM, KS} \leq \bar{\sigma}^s \quad (48)$$

$$f^1 = c_s^{I, 1} \cdot \sigma^{1, KS} \leq \bar{\sigma}^s \quad (49)$$

The complete expressions of the correction factors in the STM-based stress correction scheme  $c_s^{I, vM}$  and  $c_s^{I, 1}$  are reported as below:

$$c_s^{I, vM} = \begin{cases} \alpha_s^{I, vM} & I = 1 \\ (1 - s_0)\alpha_s^{I, vM} + s_0 c_s^{I-1, vM} & I > 1 \end{cases} \quad (50)$$

$$c_s^{I, 1} = \begin{cases} \alpha_s^{I, 1} & I = 1 \\ (1 - s_0)\alpha_s^{I, 1} + s_0 c_s^{I-1, 1} & I > 1 \end{cases} \quad (51)$$

where  $I$  is the iteration index of the topology optimization procedure,  $\alpha_s^{I, vM} = \frac{\max(\sigma_e^{vM})_I}{\sigma^{vM, KS}}$ ,  $\alpha_s^{I, 1} = \frac{\max(\sigma_e^1)_I}{\sigma^{1, KS}}$  and  $s_0 \in [0,1]$  is a relaxation parameter for avoiding possible oscillations. From the whole set of possible methodologies to solve the stress constraint related issues, the *qp-relaxation* strategy, the *K-S aggregation* function, and the *STM-based correction* scheme have been selected. This choice is justified by previous studies [61,103] which proved the effectiveness of the presented solution.

Finally, the Method of Moving Asymptotes (MMA) [25] has been adopted to numerically solve the optimisation problem. This method is a first order-programming solver, and it requires the evaluation of the first derivatives.

Here, the sensitivity analysis of the first principal alternate stress is detailed. For the sensitivity of the compliance, the volume constraint and the von Mises constraint the reader is referred to [61] since they have been already established.

The derivatives of the first principal alternate stress of the  $e^{\text{th}}$  element  $\sigma_e^1$ , defined in Eq.44, with respect to the stress components  $\sigma_{ex}$ ,  $\sigma_{ey}$ ,  $\tau_{exy}$ , defined in Eq.41, are given by:

$$\begin{aligned}
\frac{\partial \sigma_e^1}{\partial \sigma_{ex}} &= \frac{1}{2} + \frac{1}{2} \frac{\sigma_{ex} - \sigma_{ey}}{\sqrt{(\sigma_{ex} - \sigma_{ey})^2 + 4\tau_{exy}^2}} \\
\frac{\partial \sigma_e^1}{\partial \sigma_{ey}} &= \frac{1}{2} - \frac{1}{2} \frac{\sigma_{ex} - \sigma_{ey}}{\sqrt{(\sigma_{ex} - \sigma_{ey})^2 + 4\tau_{exy}^2}} \\
\frac{\partial \sigma_e^1}{\partial \tau_{exy}} &= \frac{2\tau_{exy}}{\sqrt{(\sigma_{ex} - \sigma_{ey})^2 + 4\tau_{exy}^2}}
\end{aligned} \tag{52}$$

In matrix form the derivatives can be expressed as:

$$\frac{\partial \sigma_e^1}{\partial \boldsymbol{\sigma}_e} = \mathbf{V}_1^T + \frac{1}{2} \frac{\mathbf{V}_2 \boldsymbol{\sigma}_e}{(\boldsymbol{\sigma}_e^T \mathbf{V}_2 \boldsymbol{\sigma}_e)^{\frac{1}{2}}} \tag{53}$$

The sensitivity of the K-S stress function in Eq.47 with respect to  $\rho_i$  can be derived using the chain rule as:

$$\frac{\partial \sigma^{1,KS}}{\partial \rho_i} = \sum_{e \in \Omega^1} \frac{\partial \sigma^{1,KS}}{\partial \sigma_e^1} \left( \frac{\partial \sigma_e^1}{\partial \boldsymbol{\sigma}_{ce}} \right)^T \frac{\partial \boldsymbol{\sigma}_{ce}}{\partial \rho_i} \tag{54}$$

In the above expression, the partial derivative of the K-S stress function with respect to the element first principal alternate stress is detailed as below:

$$\frac{\partial \sigma^{1,KS}}{\partial \sigma_e^1} = \frac{1}{\sigma_f} \cdot \frac{\exp\left(\mu_\sigma \frac{\sigma_e^1}{\sigma_f}\right)}{\sum_{e \in \Omega^1} \exp\left(\mu_\sigma \frac{\sigma_e^1}{\sigma_f}\right)} \tag{55}$$

The sensitivity of the element stress vector with respect to  $\rho_i$  is:

$$\frac{\partial \boldsymbol{\sigma}_{ce}}{\partial \rho_i} = \frac{q}{\rho_e} \delta_{ie} \boldsymbol{\sigma}_{ce} + \rho_e^q \boldsymbol{\Phi}_c \mathbf{H}^{-1} \mathbf{G} \frac{\partial \mathbf{d}_e}{\partial \rho_i} \tag{56}$$

where  $\delta_{ie}$  is the Kronecker delta. The adjoint method [102,134] is used to calculate the last term on the right-hand-side of Eq.56, which contains the sensitivity of the displacement vector. Following the same procedure as in [104] and after some rearrangements of the mathematical terms, it is possible to derive the expression for the sensitivity:

$$\frac{\partial \sigma^{1,KS}}{\partial \rho_i} = \sum_{e \in \Omega^1} \frac{q \delta_{ie}}{\rho_e} \frac{\partial \sigma^{1,KS}}{\partial \sigma_e^1} \left( \frac{\partial \sigma_e^1}{\partial \boldsymbol{\sigma}_{ce}} \right)^T \boldsymbol{\sigma}_{ce} - (\boldsymbol{\chi}^{1,KS})^T \frac{\partial \mathbf{K}}{\partial \rho_i} \mathbf{U} \tag{57}$$

where  $\boldsymbol{\chi}_k^{\text{KS}}$  is an adjoint vector that can be obtained by solving the following:

$$\mathbf{K}\chi_k^{KS} = \sum_{e \in \Omega^1} \rho_e^q \frac{\partial \sigma_k^{KS}}{\partial \sigma_e^1} (\Phi_c \mathbf{H}^{-1} \mathbf{G})^T \frac{\partial \sigma_e^1}{\partial \sigma_{ce}} \quad (58)$$

The derivatives of all the quantities can be achieved by the chain rule if the projected and filtered density is considered as reported in [61].

#### 4.3.4 Solution algorithm

To check the convergence of the MMA, the following two criteria have been used:

$$\begin{aligned} \|\boldsymbol{\rho}^{(I)} - \boldsymbol{\rho}^{(I-1)}\|_{\infty} &\leq \varepsilon_{\rho} \\ \frac{\|\mathbf{C}^{(I)} - \mathbf{C}^{(I-1)}\|}{\mathbf{C}^{(I)}} &\leq \varepsilon_{\mathbf{C}} \end{aligned} \quad (59)$$

where  $I$  is the iteration index, and  $\varepsilon_{\mathbf{C}}$  and  $\varepsilon_{\rho}$  are predefined tolerances [61].

The flowchart of the proposed solution algorithm *TopFat* is reported in Figure 66, the numbers indicate the various steps of the method. It can be split into two main different phases. The first phase (1) consists of the evaluation of the defect population and related stress limit according to Murakami theory. Then the second phase (2), where the proper topology optimisation is carried out considering the defect distribution. The defect population analysis in *TopFat* starts with the optimisation model definition (1.1), i.e. the design domain, the application of the boundary conditions and the material model. In this step, the solution parameters are defined too. Step 1.2 consists of the defect population estimation according to LEVD, the evaluation of the size  $\sqrt{a}$  of the most critical one. In step 1.3 the information about the defect population is converted in the admissible first principal alternate stress following the Murakami theory. After that, the topology optimisation phase starts, and it begins with the filtering and the projection of the density variables (2.1). Step 2.2 consists of the finite element analysis and therefore the evaluation of the compliance, the volume, and the stress functions within the domain. The sensitivity of these quantities with respect to the density variables follows (2.3). The updating of the new distribution of the density variables by means of the MMA method is carried out in step 2.4. Finally, in step 2.5 the convergence is checked, and step 2.1-2.4 are repeated in case it is not verified.

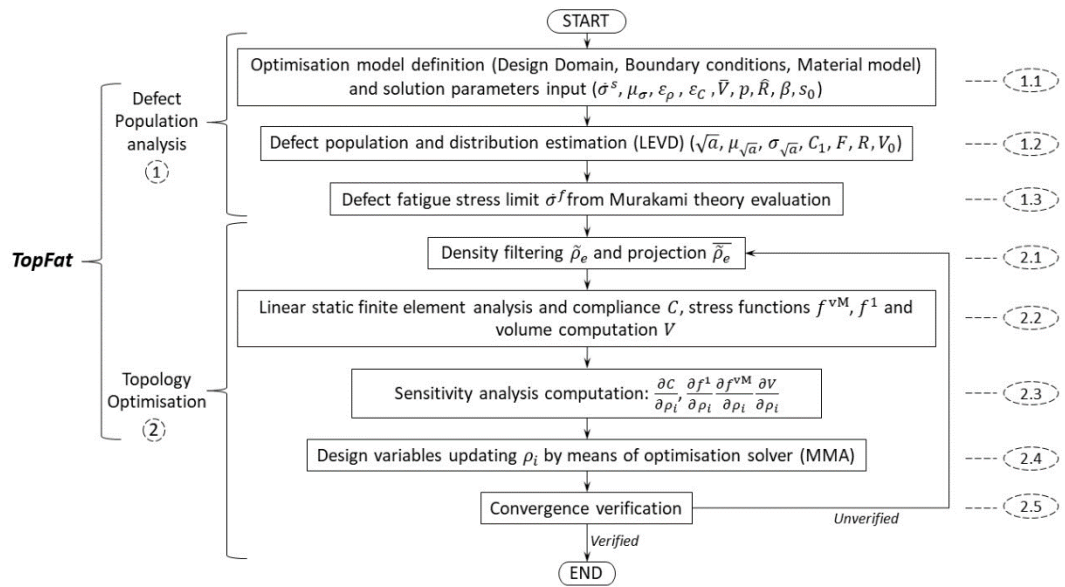


Figure 66 - Flowchart of the *TopFat* solution algorithm

## 4.4 *TopFat* results

In this paragraph, *TopFat* is validated on literature benchmarks. Below, the optimized topology of an L-shape structure, a cantilever and a corbel structure are assessed, respectively. For all the examples, steel is considered as constituent material, with Young's modulus  $E = 2.1 \times 10^5$  MPa and Poisson's ratio  $\nu = 0.3$ , respectively. Initial designs with a uniform material distribution have been considered and all the initial values of the densities are set equal to 0.3. In Table 7 the values of the optimisation parameters are detailed.

SIMP parameter	Value and/or continuation scheme
Material interpolation $p$	$p = \min\{1 + \text{floor}((I - 1)/3) \cdot 0.1, 3\}$
Stress aggregation measure $\mu_\sigma$	$\mu_\sigma = 10$
Relaxation parameter $s_0$	$s_0 = 0.618$
Linear filter radius $\hat{R}$	$\hat{R}/l_e = \max\{R_0 - \text{floor}((I - 1)/10) \cdot 0.1, R_{min}\}$ $R_0 = 4; R_{min} = 1.2$
Nonlinear projection $\beta$	$\beta = \begin{cases} 0.1 & \text{if } I < 400 \\ \min\{0.1 + \text{floor}((I/10 - 40)), 20\} & \text{if } I \geq 400 \end{cases}$
Convergence tolerance parameters $\varepsilon_C, \varepsilon_\rho$	$\varepsilon_C = 0.01; \varepsilon_\rho = 0.01$

Table 7 - Values of *TopFat* optimisation parameters

Table 8 lists the parameters related to the defect distribution and fatigue strength [116].  $C_1$  has been set conservatively to 1.41 (worst condition in [116]).

A Vickers hardness of 290 HV, consistent with the employed material, has been considered. The stress ratio  $R$  is set equal to 0. The volume  $V_n$  for each case is conservatively set equal to  $\bar{V}$ , the volume of the final topology, supposing that all the elements could contain the most critical defect. The reference volume for the LEVD is equal to  $8.8 \times 10^{-3} \text{ mm}^3$ , which is reasonably the inspection volume for defect sampling on the metallographic polished sample with an inspection area of about  $0.5 \text{ mm}^2$  [116]. The probability  $P$  has been set to 0.5 (i.e., the median quantile of the defect size in the final volume was considered). It is worth to note that a more conservative quantile can be chosen. However, since other conservative assumptions were made for the validation benchmarks (i.e., fatigue limit for surface defects and the presence of the critical defect in each element), the choice of the median quantile was considered appropriate. In addition, reasonable values from the literature have been considered or have been assumed, in order to show the effectiveness of the proposed methodology and the need of considering the material sensitivity to defect in the topology optimisation process.

Fatigue parameter	Value
Defect location parameters $C_1$	$C_1 = 1.41$
Vickers hardness $HV$	$HV = 290$
LEVD location parameter $\mu_{\sqrt{a}}$ [ $\mu\text{m}$ ]	$\mu_{\sqrt{a}} = 16.96$
LEVD scale location parameter $\sigma_{\sqrt{a}}$ [ $\mu\text{m}$ ]	$\sigma_{\sqrt{a}} = 2.389$
Probability $P$	$P = 0.5$
Stress ratio $R$	$R = 0$
Reference volume $V_0$ [ $\text{mm}^3$ ]	$V_0 = 8.8 \cdot 10^{-3}$
Initial volume $V_s$ [ $\text{mm}^3$ ]	$V_s^{L\text{-shape}} = 6400$
	$V_s^{\text{cantilever}} = 20000$
	$V_s^{\text{corbel}} = 17700$
Upper limit volume, $\bar{V}$	$\bar{V} = 0.3 \cdot V_s$

**Table 8** - Values of defect and fatigue parameters

#### 4.4.1 L-shape structure design

In the first example, the optimized material distribution within a classical L-shape structure, shown in Figure 67, is assessed. This domain geometry has been fairly employed in the literature and it is largely used for testing the effectiveness of stress-constrained topology optimisation algorithms [132][102]. The material volume is constrained to 30% of the design domain volume (i.e.,  $\bar{V} = 0.3 \cdot \bar{V}_{\text{L-shape}}$ ). The design domain is discretized into 6400 square four-node elements with the edge length 1 mm. To avoid the artificial stress concentration, the concentrated load  $F = 800 \text{ N}$  is distributed equally over the closest five nodes around the vertical-right corner. The fatigue strength of the material computed

according to Eq.39 by considering a volume corresponding to  $0.3 \cdot \bar{V}_{L\text{-shape}}$ , leads to a limit of the first principal alternate stress of  $\bar{\sigma}^f = 255 \text{ MPa}$ . For the von Mises stress constraint, an admissible stress  $\bar{\sigma}^s = 580 \text{ MPa}$  is considered (e.g., yield strength divided by an opportune safety coefficient).

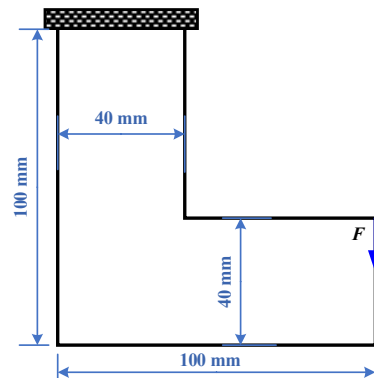


**Figure 67** - L-shape design domain and geometrical dimensions.

The optimized topologies of the L-shape domain are obtained by considering four different constraint conditions Figure 68. Figure 68a shows the optimized topology with only the volume constraint, Figure 68b shows the optimized topology with the volume and the von Mises constraint, Figure 68c shows the optimized topology with the volume and the fatigue constraint on the first principal alternate stress and Figure 68d shows the optimized topology with all the constraints. In the figure,  $C$  is the compliance,  $\sigma_{\max}^{\text{VM}}$  is the maximum von Mises stress,  $\sigma_{\max}^1 = \max(\sigma_e^1)$  is the maximum first principal alternate stress within the final domain.

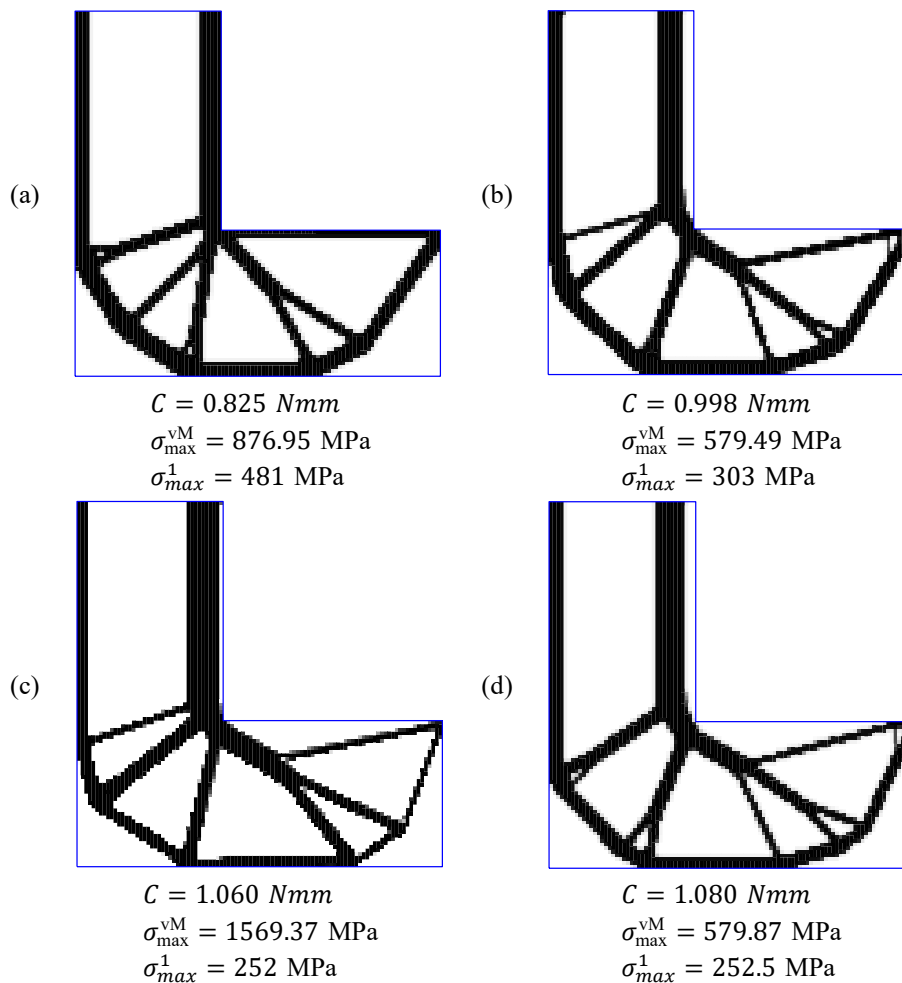


**Figure 68** - Optimisation results for the L-shape structure

As shown in Figure 68 the solution to the classical compliance minimization problem under volume constraint (Figure 68a) provides the minimum compliance compared to the other topologies. This represents the topology with the highest stiffness ( $C$  is the smallest), but both the von Mises stress and the first principal alternate stress are significantly larger than the material limits, compromising the structural integrity. Indeed, the re-entrant corner is still present in the design obtained, even if it is the most critical part of the entire domain since it is characterised by high and detrimental stress peaks. If the von Mises stress constraint is added (Figure 68b), the final topology changes and the corner is smoothed, with the von Mises stress below the limit but the first principal alternate stress above the fatigue strength. The compliance, on the contrary, increases by about 20%. The topology in Figure 68c, obtained by considering the constraints on the first principal alternate stress (fatigue constraint) and on the volume, is quite similar to the one showed in Figure 68b. However, the members close to the corner are thicker, and thinner far from it, ensuring a first principal alternate stress below the prescribed fatigue strength, but with the von Mises stress significantly larger than the limit. In these three cases (Figure 68a-c), therefore, the structural integrity of the component is not guaranteed. Finally, Figure 68d shows the topology of the fully constrained problem, i.e. under all the

constraints on volume, von Mises and first principal alternate stress. It is useful to see these final topologies as an assembly of trusses. Indeed, the comparison of the thickness, location, and orientation of these trusses in the final topologies can foster the understanding of their differences and peculiarities. The topology shown in Figure 68d is qualitatively similar to those shown in Figure 68b and Figure 68c, but the trusses dimensions are significantly different. In this case, both the maximum von Mises stress and the first principal alternate stress are below the limits, ensuring the structural integrity of the component. The compliance increment, about 29%, is compensated by a significant reduction in the stress level to completely satisfy the structural requirements, which is the most important aspect when a component is designed. Figure 69 shows stress distributions in the topology obtained by considering all the constraints (Figure 68d): Figure 69a shows the first principal alternate stress, whereas Figure 69b shows the von Mises stress.

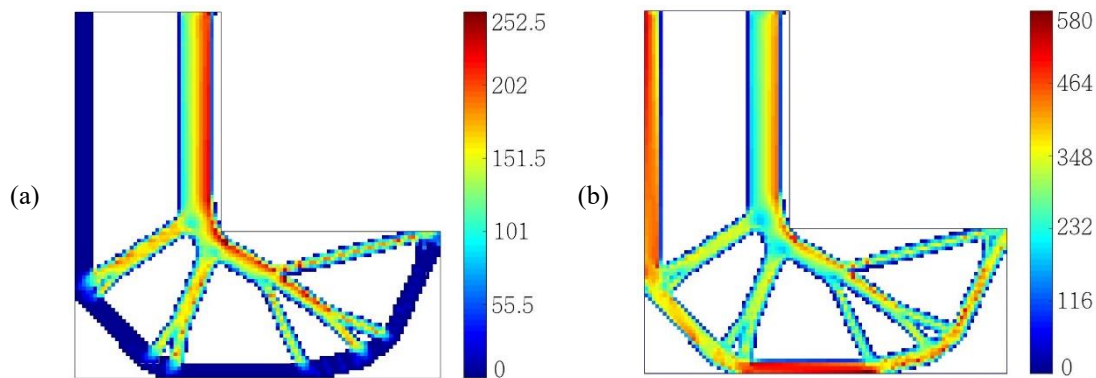


**Figure 69** - Stress distribution of the optimized L-shape

As shown in Figure 69a, the first principal alternate stress in the lower trusses is close to 0 (blue colour), while it is close to the fatigue strength along the trusses close to the corner. For this reason, the lower trusses are thinner compared to the trusses close to the corner. The peak of the von Mises stress (Figure 69b), on the contrary, is in the lower truss of the optimized domain. Figure 69 confirms that both the stress constraints in the presented topology are respected.

Figure 70a and Figure 70b show the trend of the most meaningful quantities during the optimisation process. In particular, Figure 70a shows the compliance and the stress with respect to the number of iterations (the compliance, the K-S fatigue function and the first principal alternate stress are shown); whereas Figure 70b shows the material volume ratio and the stress with respect to the number of iterations (the K-S stress function and the maximum von Mises stress). As it can be noticed, the K-S aggregation function overestimates the real maximum in the structure. This is the reason why the STM-correction scheme is needed, as explained in previously. Overall, the combination of the aggregation function and the correction scheme reduces the number of constraints but guarantees that the real maximum value is set to the imposed limit.

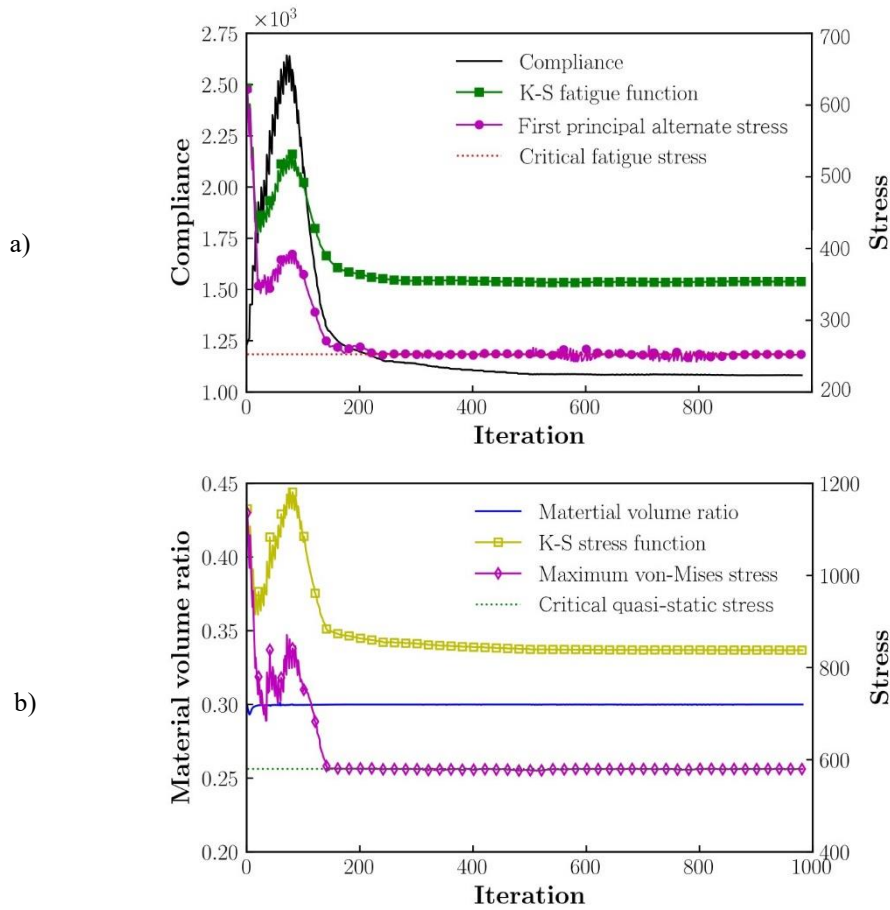


**Figure 70** - Iteration histories for optimisation of the L-shape

As shown in Figure 70a, the K-S fatigue function, the first principal alternate stress and the compliance share almost the same trend. A maximum appears around iteration number 100 and then these quantities rapidly decrease to their prescribed convergence values with few slight oscillations. The same considerations can be done for the von Mises stress and its K-S aggregation function (Figure 70b). As for the volume ratio, it is almost constant during the process, mainly because the initial values of the design variables are set to the selected volume fraction, speeding up the convergence process of the volume constraint. Figure 70 confirms therefore that the proposed algorithm rapidly converges to the prescribed values.

#### 4.4.2 Cantilever structure design

A modified cantilever structure, shown in Figure 71, is also considered for the validation of the proposed topology optimisation model and solution algorithm. As for the other examples, the prescribed material volume fraction is 0.30. The design domain is divided into 20,000 square four-node elements with of unit edge length. A concentrated load of  $F = 1.0$  kN is distributed over thirteen neighbouring nodes along the right edge to avoid stress concentration. The fatigue strength  $\bar{\sigma}^f$ , computed according to Eq.39, is equal to 253 MPa. As for the von Mises stress constraint, in this case it is set to  $\bar{\sigma}^s = 620$  MPa.

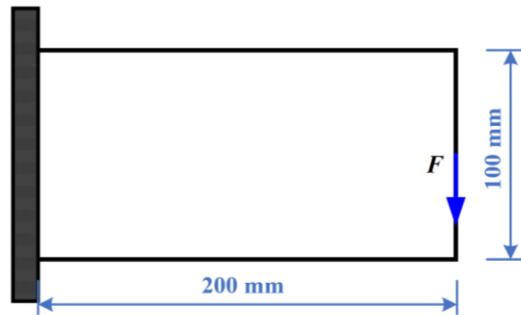


**Figure 71** - Cantilever design domain and geometrical dimensions

As for the first example, four topology optimisations with different constraints are carried out and the designs obtained are presented in **Errore. L'origine riferimento non è stata trovata.** **a** shows the optimized topology with only the volume constraint, **Errore. L'origine riferimento non è stata trovata.** **b** shows the optimized topology with the volume and the von Mises stress constraints, **Errore. L'origine riferimento non è stata trovata.** **c** shows the optimized topology with the volume constraint and the fatigue constraint on the first principal alternate stress and **Errore. L'origine riferimento non è stata trovata.** **d** shows the optimized topology with all the constraints.

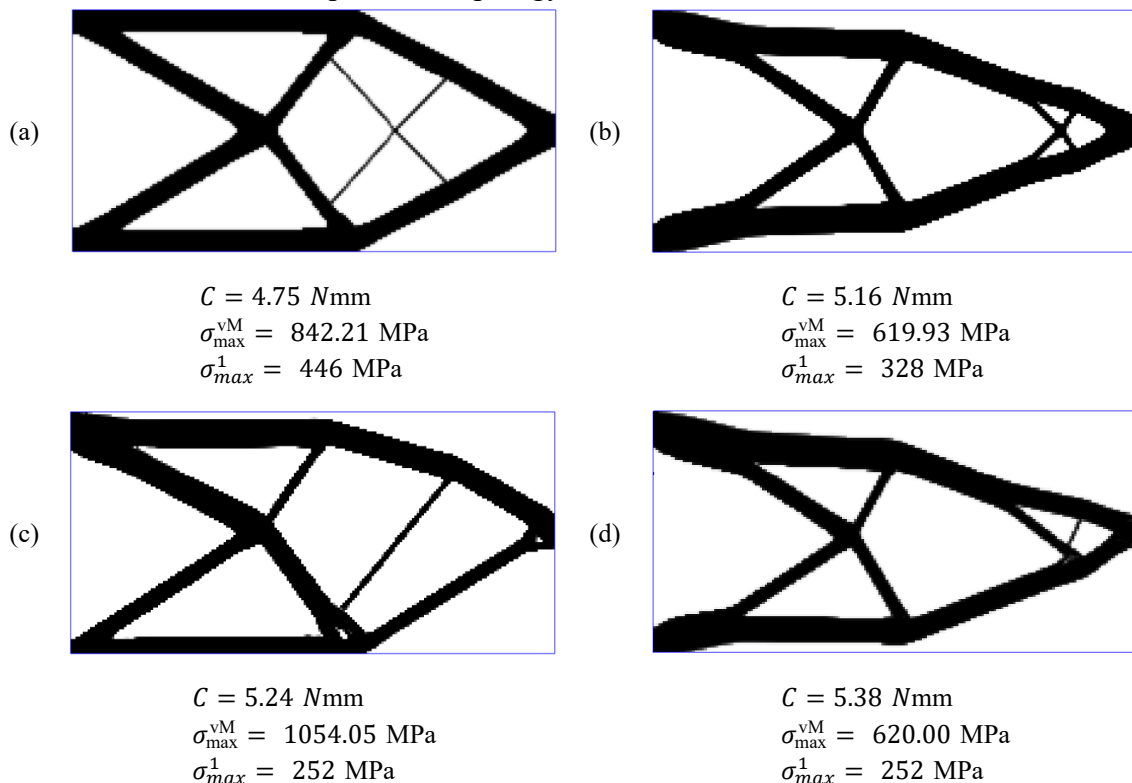


**Figure 72** - Optimisation results for the cantilever beam

According to **Errore. L'origine riferimento non è stata trovata.**, similar observations as for the L-shape structure can be made. The topology obtained by considering only the volume constraint is characterized by the maximum stiffness, but both the stresses (first principal alternate and von Mises) are larger than the

admissible stresses. On the other hand, by considering only a limit on the von Mises stress (**Errore. L'origine riferimento non è stata trovata.b**) and a limit on the first principal alternate stress (**Errore. L'origine riferimento non è stata trovata.c**), one of the two stress constraints is violated. The fourth topology where both stress constraints are active (**Errore. L'origine riferimento non è stata trovata.d**) permits to respect both the material limits, with a compliance increment of about 13%, smaller than the increment in the L-shape structure.

Figure 73 shows the stress distribution in the topology obtained by considering all the constraints (**Errore. L'origine riferimento non è stata trovata.d**): Figure 73a shows the first principal alternate stress, whereas Figure 73b shows the von Mises stress.

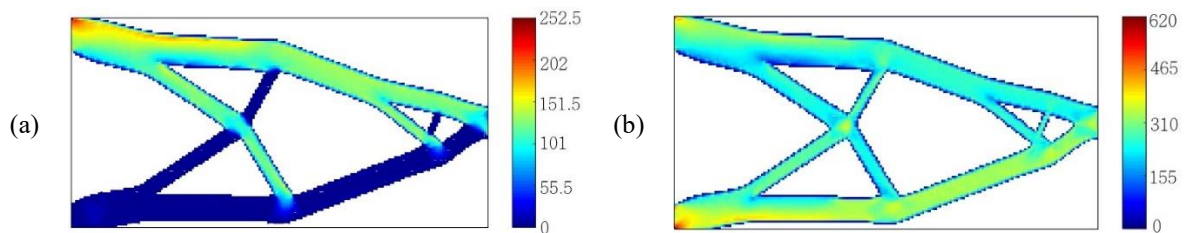


**Figure 73** - Stress distribution of the optimized cantilever beam

By analysing Figure 73a and Figure 73b, the asymmetry induced by the fatigue constraint could be explained. Indeed, according to **Errore. L'origine riferimento non è stata trovata.a** and **Errore. L'origine riferimento non è stata trovata.b**, the final topology is vertically symmetric if constraints on the first principal alternate stress are not applied. On the contrary, the topologies in **Errore. L'origine riferimento non è stata trovata.c** and **Errore. L'origine riferimento non è stata trovata.d**, obtained by applying constraints on the first principal alternate stress, are not symmetric. Indeed, the von Mises stress is higher in the compressed trusses, whereas the first principal alternate stress prevails in the trusses subjected to traction, forcing them to be thicker and inducing a non-symmetric topology.

Figure 74a and Figure 74b show the trend of the most meaningful quantities during the optimisation process. In particular, Figure 74a shows the compliance and the stress with respect to the number of iterations (the compliance, the K-S fatigue function and the first principal alternate stress are shown); whereas Figure 74b shows the material volume ratio and the stress with respect to the number of iterations (the K-S stress function and the maximum von Mises stress).

The trends highlighted in Figure 74a and Figure 74b show that feasible designs are achieved in about 600 iterations and the convergence process is effective, with very little fluctuations. This means, as for the L-shape, that the proposed algorithm provides a smooth and clear method to find the optimal topology.

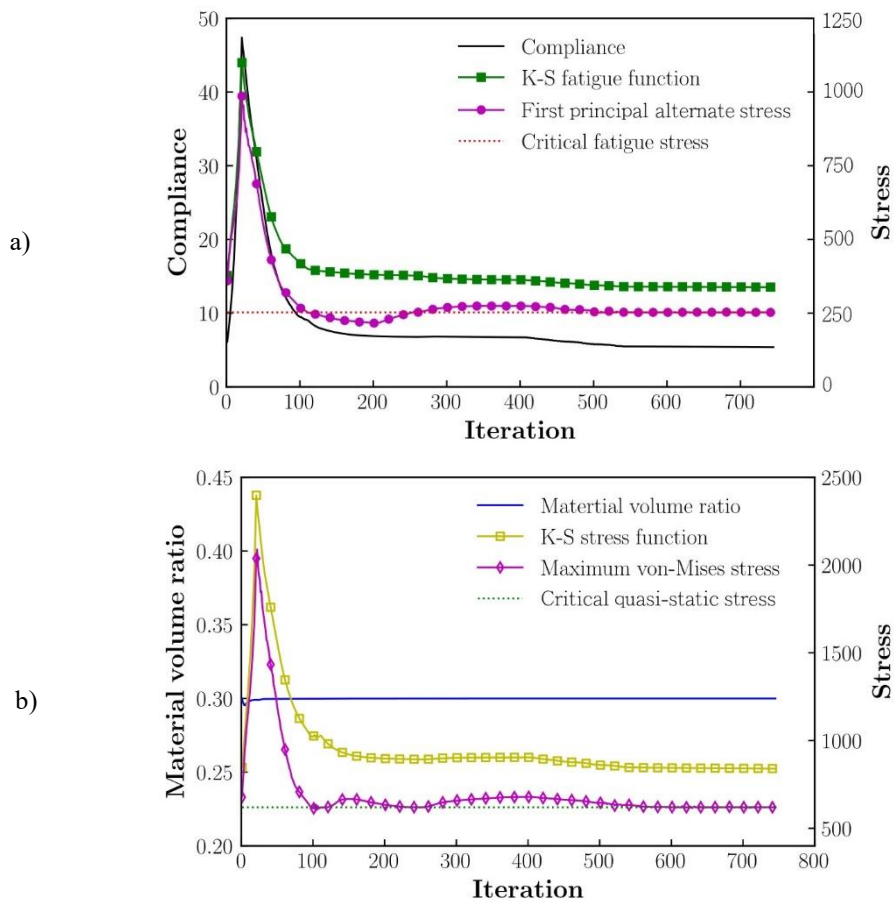
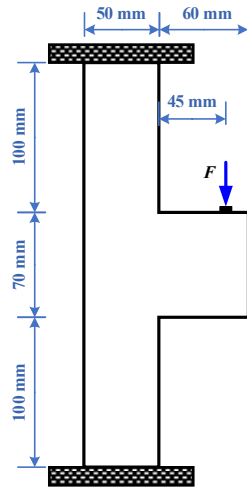


Figure 74 - Iteration histories for optimisation of the cantilever beam

### 4.4.3 Corbel structure design

In the third example, a corbel structure [131] is considered (Figure 75). The prescribed material volume fraction is 0.30. The design domain is meshed by 17700 square four-node elements of unit edge length. A concentrated load of  $F = 3.5$  kN is distributed over eleven neighbouring nodes along the top edge to avoid stress concentration. A fatigue strength  $\bar{\sigma}^f$  of 253 MPa and a von Mises stress constraint  $\bar{\sigma}^s$  of 660 MPa are considered.



**Figure 75** - Corbel design domain and geometrical dimensions

As for the other benchmarks, four cases are considered. Figure 76a shows the optimized topology with only the volume constraint, Figure 76b shows the optimized topology with the volume and the von Mises constraint, Figure 76c shows the optimized topology with the volume and the fatigue constraint on the first principal alternate stress and Figure 76d shows the optimized topology with all the constraints.

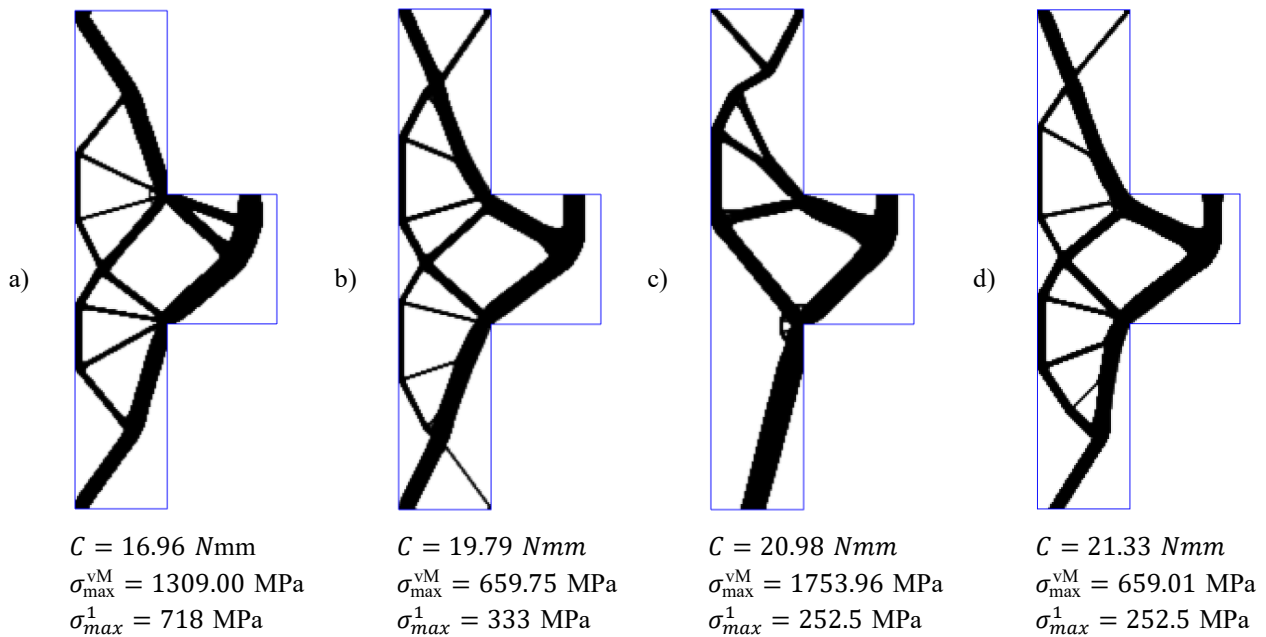


**Figure 76** - Optimisation results for the corbel structure

This example further confirms the effectiveness of the proposed methodology. An increment of the compliance is compensated by the possibility to ensure the structural integrity of the optimized component. In the topology obtained by considering both constraints, the first principal alternate stress and the von Mises stress are below the corresponding admissible values.

Figure 77 shows the stress distribution in the topology obtained by considering all the constraints (Figure 76d): Figure 77a shows the first principal alternate stress, whereas Figure 77b shows the von Mises stress.

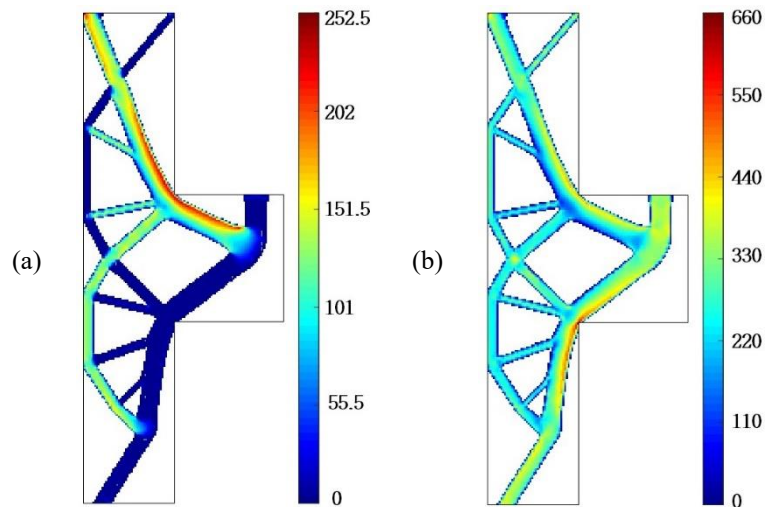


**Figure 77** - Stress distribution of the optimized corbel

As for the other two cases, where the von Mises stress is higher, the first principal alternate stress is smaller and vice versa, highlighting the importance of considering both stress constraints.

Figure 78a and Figure 78b show the trend of the most meaningful quantities during the optimisation process. In particular, Figure 78a shows the compliance and the stress with respect to the number of iterations (the compliance, the K-S fatigue function and the first principal alternate stress are shown); whereas Figure 78b shows the material volume ratio and the stress with respect to the number of iterations (the K-S stress function and the maximum von Mises stress).

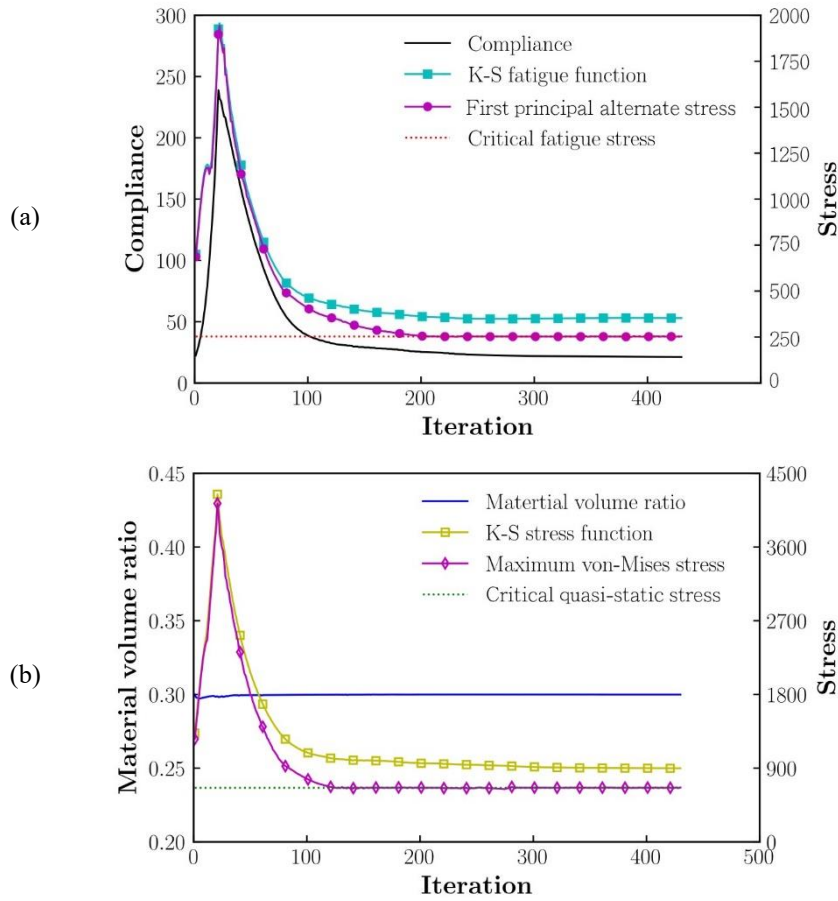


**Figure 78** - Iteration histories for optimisation of the corbel structure

As for the other two examples, the algorithm rapidly converges (less than 200 iterations) with limited fluctuations, further proving the efficiency of the proposed topology optimisation algorithm with fatigue constraints.

## 4.5 *TopFat* extension to commercial software

Even if *TopFat* is a first step in evaluating the final topology including the defect population, it is not immediately extendible to the industrial applications which may require this type of safe design.

Firstly, the *TopFat* procedure is implemented in the *HyperWorks* commercial software. The previous optimized topologies are compared with those obtained implemented by using *HyperWorks*. The differences between the two topologies are highlighted and discussed, with the aim of showing that the *TopFat* methodology can be reliably used for the design against fatigue failures from defects even with topology optimisation algorithms implemented in commercial software. Secondly, *TopFat* is extended in *HyperWorks* to support different loading conditions and stress ratios different from zero. Lastly, the *TopFat* criterion within the Hypermesh framework is used to safely re-design a real component for the aerospace industry to be produced by AM processes and therefore affected by a defect population.

It is worth to note that *HyperWorks* provides the possibility to limit only the maximum first principal stress  $\bar{\sigma}^{f,max}$  and not the alternate one  $\bar{\sigma}^f$ . Therefore the Eq.60 [65] is used in place of Eq.36 presented in *HyperWorks* [115].

$$\bar{\sigma}^{f,max} = \frac{2\bar{\sigma}^f}{1 - R} \quad (60)$$

### 4.5.1 Benchmarking validation

In the following paragraph, all the test cases reported and analysed with the *TopFat* original algorithm are reproduced with *HyperWorks* topology optimisation tool for benchmarking validation. In the original *TopFat* algorithm, the hybrid stress element model [124] is used to improve the accuracy of the stress measure evaluation without adding extra nodes. However, this element model is not implemented in the *HyperWorks* environment, so second-order elements are used to have accurate stress measures. While the accuracy of both element models is almost identical, the use of second-order elements rises the computational cost as a side effect. The filtering radius is set equal to 1.2 mm as imposed in the *TopFat* original algorithm. However, in the *TopFat* original algorithm both a continuation method and a non-linear projection are employed to avoid local minima and obtain cleaner final topologies [57,61]. These routines are not included in the *HyperWorks* environment and surely this discrepancy affects the results as it will be shown thereafter. To overcome these differences, all the optimisations in *HyperWorks* are carried out with a convergence parameter set equal to  $10^{-5}$ , while  $10^{-2}$  in *TopFat* original algorithm, and without a limit on the maximum number of iterations. Indeed, for the analysed benchmarks in *HyperWorks*, if the convergence parameter was set equal to  $10^{-2}$ , it would not be enough to reach a clear and definite final topology. Another difference consists of the type of programming solver: in *TopFat* original algorithm the Method of Moving Asymptotes (MMA) is used [25] which is considered one of the most efficient for solving topology optimisation problems. Instead, in *HyperWorks*, the Method of Feasible Direction (MFD), i.e. the software default one, is employed.

The limit on the von Mises equivalent stress is set according to the supposed Yield stress. As for the fatigue constraint, by substituting the required values in Eq.36 and 60, it results that the limit is around 510 MPa for all three benchmarks. Accordingly, in the *TopFat* original test cases the alternate first principle stress limit is set to 255 MPa which corresponds to a limit of 510 MPa with a stress ratio equal to zero by Eq.60. It is worth noting that, to visualize better the final topologies in *HyperWorks* topology optimisation, the command ‘Iso’ is used. Basically, this command discards from the final visualisation all the elements with a density inferior to a certain threshold, in the following cases 0.505. In Figure 79a and in Figure 79b the final topology obtained in *TopFat* and the one obtained with *HyperWorks* are reported, respectively (Notation -  $C$ : compliance;  $\sigma_{max}^{vM}$ : maximum von Mises equivalent stress;  $\sigma_{max}^1$ : maximum first principal stress). The original *TopFat* solution requires around 1000 iterations whereas the *HyperWorks* 4090. As it can be noticed the topologies are quite different especially in the lower-left portion of the domain. Moreover, the *HyperWorks*

solution is 7% stiffer and the maximum stresses are conservatively smaller than the corresponding limit stresses. However, the re-entrant corner is partially included in the final topology whereas it is excluded in the original *TopFat* solution. Anyway, in both the topologies a feasible solution is found, guarantying the structural safety according to the employed discretization model.

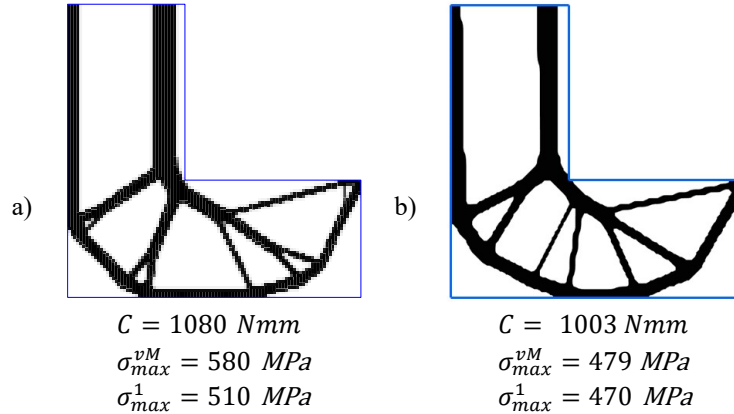


**Figure 79 - TopFat L-shape benchmark**

As for the cantilever domain, almost the same considerations highlighted for the L-shape domain can be carried out. Figure 80a shows the solution obtained in the original *TopFat* while Figure 80b shows the one obtained via *HyperWorks* topology optimisation. The *HyperWorks* solution converges in 554 iterations while the original *TopFat* final topology is reached in roughly 750 iterations. In this case, the final topologies are remarkably different, but both belong to the feasible design regions of the optimisation. The *HyperWorks* solution is 10% stiffer and the stresses are well below the imposed limits. However, the *HyperWorks* solution partially includes the upper and lower edge in the final topology. These are the most stressed zones for the cantilever structure and for this reason they are excluded in the original *TopFat* result. Lastly, the Corbel structure optimisations reported in Figure 81a and Figure 81b are obtained with the original *TopFat* algorithm and the *HyperWorks* topology optimisation, respectively. In this case, the *HyperWorks* topology optimisation algorithm has not been able to reach a feasible design. The stresses result to be higher than the imposed limits and the final topology is badly and poorly connected even if the convergence has been reached after 2119 iterations (450 in *TopFat*).

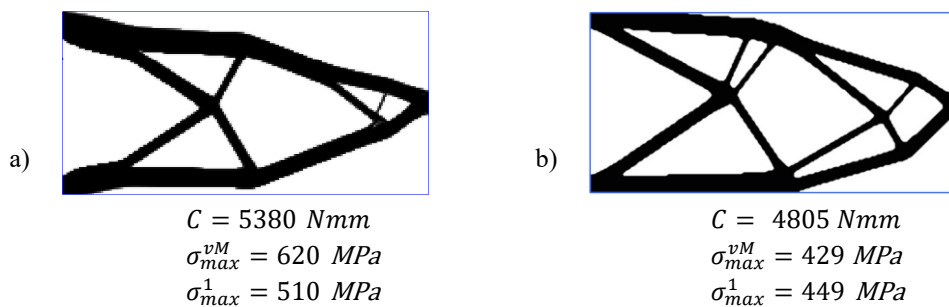


**Figure 80 - TopFat Cantilever benchmark**

This phenomenon can be addressed to the extreme characteristics of this geometry. Indeed, this case is analysed in the literature to show the weaknesses of the topology optimisation algorithms. As a matter of fact, the *TopFat* original algorithm is tested under these severe conditions with the precise purpose of showing the reliability and efficiency of the method. On the contrary, the *HyperWorks* topology optimisation solver is easily extendible to many other different topology optimisation problems, but it is less specific than the original *TopFat* algorithm. Overall, it can be concluded that the *TopFat* original algorithm is extremely efficient even with hard geometry conditions but its extendibility to other topology optimisation problems is complicated and the software is not available for most companies and industries. On the contrary, *HyperWorks* topology optimisation can include the *TopFat* procedure, i.e. including the defect population analysis within the topology optimisation framework, but it may not reach a feasible solution in specific complex problems (or the set of topology optimisation settings can be hardly defined). However, this partial limitation in *HyperWorks* can be quite easily overcome with an appropriate problem set-up, generally followed when components are to be designed with topology optimisation algorithms. For example, the re-entrant corners can be round by the designer before the optimisation, reducing stress concentrations. Additionally, the re-design phase after the optimisation, would permit to reduce possible peak stresses and to obtain a feasible topology.

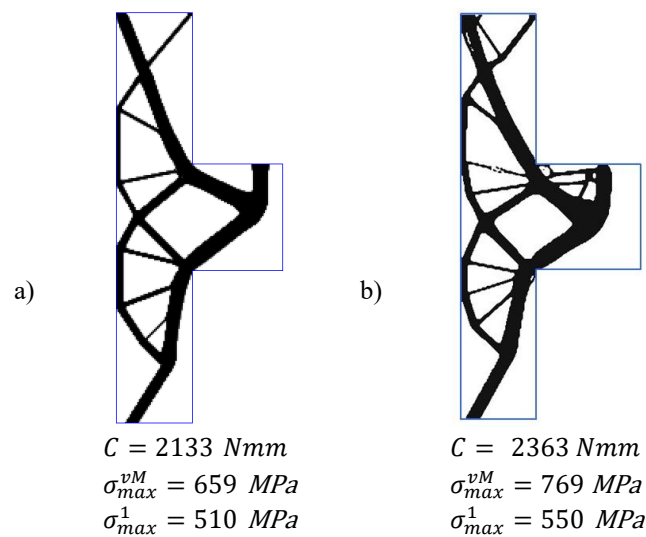


**Figure 81 - *TopFat* Corbel benchmark**

#### 4.5.2 Variable stress ratio

*HyperWorks* allows to set the topology optimisation with a constraint over the maximum first principal stress,  $\bar{\sigma}^{f,max}$ , that is evaluated according to Eq.60. Objective of this paragraph is to extend the original *TopFat* to variable stress ratio in order to evaluate wide ranging applications.

The corbel geometry as reported in Figure 82 is employed to perform different defect-driven topology optimisation [65]. The material is supposed to be AlSi10Mg, indeed it is one of the most employed in additive manufacturing metal

production [135]. In Table 9, all the data related to the material properties and defect distribution, needed for the topology optimisation problem setup, are reported.

Parameter	Value
AM AlSi10Mg Young modulus $E$ [ GPa ] [136]	$E = 75$
AM AlSi10Mg Poisson ratio $\nu$ [136]	$\nu = 0.3$
AM AlSi10Mg Yield limit $R_{p02}$ [ MPa ] [136]	$R_{p02} = 260$
AM AlSi10Mg Vickers hardness [HV] [136]	$HV = 120$
Superficial defect location parameters $C_1$ [116]	$C_1 = 1.41$
LEVD location parameter $\mu_{\sqrt{a}}$ [ $\mu\text{m}$ ] [136]	$\mu_{\sqrt{a}} = 139.94$
LEVD scale location parameter $\sigma_{\sqrt{a}}$ [ $\mu\text{m}$ ] [136]	$\sigma_{\sqrt{a}} = 35.05$
Reference volume $V_0$ [ $\text{mm}^3$ ] [136]	$V_0 = 0.01$
Initial volume $V_s$ [ $\text{mm}^3$ ]	$V_s^{corbel} = 17700$
Upper limit volume, $\bar{V}$	$\bar{V} = 0.3 \cdot V_s$

**Table 9** - Material, defect population and fatigue modelling parameters

The applied force  $F_{max}$ , as shown in Figure 82, is downward with an amplitude of 600 N. It is applied on the twenty closest nodes to the indicated point in Figure 82 so that artificial stress concentrations are avoided. This force is considered as the maximum applied force within the fatigue cyclic history load. According to the *TopFat* procedure, in the condition of R equal to zero, i.e. the applied force varies from zero to its maximum, this is the only force that is needed to be considered. The limit over the maximum first principal stress can be straightforwardly accessed by Eq.60 as twice the limit on the alternate one. If a condition with R greater than 0 is considered, i.e. the applied minimum force  $F_{min}$  is not null but anyway downward, the limit on the maximum first principal stress changes accordingly to Eq.60 but no other modifications are needed in the topology optimisation set up. Indeed, the minimum force  $F_{min}$ , in this case, can be considered as scaled-down from  $F_{max}$ . This means that the stress field would change in magnitude and not in sign. Indeed, the material portions under traction condition would remain identical. In other words, the only effect in the crack propagation is that average applied stress is higher, and this effect is already evaluated in the limit by Eq.60. It is enough to ensure that the limit on the maximum first principal stress is respected in the worst case, i.e.  $F_{max}$ , to conclude that no defects will let propagate the crack. Reversely, if a negative R is considered, then the applied minimum force  $F_{min}$  is in the opposite sense of the maximum one  $F_{max}$ , changing completely the stress field. In this condition, two different load cases must be considered: the first one with the  $F_{max}$  downward force and the second with the  $F_{min}$  upward force. Indeed, the change in sense of the applied force put in traction other zones of the material, previously in compression with the downward force. The two load cases are needed to ensure

that in all the parts of the material under traction during the historic cyclic load the first principal stress is not larger than the Murakami fatigue limit. In both load cases, Eq.60 provides the limit of the maximum first principal stress. Therefore, when the stress ratio  $R$  is negative, it is crucial to impose the limit in the two different stress distributions to ensure that no crack will propagate from the defects.

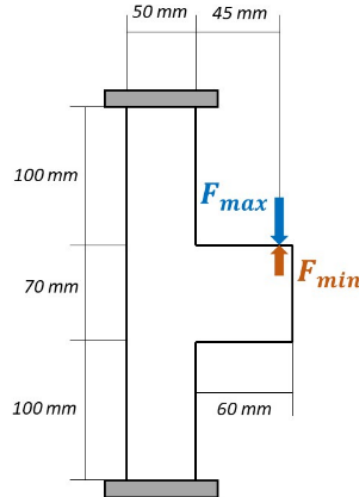


**Figure 82** - Corbel design domain for variable stress ratio

More generally, given an estimated defect population such as that supposed for AM AlSi10Mg reported in Table 9, it is possible to map the limit in the alternate first principal stress limit with respect to the variable stress ratio  $R$  according to Eq.36, as shown in Figure 83a.

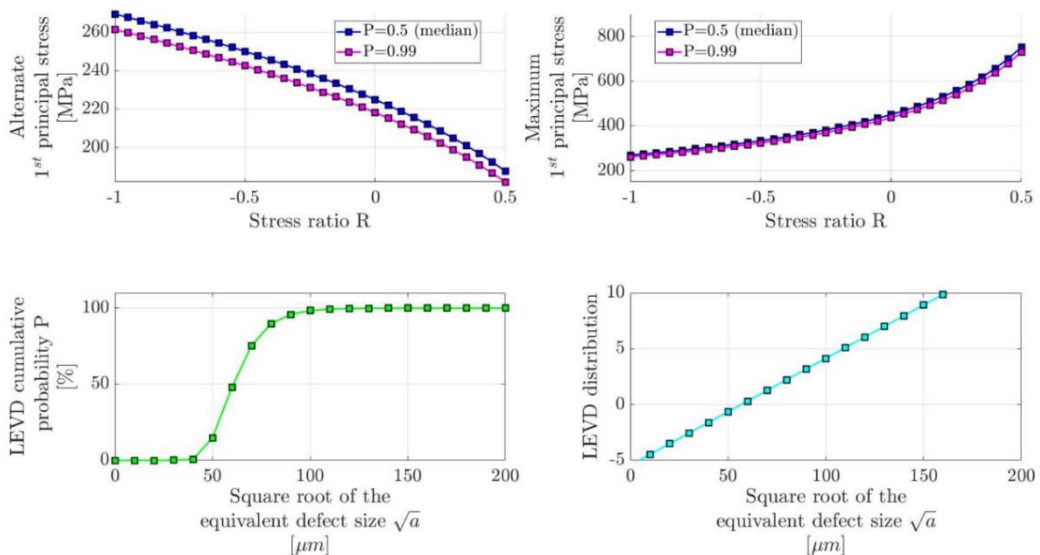


**Figure 83** - Defects and related fatigue limits

Similarly, through Eq.60 it is possible to plot the maximum first principal stress limit with respect to  $R$  as reported in Figure 83b. This plot can be used to set the Murakami fatigue limit in the topology optimisation *HyperWorks* environment. It is worth noting that the fatigue limit estimated with Eq.36 must be

limited to the fatigue limit without defects, according to [116]. A constant stress constraint over the quasi-static structural limit must be also set [115]. On the contrary, it is worth remembering that, if the considered stress ratio is smaller than 0, two different load cases must be imposed in the topology optimisation setup, one for the different senses of the applied force. Finally, Figure 83c and Figure 83d show an example of the LEVD cumulative distribution function and of the Gumbel plot for the defect size within the final optimised part, respectively. As for the finite element analysis, square second-order elements have been employed with a side length of 2 mm, i.e. 8850 elements. The filtering radius for the optimisation is set to 4 mm, i.e. 2 times the element size. It has been verified that a smaller value of the filtering radius may lead to very tiny side structures in the final topology. On the other hand, a filtering radius greater than 3 times the element size may increase remarkably the amount of element with intermediate densities at the end of the optimisation, affecting the final topology reliability. Overall, for this type of optimisation, the filtering radius should belong to the range between 1.5 and 3 times the element size. As for the convergence parameters, with a maximum number of cycles equal to 500 and a convergence checker of  $10^{-4}$ , the final topology results to be almost clear and well defined. Four different stress ratio conditions are selected to carry out the topology optimisation in *HyperWorks*. First, the stress ratio  $R$  is set equal to -1, i.e. fully reversed tension-compression. This condition is characterised by the lowest value of the limit on the maximum allowable stress of 116 MPa according to Eq.60 and as visible in Figure 83a. As already mentioned, two different load cases are set, the first one with  $F_{max}$  downward and the second with  $F_{min}$  equal to  $-F_{max}$  (upward). Concurrently a limit on the total volume fraction of 30% and the maximum admissible von Mises stress equal to 260 MPa are imposed. Figure 84a shows the result of the optimisation where all the constraints have been satisfied. Therefore, the structure can be considered safe even if the predicted greatest defect, according to the LEVD distribution, would accidentally lay in the highest tensile-stressed portion of the material in any of the different load cases.

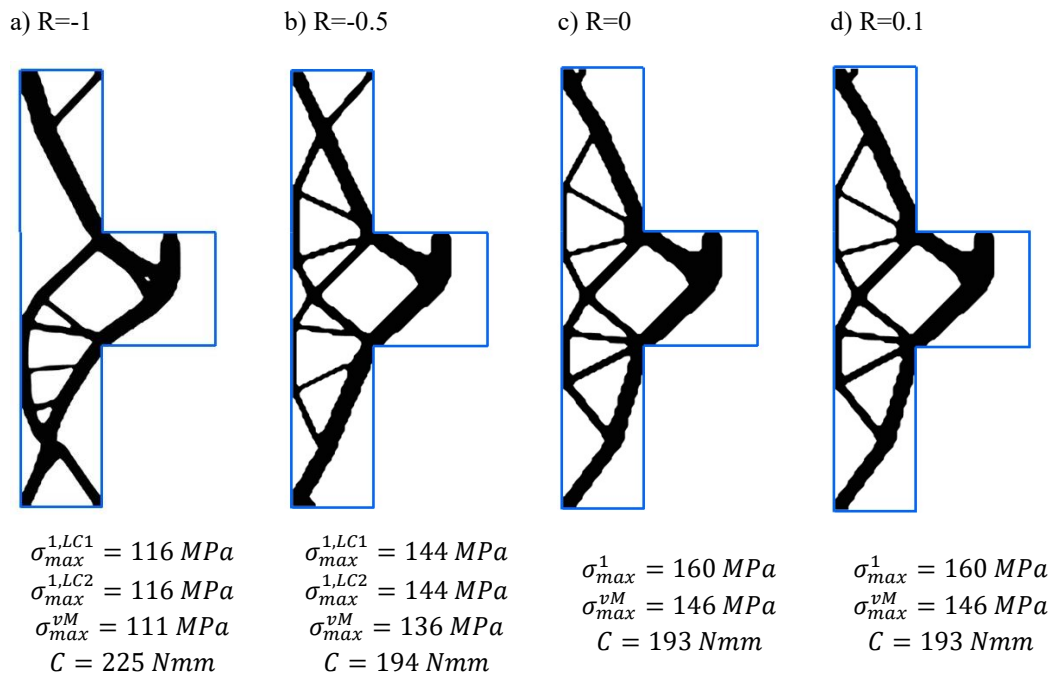


**Figure 84** – Final topologies under different stress ratios

Similarly, considering a stress ratio R of -0.5, the Murakami limit is evaluated as 144 MPa. In this case, the minimum force is equal to half -  $F_{max}$ . Again, the final topology results to be structurally safe and all the constraints are satisfied, as shown in Figure 84b. Considering R equal to 0 and 0.1, the Murakami limits are 196 MPa and 213 MPa respectively. In both conditions, a single load case with  $F_{max}$  downwards is applied. The final topologies, in Figure 84b Figure 84c, are almost identical since the stress limits are quite high and the convergence with the minimum compliance with a volume fraction of 30% is achieved. It is worth noting that all the topologies shown in Figure 84 are obtained with the command ‘Iso’ within the *HyperWorks* output environment with a value set to 0.35. It discards all the elements whose intermediate density is below this imposed value to obtain a clearer final topology. As an explicative example, the first principal stress  $\sigma^1$  in the final topology obtained with R equal to -1 is reported in Figure 85. The tensile zones are completely different in the two load cases, stating the need for the two different loading conditions. For more, the maximum first principal stress is below the prescribed limit, ensuring the fatigue structural safety in presence of defects.

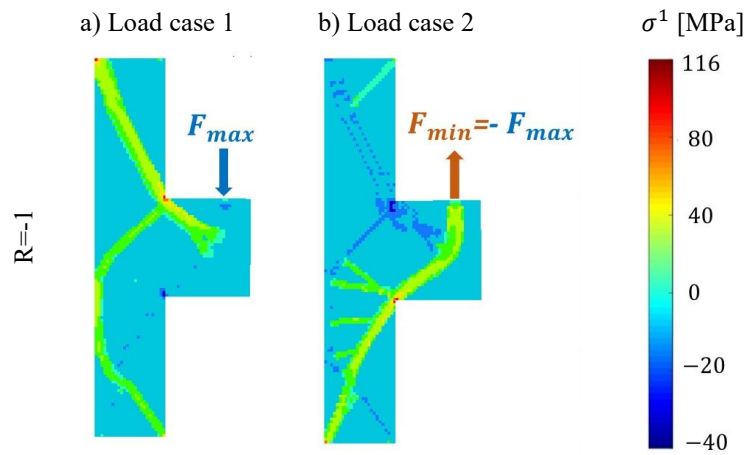
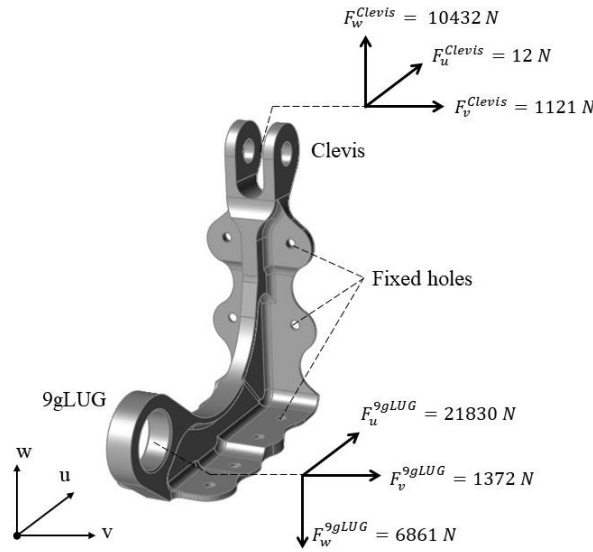


Figure 85 - First principal stress distribution in the final topology

### 4.5.3 Industrial application

In this paragraph, a real application case from the aerospace industry is optimised with *TopFat* implanted in *HyperWorks*. Figure 86 reports the *Leonardo Spa* company's original component together with the related boundary conditions. It consists of a bracket whose purpose is to connect the hatboxes to the structural beams inside the aircraft fuselage. The original geometry is achieved employing traditional methodologies, i.e. milled from a semifinished product, in aluminium T7050. The bracket is linked to the fuselage with 12 rivets through the tiny holes reported in Figure 86, named accordingly *fixed holes*. The hatboxes are connected to the bracket using two pins that fit in the two bushings, named *9gLug* and *Clevis* in Figure 86. During the flight manoeuvres, the aircraft undergoes several accelerations and, therefore, the weight of the hatboxes burden the components, applying consistent loads. To evaluate the most critical loads and the related bracket quasi-static safety, the highest accelerations that the aircraft can bear are considered. For more, the hatboxes are considered fulfilled with passenger goods, to simulate the worst condition. This analysis is carried out internally to *Leonardo Spa* company considering the full aircraft model and it is here omitted for brevity reasons. Under these severe conditions, it is possible to evaluate the pin loads transferred to the bracket with respect to the reference system called *u-v-w* reported in Figure 86. In the present paper, the bracket only is modelled, and the rivets connections are simulated locking all the degrees of freedom of the internal hole surfaces whereas the pins are substituted by rigid elements (RBE2 in *Hypermesh*) to transfer the single point loads presented in Figure 86 to the internal surfaces of the bushings. The main purpose of the bracket re-design is to reduce the component weight since it is a crucial prerequisite for aerospace parts, affecting fuel consumption remarkably. *Leonardo Spa* fixed a desirable target mass reduction of about 2% with respect to the original bracket in Figure 86 while guaranteeing the structural safety of the structure. Furthermore, *Leonardo Spa* addressed as desirable technology for the new bracket production the Electron Beam Melting (EBM) additive process by *Arcam* company, with Ti6Al4V powder. The re-design is therefore carried out using the *TopFat* procedure within

the *HyperWorks* environment considering these *Leonardo Spa* prescriptions and guidelines.



**Figure 86** - Original component geometry and boundary conditions

With the aim of designing the component in the fatigue regime, the nominal load conditions are required. Therefore, according to [137] the nominal load conditions can be calculated dividing the maximum ones by a factor equal to 1.5. Table 10 reports the maximum and the nominal conditions which the brackets undergo during its life.

Load	Worst condition	Nominal condition
$F_w^{Clevis}$ [N]	10432	6955
$F_u^{Clevis}$ [N]	12	8
$F_v^{Clevis}$ [N]	1121	747
$F_w^{9gLUG}$ [N]	-6861	-4574
$F_u^{9gLUG}$ [N]	21830	14553
$F_v^{9gLUG}$ [N]	1372	915

**Table 10** - Applied loads in worst and nominal conditions

As already mentioned, the re-design material is supposed to be Ti6Al4V processed by EBM technology. The material data about EBM Ti6Al4V are reported in Table 2 and it is directly obtained by the material data sheet provided by *Arcam* company [138]. Additionally, in Table 11, the data related to the defect distribution, needed for the topology optimisation problem setup, are reported. The data are extrapolated from the defect population found in [139] of *Arcam* EBM Ti6Al4V samples, with suggested process parameters, machined and without post-process heat treatment. This experiment setup can be assumed to be fairly close to that for possible production of the analysed component. If very different process parameters or post-production treatments, such as the hot

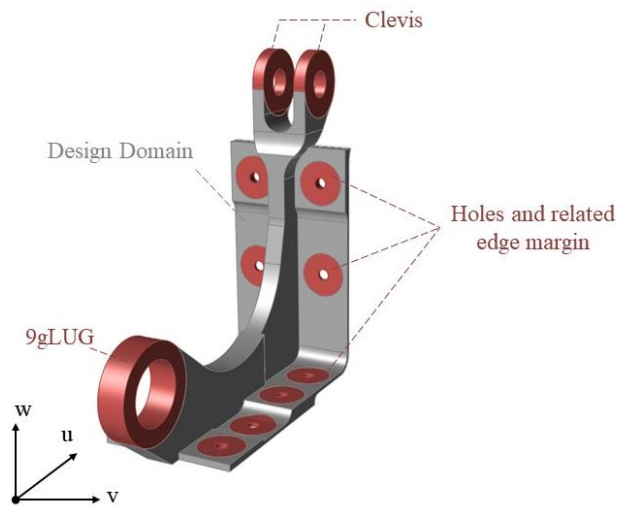
isostatic pressure (HIP), were employed, a novel defect analysis would be necessary to estimate the LEVD parameters as indicated by [116].

The optimisation in Hypermesh is carried out using the nominal set of loads reported in Table 10 since the bracket must be verified structurally in the fatigue regime. This condition is verified during the optimisation imposing a constraint over the maximum first principal stress  $\bar{\sigma}^{f,max}$ , according to Eq.60. This value is equal to 450 MPa for the defect population data reported in Table 10. For more, another constraint is imposed over the maximum allowable final mass, as prescribed by *Leonardo Spa*. Since the original bracket weight is 160 g, the maximum allowable mass results to be 156 g. This constraint is equivalent and substitutes the volume fraction constraint imposed in the *TopFat* procedure [65]. Last, a limit over the von Mises equivalent stress equal to the Yield stress is imposed to verify the quasi-static safety. The objective of the optimisation is compliance minimisation, i.e. global stiffness maximisation.

Parameter [138]	Value
EBM Ti6Al4V Young modulus $E$ [GPa]	$E = 119$
EBM Ti6Al4V Poisson ratio $\nu$	$\nu = 0.3$
EBM Ti6Al4V density $\rho$ [g/mm <sup>3</sup> ]	$\rho = 4.42 \cdot 10^{-3}$
EBM Ti6Al4V Yield limit $R_{p02}$ [MPa]	$R_{p02} = 866$
EBM Ti6Al4V Vickers hardness $HV$	$HV = 350$
Superficial defect location parameters $C_1$	$C_1 = 1.41$
LEVD location parameter $\mu_{\sqrt{a}}$ [ $\mu\text{m}$ ]	$\mu_{\sqrt{a}} = 60.78$
LEVD scale location parameter $\sigma_{\sqrt{a}}$ [ $\mu\text{m}$ ]	$\sigma_{\sqrt{a}} = 10.15$
Reference volume $V_0$ [mm <sup>3</sup> ]	$V_0 = 0.01$
Maximum admissible mass $M$ [g]	$M = 156$
Final structure volume, $V_n = M/\rho$ [mm <sup>3</sup> ]	$V_n = 35294$

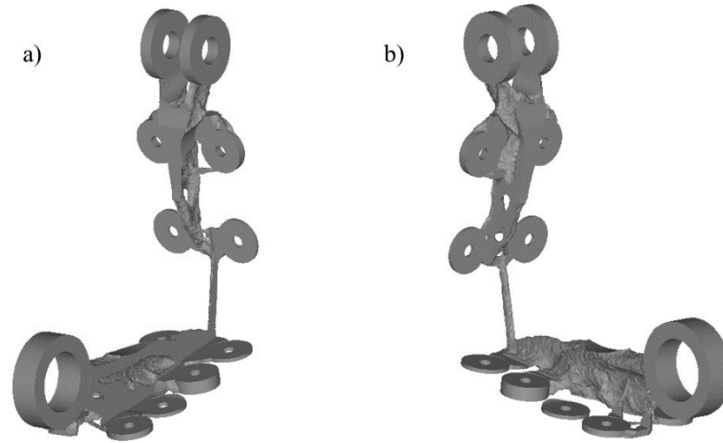
**Table 11** - Values of modelling parameters

Figure 87 shows the division in non-design domain (NDD) in red and design domain (DD) in grey of the bracket for the topology optimisation process. As it can be noticed, both the bushings, *Clevis* and *9gLug*, are set as NDD to ensure the connectivity with the pins. Similarly, an offset circular zone is set around the holes to guarantee the rivets hold. The DD is set equal to the remaining part of the bracket where the lightning features from the traditional manufacturing are removed. In particular, the full thickness of the rib is included and handles around the fixed holes are removed. No other additions of material can be done to the design domain due to the necessity of guaranteeing the assembly of the final part with other components.



**Figure 87** - Design domain and No design domain definition

The geometry in Figure 87 is used for the optimisation and it discretised in 449444 first-order R-tetra elements. The connection between the NDD and the DD is ensured using contact elements. The convergence parameter is set equal to 0.005 while no maximum number of iterations is imposed. The filtering radius is set equal to 2 mm, i.e. two times the imposed maximum element size. The topology optimisation process reaches a feasible solution, where all the constraints are satisfied, in 163 iterations. The final topology is shown under a different point of views in Figure 88 with a filter on the intermated density equal to 0.5 (command 'Iso' in Hypermesh). Some considerations must be done on this solution: first of all, the tiny bar connecting the two grater masses may be removed in the CAD re-design of the model, however, it is crucial to guarantee the link between the bushings and keep the bracket mono-component. Secondly, one rivet connection is detached from the rest of the body since the number of constraints is highly redundant and this one it is not considered vital by the optimizer. Anyway, it can be easily linked afterwards in the CAD re-design not to lose the rivet connection. In Figure 89, the von Mises equivalent stress and the maximum first principal stress distribution are reported as obtained after the optimisation. As it can be noticed, both respect the imposed limits, and the optimised bracket is structurally safe.



**Figure 88** - Topologically optimised component

Since the model is fully linear elastic, simply rescaling the maximum von Mises stress for 1.5, that used to find the nominal condition, it results to be 630 MPa, less than the Yield stress equal to 866 MPa. It means that the part is safe in quasi-static conditions as well.

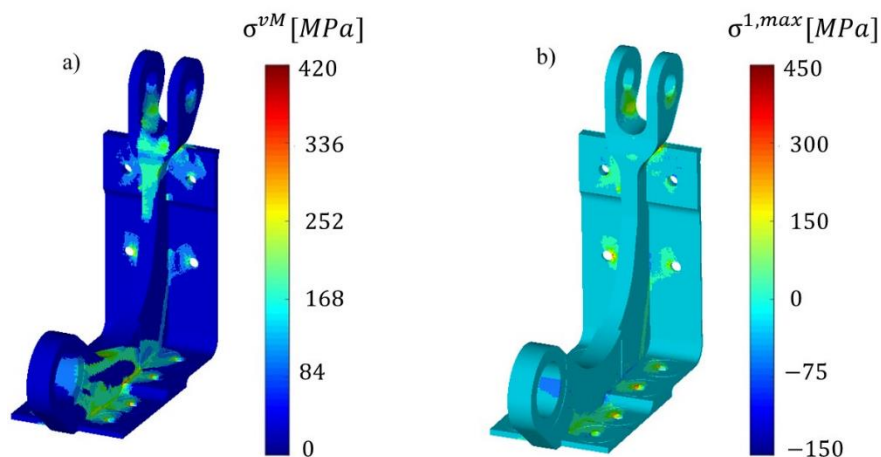


**Figure 89** - Optimised component result data

## 4.6 *TopFat* final remarks

*TopFat* is able to provide safely optimised components and prevent from possible fatigue collapse in working conditions due to the presence of large defects which are generally neglected when components are designed. Indeed, material and manufacturing defects are the cause of fatigue failures in many components, especially in those produced through AM processes and generally designed with topology optimisation algorithms. In order to model the influence of defects on the fatigue response, a stress constraint on the first principal alternate stress is introduced in the topology optimisation algorithm. In particular, the first principal alternate stress, responsible for the crack nucleation and propagation from defects, is limited to a stress amplitude corresponding to the fatigue strength computed according to the well-known Murakami formulation.

The dependency between the defect size and the material volume is also considered with the Largest Extreme Value Distribution (LEVD). A second stress constraint is introduced in order to limit the stress in elements subjected to compression stress and, therefore, not critical for the fatigue response.

The main results can be summarized as follows:

1. *TopFat* provides a final topology with maximised stiffness under volume, quasi-static and fatigue constraints.
2. The fatigue constraint is defect driven, which is a fundamental aspect especially when designing components to be produced through Additive Manufacturing processes, characterized by a fatigue behaviour worse than that of components produced through traditional processes due to the presence of large manufacturing defects.
3. The main issues related to the density-based topology optimisation process and stress-constraints are considered and combined, guaranteeing smooth convergence.
4. The validation with three benchmarks confirms that the proposed algorithm permits to obtain a final topology with the first principal alternate stress below the fatigue strength in presence of defects and a von Mises stress below an admissible stress (e.g., yield stress divided by a safety coefficient) with a rapid convergence.
5. The *TopFat* procedure can be easily extended in the commercially available software *HyperWorks* allowing the evaluation of variable stress ratios and 3D complex cases.

# Conclusions

The present dissertation provides a complete description of the Top Suite, a set of three different algorithms solving topology optimisation problems to thrive the additive manufacturing applications.

The first, *TopTM* allows optimising thermo-mechanical systems with the aim of maximising concurrently the structural stiffness and the heat exchange. *TopTM* can be implemented in the commercially available software Ansys in a few code lines. It is fast convergent and based on an optimality criterium. The analytical derivation and the solving procedure avoid local minima and intermediate densities in the final results. It can be used to optimise parts such as engines, turbine blades, heat exchangers and more, guaranteeing high performance and weight reduction.

The second, *TopComp*, optimises parts to be produced as fibre reinforced composite. *TopComp* concurrently provides the final part as a sequence of layers. Each layer is fully optimised, both for the material distribution and the local fibre orientation. *TopComp* is based on two different optimality criteria and, similarly to *TopTM*, it is fast convergent, avoids local minima and intermediate densities in the final results. Furthermore, it can be implemented in the commercially available software Ansys in a few code lines. This algorithm allows the production of fibre reinforced parts with mechanical performance comparable with metal ones, being suitable for their substitutions with incredible weight reduction.

The third, *TopFat*, is a complex algorithm able to include the presence of process-induced defects in the optimisation procedure. Employing the Murakami model, the presence of defects in the final part can be estimated as a limit over the first principal stress. Ensuring this limit, the final part can be considered reliable from the fatigue point of view. This algorithm can be extended in the commercially available software HyperWorks and be used to topologically optimise complex and three-dimensional components.

Overall, the Top Suite is an easy-to-use product, easily accessible by the academic and industrial community. It helps designers to exploit novel possibilities offered by additive manufacturing processes or avoid its weaknesses.

# Recommendations for future research

The *Top Suite* has been developed to foster the AM applications. Future research may take different roads to improve the work highlighted in this dissertation.

Future research may be more focused on industrial applications. Therefore, it may be extremely useful to implement the *Top Suite* in a unique platform to simplify its widespread use.

*TopTM* and *TopComp* are coded without stress or temperature constraints, which can be a meaningful implantation. Indeed, for most of industrial applications this aspect is crucial, and it may compromise the final topology applicability. Related to this topic there is the possibility to include the buckling constraint in the optimisation process. As a matter of fact, final topologies are often characterised by slender bars and structures which can easily suffer from elastic instability.

*TopFat* considers the defect population in its worst scenario. Indeed, the final topology is obtained as if in every part of the material may be present the biggest defect. This assumption is precautious but do not really mirror the real material condition. The design domain should be divided in intervals related to the current first principal stress evaluation, according to Murakami model. The main issue is that this discretisation creates discontinuities in the design domain which are difficult to be treated in the sensitivity analysis. However, this progress would increase the performance of the final obtained part.

The *Top Suite* is written in a deterministic approach, i.e. material properties, loads, constraints and all the other quantities in the problem formulation are considered fixed and immutable. This approach leads to extremely optimised final components, but it may create troubles after their realisation and implementation. Indeed, real properties may be slightly different from the pure numbers used in the optimisation process. For example, the direction of the load may be some cents of grades different from the hypothetic one due to real-world uncertainties. This would lower the theoretical performance of the optimised parts. To solve this problem a stochastic approach may be used in the problem formulation in order to make the *Top Suite* even more robust, reliable, and useful for industrial applications.

# References

- [1] A. Al Rashid, S.A. Khan, S. G. Al-Ghamdi, M. Koç, Additive manufacturing: Technology, applications, markets, and opportunities for the built environment, *Autom. Constr.* 118 (2020) 103268. <https://doi.org/10.1016/j.autcon.2020.103268>.
- [2] M. Benedetti, A. du Plessis, R.O. Ritchie, M. Dallago, S.M.J. Razavi, F. Berto, Architected cellular materials: A review on their mechanical properties towards fatigue-tolerant design and fabrication, *Mater. Sci. Eng. R Reports.* 144 (2021) 100606. <https://doi.org/10.1016/j.mser.2021.100606>.
- [3] B. Blakey-Milner, P. Gradl, G. Snedden, M. Brooks, J. Pitot, E. Lopez, M. Leary, F. Berto, A. du Plessis, Metal additive manufacturing in aerospace: A review, *Mater. Des.* 209 (2021) 110008. <https://doi.org/10.1016/j.matdes.2021.110008>.
- [4] Y. Lakhdar, C. Tuck, J. Binner, A. Terry, R. Goodridge, Additive manufacturing of advanced ceramic materials, *Prog. Mater. Sci.* 116 (2021) 100736. <https://doi.org/10.1016/j.pmatsci.2020.100736>.
- [5] E. Rezvani Ghomi, F. Khosravi, R.E. Neisiany, S. Singh, S. Ramakrishna, Future of additive manufacturing in healthcare, *Curr. Opin. Biomed. Eng.* 17 (2021) 100255. <https://doi.org/10.1016/j.cobme.2020.100255>.
- [6] Y. Wang, Y. Zhou, L. Lin, J. Corker, M. Fan, Overview of 3D additive manufacturing (AM) and corresponding AM composites, *Compos. Part A Appl. Sci. Manuf.* 139 (2020) 106114. <https://doi.org/10.1016/j.compositesa.2020.106114>.
- [7] S. Hällgren, L. Pejryd, J. Ekengren, (Re)Design for Additive Manufacturing, *Procedia CIRP.* 50 (2016) 246–251. <https://doi.org/10.1016/j.procir.2016.04.150>.
- [8] W.T. Carter, D.J. Erno, D.H. Abbott, C.E. Bruck, G.H. Wilson, J.B. Wolfe, D.M. Finkhousen, A. Tepper, R.G. Stevens, The GE Aircraft Engine Bracket Challenge: An Experiment in Crowdsourcing for Mechanical Design Concepts, 25th Solid Free. Fabr. Symp. (SFF ). (2014) 1402–1411.
- [9] J. Fan, L. Zhang, S. Wei, Z. Zhang, S.K. Choi, B. Song, Y. Shi, A review of additive manufacturing of metamaterials and developing trends, *Mater. Today.* xxx (2021). <https://doi.org/10.1016/j.mattod.2021.04.019>.
- [10] J. Liu, A.T. Gaynor, S. Chen, Z. Kang, K. Suresh, A. Takezawa, L. Li, J. Kato, J. Tang, C.C.L. Wang, L. Cheng, X. Liang, A.C. To, Current and future trends in topology optimization for additive manufacturing, *Struct. Multidiscip. Optim.* 57 (2018) 2457–2483. <https://doi.org/10.1007/s00158-018-1994-3>.
- [11] M.P. Bendsoe, O. Sigmund, *Topology Optimization: Theory, Methods and Applications*, 2002.
- [12] S. Cooke, K. Ahmadi, S. Willerth, R. Herring, Metal additive manufacturing: Technology, metallurgy and modelling, *J. Manuf. Process.* 57 (2020) 978–1003. <https://doi.org/10.1016/j.jmapro.2020.07.025>.
- [13] P. Parandoush, D. Lin, A review on additive manufacturing of polymer-fiber composites, *Compos. Struct.* 182 (2017) 36–53. <https://doi.org/10.1016/j.compstruct.2017.08.088>.
- [14] G. Gong, J. Ye, Y. Chi, Z. Zhao, Z. Wang, G. Xia, X. Du, H. Tian, H. Yu, C. Chen, Research status of laser additive manufacturing for metal: A review, *J. Mater. Res. Technol.* (2021). <https://doi.org/10.1016/j.jmrt.2021.08.050>.
- [15] H. Jia, H. Sun, H. Wang, Y. Wu, H. Wang, Scanning strategy in selective laser melting (SLM): a review, *Int. J. Adv. Manuf. Technol.* 113 (2021) 2413–2435. <https://doi.org/10.1007/s00170-021-06810-3>.
- [16] P. Ponnusamy, R.A.R. Rashid, S.H. Masood, D. Ruan, S. Palanisamy, Mechanical properties of slm-printed aluminium alloys: A review, *Materials (Basel).* 13

- (2020) 1–51. <https://doi.org/10.3390/ma13194301>.
- [17] I. Buj-Corral, A. Tejo-Otero, F. Fenollosa-Artés, Development of am technologies for metals in the sector of medical implants, *Metals (Basel)*. 10 (2020) 1–30. <https://doi.org/10.3390/met10050686>.
- [18] L.E. Murr, S. Li, Electron-beam additive manufacturing of high-temperature metals, *MRS Bull.* 41 (2016) 752–757. <https://doi.org/10.1557/mrs.2016.210>.
- [19] M.Q. Zafar, C.C. Wu, H. Zhao, J. Wang, X. Hu, Finite element framework for electron beam melting process simulation, *Int. J. Adv. Manuf. Technol.* 109 (2020) 2095–2112. <https://doi.org/10.1007/s00170-020-05707-x>.
- [20] L.C. Zhang, Y. Liu, S. Li, Y. Hao, Additive Manufacturing of Titanium Alloys by Electron Beam Melting: A Review, *Adv. Eng. Mater.* 20 (2018) 1–16. <https://doi.org/10.1002/adem.201700842>.
- [21] G. Liu, X. Zhang, X. Chen, Y. He, L. Cheng, M. Huo, J. Yin, F. Hao, S. Chen, P. Wang, S. Yi, L. Wan, Z. Mao, Z. Chen, X. Wang, Z. Cao, J. Lu, Additive manufacturing of structural materials, *Mater. Sci. Eng. R Reports*. 145 (2021) 100596. <https://doi.org/10.1016/j.mser.2020.100596>.
- [22] J. Plocher, A. Panesar, Review on design and structural optimisation in additive manufacturing: Towards next-generation lightweight structures, *Mater. Des.* 183 (2019). <https://doi.org/10.1016/j.matdes.2019.108164>.
- [23] G.I.N. Rozvany, A critical review of established methods of structural topology optimization, *Struct. Multidiscip. Optim.* 37 (2009) 217–237. <https://doi.org/10.1007/s00158-007-0217-0>.
- [24] J.D. Deaton, R. V. Grandhi, A survey of structural and multidisciplinary continuum topology optimization: Post 2000, *Struct. Multidiscip. Optim.* 49 (2014) 1–38. <https://doi.org/10.1007/s00158-013-0956-z>.
- [25] K. Svanberg, The method of moving asymptotes - a new method for structural optimization., *Int. J. Numer. Methods Eng.* 24 (1987) 359–373.
- [26] C. Wang, X.P. Tan, S.B. Tor, C.S. Lim, Machine learning in additive manufacturing: State-of-the-art and perspectives, *Addit. Manuf.* 36 (2020) 101538. <https://doi.org/10.1016/j.addma.2020.101538>.
- [27] T. Stejskal, M. Dovica, J. Svetlík, P. Demeč, L. Hrivniak, M. Šašala, Establishing the optimal density of the Michell truss members, *Materials (Basel)*. 13 (2020) 1–16. <https://doi.org/10.3390/ma13173867>.
- [28] Martin Philip Bendsoe, Noboru Kikuchi, Generating optimal topologies in structural design using a homogenization method, *Comput. Methods Appl. Mech. Eng.* 71 (1988) 197–224.
- [29] O. Sigmund, K. Maute, Topology optimization approaches: A comparative review, *Struct. Multidiscip. Optim.* 48 (2013) 1031–1055. <https://doi.org/10.1007/s00158-013-0978-6>.
- [30] C. Yang, Y. Kim, S. Ryu, G.X. Gu, Prediction of composite microstructure stress-strain curves using convolutional neural networks, *Mater. Des.* 189 (2020) 108509. <https://doi.org/10.1016/j.matdes.2020.108509>.
- [31] G.X. Gu, C.T. Chen, M.J. Buehler, De novo composite design based on machine learning algorithm, *Extrem. Mech. Lett.* 18 (2018) 19–28. <https://doi.org/10.1016/j.eml.2017.10.001>.
- [32] O. Sigmund, On the usefulness of non-gradient approaches in topology optimization, *Struct. Multidiscip. Optim.* 43 (2011) 589–596. <https://doi.org/10.1007/s00158-011-0638-7>.
- [33] R. Picelli, S. Ranjbarzadeh, R. Sivapuram, R.S. Gioria, E.C.N. Silva, Topology optimization of binary structures under design-dependent fluid-structure interaction loads, *Struct. Multidiscip. Optim.* 62 (2020) 2101–2116. <https://doi.org/10.1007/s00158-020-02598-0>.
- [34] P. Shi, Y. Qin, Y. Cao, H. Zhao, R. Gao, S. Liu, Topology optimization of metamaterial microstructure for wireless power transfer with high power transmission efficiency, *J. Magn. Magn. Mater.* 537 (2021) 168228. <https://doi.org/10.1016/j.jmmm.2021.168228>.

- [35] G.H. Yoon, E.M. Dede, T. Nomura, P. Schmalenberg, Topology optimization of time-transient heat conduction for thermo-optic silicon modulators, *Int. J. Heat Mass Transf.* 157 (2020) 119862. <https://doi.org/10.1016/j.ijheatmasstransfer.2020.119862>.
- [36] K. Suzuki, N. Kikuchi, Shape and topology optimization by a homogenization method, *Am. Soc. Mech. Eng. Appl. Mech. Div. AMD.* 115 (1990) 15–30.
- [37] C. Wang, X. Gu, J. Zhu, H. Zhou, S. Li, W. Zhang, Concurrent design of hierarchical structures with three-dimensional parameterized lattice microstructures for additive manufacturing, *Struct. Multidiscip. Optim.* 61 (2020) 869–894. <https://doi.org/10.1007/s00158-019-02408-2>.
- [38] W. Wu, W. Hu, G. Qian, H. Liao, X. Xu, F. Berto, Mechanical design and multifunctional applications of chiral mechanical metamaterials: A review, *Mater. Des.* 180 (2019) 107950. <https://doi.org/10.1016/j.matdes.2019.107950>.
- [39] A. V. Krysko, J. Awrejcewicz, S.P. Pavlov, K.S. Bodyagina, V.A. Krysko, Topological optimization of thermoelastic composites with maximized stiffness and heat transfer, *Compos. Part B Eng.* 158 (2019) 319–327. <https://doi.org/10.1016/j.compositesb.2018.09.047>.
- [40] A. Ueno, H. Guo, A. Takezawa, R. Moritoyo, M. Kitamura, Temperature distribution design based on variable lattice density optimization and metal additive manufacturing, *Symmetry (Basel)*. 13 (2021) 1–16. <https://doi.org/10.3390/sym13071194>.
- [41] T.P. Ribeiro, L.F.A. Bernardo, J.M.A. Andrade, Topology optimisation in structural steel design for additive manufacturing, *Appl. Sci.* 11 (2021) 1–66. <https://doi.org/10.3390/app11052112>.
- [42] M.P. Bendsøe, O. Sigmund, Material interpolation schemes in topology optimization, *Arch. Appl. Mech. (Ingenieur Arch.)* 69 (1999) 635–654. <https://doi.org/10.1007/s004190050248>.
- [43] O.M. Querin, G.P. Steven, Y.M. Xie, Evolutionary structural optimisation (ESO) using a bidirectional algorithm, *Eng. Comput. (Swansea, Wales)*. 15 (1998) 1031–1048. <https://doi.org/10.1108/02644409810244129>.
- [44] L. Zhao, B. Xu, Y. Han, J. Xue, J. Rong, Structural topological optimization with dynamic fatigue constraints subject to dynamic random loads, *Eng. Struct.* 205 (2020) 110089. <https://doi.org/10.1016/j.engstruct.2019.110089>.
- [45] M. Stolpe, K. Svanberg, An alternative interpolation scheme for minimum compliance topology optimization, *Struct. Multidiscip. Optim.* 22 (2001) 116–124. <https://doi.org/10.1007/s001580100129>.
- [46] N.P. Van Dijk, K. Maute, M. Langelaar, F. Van Keulen, Level-set methods for structural topology optimization: A review, *Struct. Multidiscip. Optim.* 48 (2013) 437–472. <https://doi.org/10.1007/s00158-013-0912-y>.
- [47] J. Hyun, H.A. Kim, Level-set topology optimization for effective control of transient conductive heat response using eigenvalue, *Int. J. Heat Mass Transf.* 176 (2021) 121374. <https://doi.org/10.1016/j.ijheatmasstransfer.2021.121374>.
- [48] G. Jing, J. Jia, J. Xiang, Level set-based BEM topology optimization method for maximizing total potential energy of thermal problems, *Int. J. Heat Mass Transf.* 182 (2022) 121921. <https://doi.org/10.1016/j.ijheatmasstransfer.2021.121921>.
- [49] C. Zhuang, Z. Xiong, H. Ding, Temperature-constrained topology optimization of nonlinear heat conduction problems, *J. Comput. Des. Eng.* 8 (2021) 1059–1081. <https://doi.org/10.1093/jcde/qwab032>.
- [50] D. Merayo, A. Rodríguez-Prieto, A.M. Camacho, Topological optimization of artificial neural networks to estimate mechanical properties in metal forming using machine learning, *Metals (Basel)*. 11 (2021). <https://doi.org/10.3390/met11081289>.
- [51] L. Zheng, S. Kumar, D.M. Kochmann, Data-driven topology optimization of spinodoid metamaterials with seamlessly tunable anisotropy, *Comput. Methods Appl. Mech. Eng.* 383 (2021) 113894. <https://doi.org/10.1016/j.cma.2021.113894>.
- [52] S. Zheng, H. Fan, Z. Zhang, Z. Tian, K. Jia, Accurate and real-time structural

- topology prediction driven by deep learning under moving morphable component-based framework, *Appl. Math. Model.* 97 (2021) 522–535. <https://doi.org/10.1016/j.apm.2021.04.009>.
- [53] S. Zhu, M. Ohsaki, K. Hayashi, X. Guo, Machine-specified ground structures for topology optimization of binary trusses using graph embedding policy network, *Adv. Eng. Softw.* 159 (2021) 103032. <https://doi.org/10.1016/j.advengsoft.2021.103032>.
- [54] K. Garbrecht, M. Aguilo, A. Sanderson, A. Rollett, R.M. Kirby, J. Hochhalter, Interpretable Machine Learning for Texture-Dependent Constitutive Models with Automatic Code Generation for Topological Optimization, *Integr. Mater. Manuf. Innov.* 10 (2021) 373–392. <https://doi.org/10.1007/s40192-021-00231-6>.
- [55] O. Sigmund, A 99 line topology optimization code written in matlab, *Struct. Multidiscip. Optim.* 21 (2001) 120–127. <https://doi.org/10.1007/s001580050176>.
- [56] J. Wu, O. Sigmund, J.P. Groen, Topology optimization of multi-scale structures: a review, *Struct. Multidiscip. Optim.* 63 (2021) 1455–1480. <https://doi.org/10.1007/s00158-021-02881-8>.
- [57] O. Sigmund, J. Petersson, Numerical instabilities in topology optimization: A survey on procedures dealing with checkerboards, mesh-dependencies and local minima, *Struct. Optim.* 16 (1998) 68–75. <https://doi.org/10.1007/BF01214002>.
- [58] G. Chiandussi, On the solution of a minimum compliance topology optimisation problem by optimality criteria without a priori volume constraint specification, *Comput. Mech.* 38 (2006) 77–99. <https://doi.org/10.1007/s00466-005-0722-1>.
- [59] A. Díaz, O. Sigmund, Checkerboard patterns in layout optimization, *Struct. Optim.* 10 (1995) 40–45. <https://doi.org/10.1007/BF01743693>.
- [60] O. Sigmund, K. Maute, Sensitivity filtering from a continuum mechanics perspective, *Struct. Multidiscip. Optim.* 46 (2012) 471–475. <https://doi.org/10.1007/s00158-012-0814-4>.
- [61] X. Gao, Y. Li, H. Ma, G. Chen, Improving the overall performance of continuum structures: A topology optimization model considering stiffness, strength and stability, *Comput. Methods Appl. Mech. Eng.* 359 (2020) 1–23. <https://doi.org/10.1016/j.cma.2019.112660>.
- [62] F. Wang, B.S. Lazarov, O. Sigmund, On projection methods, convergence and robust formulations in topology optimization, *Struct. Multidiscip. Optim.* 43 (2011) 767–784. <https://doi.org/10.1007/s00158-010-0602-y>.
- [63] G. Chiandussi, *Thermal and Structural Design*, (2004).
- [64] R. Caivano, A. Tridello, M. Codegone, G. Chiandussi, A new methodology for thermostructural topology optimization: Analytical definition and validation, *Proc. Inst. Mech. Eng. Part L J. Mater. Des. Appl.* (2020). <https://doi.org/10.1177/1464420720970246>.
- [65] X. Gao, R. Caivano, A. Tridello, G. Chiandussi, H. Ma, D. Paolino, F. Berto, Innovative formulation for topological fatigue optimisation based on material defects distribution and TopFat algorithm, *Int. J. Fatigue.* 147 (2021) 106176. <https://doi.org/10.1016/j.ijfatigue.2021.106176>.
- [66] T. Dbouk, A review about the engineering design of optimal heat transfer systems using topology optimization, *Appl. Therm. Eng.* 112 (2017) 841–854. <https://doi.org/10.1016/j.applthermaleng.2016.10.134>.
- [67] V. Subramaniam, T. Dbouk, J.L. Harion, Topology optimization of conductive heat transfer devices: An experimental investigation, *Appl. Therm. Eng.* 131 (2018) 390–411. <https://doi.org/10.1016/j.applthermaleng.2017.12.026>.
- [68] A. Gersborg-Hansen, M.P. Bendsoe, O. Sigmund, Topology optimization of heat conduction problems using the finite volume method, *Struct. Multidiscip. Optim.* 31 (2006) 251–259. <https://doi.org/10.1007/s00158-005-0584-3>.
- [69] T. Gao, W.H. Zhang, J.H. Zhu, Y.J. Xu, D.H. Bassir, Topology optimization of heat conduction problem involving design-dependent heat load effect, *Finite Elem. Anal. Des.* 44 (2008) 805–813. <https://doi.org/10.1016/j.finel.2008.06.001>.
- [70] X. Zhu, C. Zhao, X. Wang, Y. Zhou, P. Hu, Z.D. Ma, Temperature-constrained

- topology optimization of thermo-mechanical coupled problems, *Eng. Optim.* 51 (2019) 1687–1709. <https://doi.org/10.1080/0305215X.2018.1554065>.
- [71] T. Gao, P. Xu, W. Zhang, Topology optimization of thermo-elastic structures with multiple materials under mass constraint, *Comput. Struct.* 173 (2016) 150–160. <https://doi.org/10.1016/j.compstruc.2016.06.002>.
- [72] J.D. Deaton, R. V. Grandhi, Stress-based design of thermal structures via topology optimization, *Struct. Multidiscip. Optim.* 53 (2016) 253–270. <https://doi.org/10.1007/s00158-015-1331-z>.
- [73] W. Zhang, J. Yang, Y. Xu, T. Gao, Topology optimization of thermoelastic structures: Mean compliance minimization or elastic strain energy minimization, *Struct. Multidiscip. Optim.* 49 (2014) 417–429. <https://doi.org/10.1007/s00158-013-0991-9>.
- [74] X. Liu, C. Wang, Y. Zhou, Topology optimization of thermoelastic structures using the guide-weight method, *Sci. China Technol. Sci.* 57 (2014) 968–979. <https://doi.org/10.1007/s11431-014-5521-5>.
- [75] Q. Yang, B. Gao, Z. Xu, W. Xie, S. Meng, Topology optimisations for integrated thermal protection systems considering thermo-mechanical constraints, *Appl. Therm. Eng.* 150 (2019) 995–1001. <https://doi.org/10.1016/j.applthermaleng.2019.01.067>.
- [76] A. Takezawa, G.H. Yoon, S.H. Jeong, M. Kobashi, M. Kitamura, Structural topology optimization with strength and heat conduction constraints, *Comput. Methods Appl. Mech. Eng.* 276 (2014) 341–361. <https://doi.org/10.1016/j.cma.2014.04.003>.
- [77] X. Deng, J. Wang, J. Zhou, H. Shen, Z. Sheng, J. Zhang, X. Lv, C. Xie, A hybrid cellular automaton method for structural topology optimization with mechanical and heat constraints, *Front. Heat Mass Transf.* 12 (2019). <https://doi.org/10.5098/hmt.12.13>.
- [78] J.E. Marsden, T.J. Hughes, *Mathematical Foundations of Elasticity*, 1994.
- [79] M. Codegone, E. Sanchez-Palencia, Asymptotics of the scattering frequencies for a thermoelasticity problem with small thermal conductivity, *Modélisation Mathématique Anal. Numérique*. 23 (1989) 87–101.
- [80] R. Caivano, A. Tridello, D. Paolino, G. Chiandussi, Topology and fibre orientation simultaneous optimisation: A design methodology for fibre-reinforced composite components, *Proc. Inst. Mech. Eng. Part L J. Mater. Des. Appl.* 234 (2020) 1267–1279. <https://doi.org/10.1177/1464420720934142>.
- [81] J.R. Hartenstine, W.G. Anderson, R. Bonner, Titanium loop heat pipes for space nuclear power systems, *AIP Conf. Proc.* 969 (2008) 44–52. <https://doi.org/10.1063/1.2845001>.
- [82] B. Dutta, F.H. (Sam. Froes, *The Additive Manufacturing (AM) of titanium alloys*, Elsevier Inc., 2017. <https://doi.org/10.1016/j.mprp.2016.12.062>.
- [83] A. Boudjemai, M.H. Bouanane, A. Mankour, H. Salem, R. Hocine, R. Amri, Thermo-mechanical design of honeycomb panel with fully-potted inserts used for spacecraft design, *RAST 2013 - Proc. 6th Int. Conf. Recent Adv. Sp. Technol.* (2013) 39–46. <https://doi.org/10.1109/RAST.2013.6581238>.
- [84] A. Sanchez-Torres, *Radioisotope Power Systems for Space Applications*, *Radioisot. - Appl. Phys. Sci.* (2011). <https://doi.org/10.5772/20928>.
- [85] W.G. Anderson, R. Bonner, J. Hartenstine, J. Barth, High temperature titanium-water heat pipe radiator, *AIP Conf. Proc.* 813 (2006) 91–99. <https://doi.org/10.1063/1.2169184>.
- [86] L. Aydin, O. Aydin, H.S. Artem, A. Mert, Design of dimensionally stable composites using efficient global optimization method, *Proc. Inst. Mech. Eng. Part L J. Mater. Des. Appl.* 233 (2019) 156–168. <https://doi.org/10.1177/1464420716664921>.
- [87] A.M. Rao, C. Ratnam, J. Srinivas, A. Premkumar, Optimum design of multilayer composite plates using simulated annealing, *Proc. Inst. Mech. Eng. Part L J. Mater. Des. Appl.* 216 (2002) 193–197.

- <https://doi.org/10.1177/146442070221600304>.
- [88] Y.S. Liao, C.Y. Chiou, Robust optimum designs of fibre-reinforced composites with design-variable and non-design-variable uncertainties, *Proc. Inst. Mech. Eng. Part L J. Mater. Des. Appl.* 222 (2008) 111–121. <https://doi.org/10.1243/14644207JMDA139>.
- [89] P. Pedersen, Examples of density, orientation, and shape-optimal 2D-design for stiffness and/or strength with orthotropic materials, *Struct. Multidiscip. Optim.* 26 (2004) 37–49. <https://doi.org/10.1007/s00158-003-0295-6>.
- [90] S. Setoodeh, M.M. Abdalla, Z. Gürdal, Combined topology and fiber path design of composite layers using cellular automata, *Struct. Multidiscip. Optim.* 30 (2005) 413–421. <https://doi.org/10.1007/s00158-005-0528-y>.
- [91] X. Tong, W. Ge, X. Gao, Y. Li, Simultaneous optimization of fiber orientations and topology shape for composites compliant leading edge, *J. Reinf. Plast. Compos.* 38 (2019) 706–716. <https://doi.org/10.1177/0731684419842292>.
- [92] X. Tong, W. Ge, X. Gao, Y. Li, Optimization of Combining Fiber Orientation and Topology for Constant-Stiffness Composite Laminated Plates, *J. Optim. Theory Appl.* 181 (2019) 653–670. <https://doi.org/10.1007/s10957-018-1433-z>.
- [93] W. Hansel, W. Becker, Layerwise adaptive topology optimization of laminate structures, *Eng. Comput. (Swansea, Wales)*. 16 (1999) 841–851. <https://doi.org/10.1108/02644409910298156>.
- [94] A.A. Safonov, 3D topology optimization of continuous fiber-reinforced structures via natural evolution method, *Compos. Struct.* 215 (2019) 289–297. <https://doi.org/10.1016/j.compstruct.2019.02.063>.
- [95] T. Nomura, E.M. Dede, J. Lee, S. Yamasaki, T. Matsumori, A. Kawamoto, N. Kikuchi, General topology optimization method with continuous and discrete orientation design using isoparametric projection, *Int. J. Numer. Methods Eng.* (2014). <https://doi.org/https://doi.org/10.1002/nme.4799>.
- [96] J. Lee, D. Kim, T. Nomura, E.M. Dede, J. Yoo, Topology optimization for continuous and discrete orientation design of functionally graded fiber-reinforced composite structures, *Compos. Struct.* 201 (2018) 217–233. <https://doi.org/10.1016/j.compstruct.2018.06.020>.
- [97] H. Völkl, D. Klein, M. Franz, S. Wartzack, An efficient bionic topology optimization method for transversely isotropic materials, *Compos. Struct.* 204 (2018) 359–367. <https://doi.org/10.1016/j.compstruct.2018.07.079>.
- [98] L. Esposito, A. Cutolo, M. Barile, L. Lecce, G. Mensitieri, E. Sacco, M. Fraldi, Topology optimization-guided stiffening of composites realized through Automated Fiber Placement, *Compos. Part B Eng.* 164 (2019) 309–323. <https://doi.org/10.1016/j.compositesb.2018.11.032>.
- [99] J.H. Luo, H.C. Gea, Optimal orientation of orthotropic materials using an energy based method, *Struct. Optim.* 15 (1998) 230–236. <https://doi.org/10.1007/BF01203536>.
- [100] E. Brusa, R. Sesana, E. Ossola, Numerical modeling and testing of mechanical behavior of AM Titanium alloy bracket for aerospace applications, *Procedia Struct. Integr.* 5 (2017) 753–760. <https://doi.org/10.1016/j.prostr.2017.07.166>.
- [101] Y. Saadlaoui, J.L. Milan, J.M. Rossi, P. Chabrand, Topology optimization and additive manufacturing: Comparison of conception methods using industrial codes, *J. Manuf. Syst.* 43 (2017) 178–186. <https://doi.org/10.1016/j.jmsy.2017.03.006>.
- [102] E. Holmberg, B. Torstenfelt, A. Klarbring, Stress constrained topology optimization, *Struct. Multidiscip. Optim.* 48 (2013) 33–47. <https://doi.org/10.1007/s00158-012-0880-7>.
- [103] X. Gao, L. Li, H. Ma, An Adaptive Continuation Method for Topology Optimization of Continuum Structures Considering Buckling Constraints, *Int. J. Appl. Mech.* 9 (2017). <https://doi.org/10.1142/S1758825117500922>.
- [104] E. Holmberg, B. Torstenfelt, A. Klarbring, Fatigue constrained topology optimization, *Struct. Multidiscip. Optim.* 50 (2014) 207–219.

- <https://doi.org/10.1007/s00158-014-1054-6>.
- [105] J.W. Lee, G.H. Yoon, S.H. Jeong, Topology optimization considering fatigue life in the frequency domain, *Comput. Math. with Appl.* 70 (2015) 1852–1877. <https://doi.org/10.1016/j.camwa.2015.08.006>.
  - [106] Z. Chen, K. Long, P. Wen, S. Nouman, Fatigue-resistance topology optimization of continuum structure by penalizing the cumulative fatigue damage, *Adv. Eng. Softw.* 150 (2020) 102924. <https://doi.org/10.1016/j.advengsoft.2020.102924>.
  - [107] M. Collet, M. Bruggi, P. Duysinx, Topology optimization for minimum weight with compliance and simplified nominal stress constraints for fatigue resistance, *Struct. Multidiscip. Optim.* 55 (2017) 839–855. <https://doi.org/10.1007/s00158-016-1510-6>.
  - [108] J. Oest, E. Lund, Topology optimization with finite-life fatigue constraints, *Struct. Multidiscip. Optim.* 56 (2017) 1045–1059. <https://doi.org/10.1007/s00158-017-1701-9>.
  - [109] S.H. Jeong, J.W. Lee, G.H. Yoon, D.H. Choi, Topology optimization considering the fatigue constraint of variable amplitude load based on the equivalent static load approach, *Appl. Math. Model.* 56 (2018) 626–647. <https://doi.org/10.1016/j.apm.2017.12.017>.
  - [110] K. Nabaki, J. Shen, X. Huang, Evolutionary topology optimization of continuum structures considering fatigue failure, *Mater. Des.* 166 (2019) 107586. <https://doi.org/10.1016/j.matdes.2019.107586>.
  - [111] S. Zhang, C. Le, A.L. Gain, J.A. Norato, Fatigue-based topology optimization with non-proportional loads, *Comput. Methods Appl. Mech. Eng.* 345 (2019) 805–825. <https://doi.org/10.1016/j.cma.2018.11.015>.
  - [112] S. Suresh, S.B. Lindström, C.J. Thore, B. Torstenfelt, A. Klarbring, Topology optimization using a continuous-time high-cycle fatigue model, *Struct. Multidiscip. Optim.* 61 (2020) 1011–1025. <https://doi.org/10.1007/s00158-019-02400-w>.
  - [113] K. Sherif, W. Witteveen, K. Puchner, H. Irschik, Efficient topology optimization of large dynamic finite element systems using fatigue, *AIAA J.* 48 (2010) 1339–1347. <https://doi.org/10.2514/1.45196>.
  - [114] S.H. Jeong, D.H. Choi, G.H. Yoon, Fatigue and static failure considerations using a topology optimization method, *Appl. Math. Model.* 39 (2015) 1137–1162. <https://doi.org/10.1016/j.apm.2014.07.020>.
  - [115] S. Suresh, *Fatigue of Materials*, Cambridge University Press, 1998. <https://doi.org/10.1017/CBO9780511806575>.
  - [116] Yukitaka Murakami, *Metal Fatigue: Effects of Small Defects and Nonmetallic Inclusions*, Elsevier, 2002. <https://doi.org/10.1016/B978-0-08-044064-4.X5000-2>.
  - [117] M. Tang, P.C. Pistorius, Oxides, porosity and fatigue performance of AlSi10Mg parts produced by selective laser melting, *Int. J. Fatigue.* 94 (2017) 192–201. <https://doi.org/10.1016/j.ijfatigue.2016.06.002>.
  - [118] A. Yadollahi, N. Shamsaei, Additive manufacturing of fatigue resistant materials: Challenges and opportunities, *Int. J. Fatigue.* 98 (2017) 14–31. <https://doi.org/10.1016/j.ijfatigue.2017.01.001>.
  - [119] S. Beretta, S. Romano, A comparison of fatigue strength sensitivity to defects for materials manufactured by AM or traditional processes, *Int. J. Fatigue.* 94 (2017) 178–191. <https://doi.org/10.1016/j.ijfatigue.2016.06.020>.
  - [120] A. Tridello, J. Fiocchi, C.A. Biffi, G. Chiandussi, M. Rossetto, A. Tuissi, D.S. Paolino, Effect of microstructure, residual stresses and building orientation on the fatigue response up to 109 cycles of an SLM AlSi10Mg alloy, *Int. J. Fatigue.* 137 (2020) 105659. <https://doi.org/10.1016/j.ijfatigue.2020.105659>.
  - [121] G. Qian, Y. Li, D.S. Paolino, A. Tridello, F. Berto, Y. Hong, Very-high-cycle fatigue behavior of Ti-6Al-4V manufactured by selective laser melting: Effect of build orientation, *Int. J. Fatigue.* 136 (2020) 105628. <https://doi.org/10.1016/j.ijfatigue.2020.105628>.
  - [122] J. Martínez-Frutos, G. Allaire, C. Dapogny, F. Periago, Structural optimization

- under internal porosity constraints using topological derivatives, *Comput. Methods Appl. Mech. Eng.* 345 (2019) 1–25. <https://doi.org/10.1016/j.cma.2018.10.036>.
- [123] A. Tridello, J. Fiocchi, C.A. Biffi, G. Chiandussi, M. Rossetto, A. Tuissi, D.S. Paolino, Influence of the annealing and defects on the VHCF behavior of an SLM AlSi10Mg alloy, *Fatigue Fract. Eng. Mater. Struct.* 42 (2019) 2794–2807. <https://doi.org/10.1111/ffe.13123>.
- [124] T.H.H. Pian, K. Sumihara, Rational approach for assumed stress finite elements, *Int. J. Numer. Methods Eng.* 20 (1984) 1685–1695. <https://doi.org/10.1002/nme.1620200911>.
- [125] S.N. Patnaik, J.D. Guptill, L. Berke, Singularity in structural optimization, *Int. J. Numer. Methods Eng.* 36 (1993) 931–944.
- [126] M. Bruggi, On an alternative approach to stress constraints relaxation in topology optimization, *Struct. Multidiscip. Optim.* 36 (2008) 125–141. <https://doi.org/10.1007/s00158-007-0203-6>.
- [127] X. Guo, G.D. Cheng, S-relaxed approach in structural topology optimization, *Struct. Optim.* (1997) 258–266.
- [128] C. Le, J. Norato, T. Bruns, C. Ha, D. Tortorelli, Stress-based topology optimization for continua, *Struct. Multidiscip. Optim.* 41 (2010) 605–620. <https://doi.org/10.1007/s00158-009-0440-y>.
- [129] A. Chen, K. Cai, Z.L. Zhao, Y. Zhou, L. Xia, Y.M. Xie, Controlling the maximum first principal stress in topology optimization, *Struct. Multidiscip. Optim.* (2020). <https://doi.org/10.1007/s00158-020-02701-5>.
- [130] J. París, F. Navarrina, I. Colominas, M. Casteleiro, Topology optimization of continuum structures with local and global stress constraints, *Struct. Multidiscip. Optim.* 39 (2009) 419–437. <https://doi.org/10.1007/s00158-008-0336-2>.
- [131] Y. Luo, M.Y. Wang, Z. Kang, An enhanced aggregation method for topology optimization with local stress constraints, *Comput. Methods Appl. Mech. Eng.* 254 (2013) 31–41. <https://doi.org/10.1016/j.cma.2012.10.019>.
- [132] J. París, F. Navarrina, I. Colominas, M. Casteleiro, Block aggregation of stress constraints in topology optimization of structures, *Adv. Eng. Softw.* 41 (2010) 433–441. <https://doi.org/10.1016/j.advengsoft.2009.03.006>.
- [133] G.J. Kennedy, J.E. Hicken, Improved constraint-aggregation methods, *Comput. Methods Appl. Mech. Eng.* 289 (2015) 332–354. <https://doi.org/10.1016/j.cma.2015.02.017>.
- [134] D. Yang, H. Liu, W. Zhang, S. Li, Stress-constrained topology optimization based on maximum stress measures, *Comput. Struct.* 198 (2018) 23–39. <https://doi.org/10.1016/j.compstruc.2018.01.008>.
- [135] K. Kempen, L. Thijs, J. Van Humbeeck, J.P. Kruth, Mechanical Properties of AlSi10Mg Produced by Selective Laser Melting, *Phys. Procedia.* 39 (2012) 439–446. <https://doi.org/10.1016/j.phpro.2012.10.059>.
- [136] A. Tridello, J. Fiocchi, C.A. Biffi, M. Rossetto, A. Tuissi, D.S. Paolino, A. Tridello, Size-effects affecting the fatigue response up to 10<sup>9</sup> cycles ( VHCF ) of SLM AlSi10Mg specimens produced in horizontal and vertical directions, (n.d.) 1–28.
- [137] M.C.-Y. Niu, AIRFRAME: Stress Analysis and Sizing, Hong Kong Conmilit Press ltd., 1997.
- [138] Arcam EBM system, Ti6AL4V ELI Titanium alloy, (n.d.). [www.arcam.com](http://www.arcam.com).
- [139] J. Günther, D. Krewerth, T. Lippmann, S. Leuders, T. Tröster, A. Weidner, H. Biermann, T. Niendorf, Fatigue life of additively manufactured Ti–6Al–4V in the very high cycle fatigue regime, *Int. J. Fatigue.* 94 (2017) 236–245. <https://doi.org/10.1016/j.ijfatigue.2016.05.018>.